LABELING THE HUMAN RESPIRATORY SYNCYTIAL VIRUS GENOMIC RNA WITH EXOGENOUS PROBES FOR FLUORESCENCE AND ELECTRON MICROSCOPY

A Dissertation
Presented to
The Academic Faculty

by

Eric J. Alonas

In Partial Fulfillment
of the Requirements for the Degree
Doctor of Philosophy in the
School of Biomedical Engineering

Georgia Institute of Technology
December 2015

LABELING THE HUMAN RESPIRATORY SYNCYTIAL VIRUS GENOMIC RNA WITH EXOGENOUS PROBES FOR FLUORESCENCE AND ELECTRON MICROSCOPY

Approved by:

Dr. Philip J. Santangelo, Advisor
Department of Biomedical Engineering
Georgia Institute of Technology

Dr. Elizabeth R. Wright
Department of Pediatrics
Emory University

Dr. Thomas H. Barker
Deparment of Biomedical Engineering
Georgia Institute of Technology

Dr. Peng Xi
Department of Biomedical Engineering
Peking University

Dr. M.G. Finn
School of Chemistry and Biochemistry
Georgia Institute of Technology

Date Approved: July 15, 2015

ACKNOWLEDGEMENTS

I would like to thank my advisor and my thesis committee for their time and guidance. I would like to thank Shannon Sullivan, Sally Gerrish, DeWayne Roberson, Steve Marzec, and all of the BME staff for answering my questions. I would like to thank Andrew Shaw and the IBB staff for training and resources. I would like to thank my parents and family for always supporting me. I would like to thank my friends for sharing their experiences with me. Finally, I would like to thank my significant other and my cats, who have tolerated me while writing this dissertation.

TABLE OF CONTENTS

LIST OF FIGURES

LIST OF TABLES

SUMMARY

A method for labeling the genomic RNA of the human respiratory syncytial virus, as well as for isolating and examining the labeled filamentous virions was achieved. This method utilized the multiply labeled tetravalent probe design, first described in Santangelo et al. 2009. It was shown that by introducing MTRIPs into RSV infected cells immediately before isolating virus, the genomic RNA within individual filamentous virions could be labeled and imaged. This process did not seem to decrease viral titer or affect viral morphology, and allowed for the imaging of the virus using fixed and live cell conventional fluorescence microscopy and super-resolution microscopic techniques such as dSTORM and STED. The imaging of other structural components of the virus, such as the M protein, and as was discovered, the M2-1 protein was also shown. Additionally, the virus was examined for host proteins of the RLR family, which are involved in the cellular innate immune response. It was found that the protein MDA5 was localized in the isolated filaments. Finally, gold nanoclusters were covalently bound to the RNA probe to create a probe that would generate contrast in cryo-TEM and cryo-ET. By hybridizing the probe to an mRNA encoding GFP, complexing it with a cationic lipid transfection agent, and delivering it to cells before plunge-freezing, it was demonstrated that the mRNA-lipoplex granules could be detected. In conclusion, the method allows for both dynamic and ultrastructural information about the viral genome to be gathered.

CHAPTER 1

INTRODUCTION

This introduction will broadly address the biology of respiratory syncytial virus and the motivation for imaging viruses. It will briefly address some of the techniques previously used by other groups to image RNA and viruses, as well as briefly review the imaging modalities used in this thesis.

Respiratory syncytial virus taxonomy, prevalence, pathology, treatment

Respiratory syncytial virus (RSV) is a non-segmented, negative-sense RNA virus that infects humans, cows, and sheep. It belongs to the order *Mononegavirales*, family *Paramyxoviridae*, subfamily *Pneumovirinae*, and genus *Pneumovirus*. It shares the *Pneumovirinae* subfamily with human and avian metapneumoviruses. The other subfamily within the family, *Paramyxovirinae*, contains measles, mumps, Nipah, Hendra, human and animal parainfluenza, etc. Human RSV is further divided into two antigenic subgroups, A and B. It causes upper respiratory tract infections in infants, immunocompromised individuals, and the elderly. The global disease burden in children under 5 years of age was 33.8 million cases, with at least 3.4 million cases requiring hospitalization. The virus causes acute lower respiratory infections (coughing, wheezing, etc.), bronchiolitis (infection and inflammation of distal bronchiolar airways), and pneumonia.[1-4]

Current treatment is limited to the prophylactic administration of a monoclonal antibody against the RSV fusion protein (palivizumab) in high risk individuals and the antiviral ribavirin, which has been hampered by safety, efficacy, and cost concerns.[3] Vaccine attempts have been unsuccessful, possibly due to poor maturation of high affinity antibodies.[5] The failure of a formalin inactivated vaccine in the 1960s was

extremely problematic, as it actually led to enhanced disease in children when challenged.[3] Looking towards the future, a live attenuated vaccine has shown some promise in infants, but as of yet has not shown sufficient efficacy.[6] As for new treatments, a new monoclonal antibody against the glycoprotein (G) is being studied[7]. Also, new nucleoside analogs that are specific for the viral polymerase are being pursued[8,9], however, none of these experimental candidates have been approved by FDA for clinical use to date.

RSV virion

The respiratory syncytial virus virion is an enveloped, pleomorphic structure on the order of 100 nm in diameter, with filamentous virions ranging from 2 μm-8 μm in length.[2] The genome is ~15.2 kb long, encoding 11 proteins: the fusion protein (F), the major/attachment glycoprotein (G), the viroporin (SH), the nucleoprotein (N), the phosphoprotein (P), the polymerase (L), two nonstructural proteins (NS1 and NS2), the matrix protein (M), and two M variants that are alternate reading frames of the M gene (M2-1 and M2-2).[2] The F, G, and SH are all embedded in the viral envelope, and F and G typically appear as "spikes" in TEM images.[10,11] Underneath the membrane, the M protein is thought be the driver filament formation.[12] The N and P proteins are associated with the ribonucleoprotein (RNP), and N in particular is thought to comprise a helical nucleocapsid that protects the genome from degradation by nucleases.[13,14] The NS1 and NS2 proteins have been shown to regulate the host cell's innate immune response.[15-17] The M2-1 and M2-2 have been shown to be transcription processivity[18] and transcription and replication regulatory[19] factors, respectively.

The infection cycle begins when an RSV virion fuses with the host cell membrane. The F protein and its antigenic sites have been reasonably well

characterized[5,20,21], but the fusion receptor's identity has been debated, with some evidence for nucleolin[22]. Once the genome is inside the cytoplasm, the L polymerase begins transcribing mRNAs for each viral protein, which are capped and polyadenylated.[23] Gene start and end sequences surround each gene and are not transcribed, but provide instruction to the polymerase[23]. The L polymerase is also responsible for replicating the entire genome into positive sense, antigenome, from which it can then make more copies of the negative sense genome. Leader (3' end) and trailer (5' end) regions on the genome serve as promoters to recruit the L polymerase.[23] Later in the infection (24 hr post infection), infected cells can be observed by microscopy to contain large granules of N and P, which are termed inclusion bodies[10,24]. Filamentous virions protruding from the cell membrane are also observable[10,11,25]. Infected cells can form multinucleated syncytia, due to the envelope proteins on the cell surface.[26] Finally, it should be noted that in cell culture, most of the virus remains cell-associated without further steps to release the virus.[27]

Rationale and key questions

Imaging viruses can provide key insights into their structure, and by extension function, as well as the dynamics of the viral infection cycle. Some viruses, including RSV, form macromolecular assemblies from their own proteins and cellular proteins whose structure can be inferred by other analyses, but conclusively demonstrated by imaging.[28,29] A virus infection is a highly dynamic process that involves attachment and entry of the infectious particle, trafficking to the appropriate site of replication, translation of viral proteins, reorganization of the host cell, and finally release of the progeny virions.[30] All of these events take place over different timescales (entry takes

place in minutes to hours whereas replication can take hours or days) and different conditions (cell-to-cell heterogeneity in the innate immune response), which can only be fully captured by imaging then over time.

With regard to RSV, this thesis is focused on a few key areas. These areas are:

1. The structure of the RSV RNP within the virion. The RNP of RSV has been previously shown as somewhat concentric electron dense puncta in thin section TEM[31], described as a helix in crystallography[14] and cryo-EM[13]. The number of complete vs. truncated genomes per virion and their orientation would help define the features of a D.I. particle. Imaging how the genome might be attached to M would provide insight into virion assembly.
2. The role of M2-1. This 21 kDa protein has been shown to be a transcription processivity factor[18], interact with M[32], P, and RNA[33,34], and possibly form a tetramer[33]. But its role in virion structure is somewhat unclear.
3. Replication sites and interactions with host cell proteins. The role of inclusion bodies has been subject to long debate; they are suspected of being sites of replication[10]. Understanding more about their constituent proteins, including N, and its possible interactions with other host cell proteins might lead structural and functional insights.

Originally, we proposed two aims to investigate the key areas:

1. Develop probe-labeled RSV viral particles
2. Develop cryo-electron tomography compatible MTRIP-labeled RSV

While this thesis completed the first aim, the second aim will be finished by another student. Two steps though are being taken towards this second aim, 1) we are making

PNA probes to ensure high affinity binding to the RNA, and 2) optimizing Nanogold conjugates in order to maximize contrast of the RNA in cryo-EM. In order to optimize the Nanogold conjugates, we pursued a simpler model system that guaranteed large number of RNA molecules in specific locations within the cell, facilitating probe development. Using a RNA-lipoplex model, we were able to develop an electron dense RNA probe and detect RNA in cells. In future work, this probe, plus our PNA ligands, should facilitate RSV imaging via cryo-EM.

Previous virus imaging

Other groups have attempted imaging viruses in the past using a variety of approaches. The first approach was to nonspecifically label one of the exterior proteins with a covalent organic dye. This has been done for nonenveloped viruses, such as adeno-associated virus (AAV)[35], polio[36,37], and human papilloma virus (HPV)[38], as well as enveloped viruses, such as influenza[39,40]. The labeling of AAV by Seisenberger *et al.* was one of the first attempts; they used Cy5 labeled viruses to track AAV entering HeLa cells and based on the trajectories were able to subdivide AAV entry into three steps.[35] These steps were: diffusion in solution and repeated cell touching by observing the virus in fluorescence and the cell membrane in phase contrast microscopy (with an apparent D = 7.5 $\mu m^2/s$ outside the cell); endocytosis and diffusion based on fitting the mean square displacement over time (with apparent D=1.3 $\mu m^2/s$ and D = 0.57 $\mu m^2/s$, which they attribute to being outside or inside an endosome); and nuclear diffusion with drift by fitting (D = 0.25-0.35 $\mu m^2/s$, with and without drift. However, this approach does not reveal whether or not the virus is actually in a compartment. Additionally, they were only able to acquire trajectories on the order of 1-10 s due to photobleaching of the dye.

Watching such a short trajectory and fitting the entire trajectory might lead one to miss any intermediate, motor driven transportation.[41]

The imaging of poliovirus by Vaughan *et al.* and Brandenburg *et al.* took the virus tracking a step further. In Vaughan *et al.*, the authors used depolymerizing agents such as nocodazole (microtubules) and cytochalasin D (F-actin), metabolic toxins such as sodium azide, and motor inhibitors such as blebbistatin (myosin II) in conjunction with a Cy5 labeled polio to record trajectories around 2 minutes in length.[37] However, the exact mechanism of transport, the destination of the poliovirus within the cells (the site of replication), and the separation of the positive sense genomic RNA from the viral coat proteins that were labeled with Cy5 were not addressed. Brandenburg *et al.* increased the sophistication of the technique by dual labeling with a nucleic acid binding Syto dye.[36] This dual color approach allowed them visualize genome release from the viral coat proteins as a decrease in signal from the Syto dye. Beyond that point (measured to be approximately 20 min into the imaging), they are unable to further track the virus. The authors show using buffer pH changes that the virus is internalized before release of the RNA, and by using siRNA and small molecule inhibitors show that virus entry is independent of clathrin, caveolin, flotillin, and macropinocytosis, with the only vulnerability being cholesterol extraction from the cell membrane by methyl-β-cyclodextrin.

The HPV study by Schelhaas *et al.* represents a cross between the covalent conjugation and GFP fusion expressed protein strategies, as they used HPV pseudoviruses labeled with AlexaFluor 488 on the outside and carried a plasmid encoding GFP on the inside.[38] They use this technique in a fusion assay type experiment, where

virus is pre-absorbed to cells at a cold temperature (typically 4 °C) to synchronize viral attachment, excess virus removed, then cells are brought back to 37 °C, allowed to incubate for a designated period of time to allow the virus to enter, and then excess virus is removed (in this case by briefly washing with a pH 10.5 buffer). The number of cells expressing GFP is observed at later timepoint, in this case 48 hours post infection. The authors tested many different inhibitors to show that HPV entry was independent of clathrin, caveolin, cholesterol, and flotillin, and they go on to suggest that the virus might enter the cells through a pathway that is unique from macropinocytosis, but shares many of the same components and ends up in late endosomes/lysosomes. Once again, the exact sequence of events of the release of the genome are unaddressed by this particular study.

The second approach was to label the viral envelopes with a lipophilic dye, like DiO or DiD; this has been done for dengue[42], hepatitis C[43], Ebola[44], and influenza[39,40,45,46]. This approach is arguably a less invasive approach to the labeling of enveloped viruses, as it does not covalently modify the surface proteins. In van der Schaar *et al*. the authors used DiD labeled virus along with cells transfected with YFP-fused clathrin light chain plasmid to examine entry. By fitting plots of mean square displacements, they show that dengue diffuses to pre-existing clathrin coated pits with an apparent diffusion coefficient of 0.009 $\mu m^2/s$ before capture by a coated pit; this is an order of magnitude lower than the diffusion coefficients reported for the non-enveloped viruses mentioned previously. The authors also used Rab5-CFP and Rab7-YFP transfected cells to show colocalization between the labeled virus, demonstrating that the virus is internalized at around 3.5 min and fuses in the late endosome at around 12.5 min. Post fusion there is no further information that can be gained from the technique.

Hepatitis C was studied using a combination of siRNA silencing of component of the endocytosis pathway and labeled virus tracking.[43] In Coller *et al.*, the authors DiD and DiI to label HCV virions, which notably they then immobilized on glass and stained for viral proteins. They used the labeled virus to examine the relationship between the virus and either the actin filopodia or the endocytosis components. They show the when virions landed on an actin filopodia, they moved with increasing means squared displacement in single direction (for 7s tracks), suggesting active transport which was sensitive to actin depolymerization with cytochalasin D. They also show colocalization with clathrin light chain and c-Cbl (E3 ubiquitin ligase. However, they do not show convincing actin depolymerization in their GFP-actin transfected cells and label only a short window of the trajectory as active transport.

Influenza has been a popular target for labeling on the basis of its global disease burden. One of the first attempts, Lakadamyali *et al.* used only DiO alone (or in conjugation with the pH sensitive dye Cypher 5 to show that influenza infections in CHO cells could be divided up into four phases of motion: passive transport, active transport, passive transport, and active transport on the basis of mean square displacement regressions.[39] Note that this is the work of the same corresponding author as the poliovirus labeling. They used the fluorescence intensity of the DiO, which is initially partially quenched in the virion, but increases in intensity upon release, as a metric of fusion. Their tracks are approximately 8 min in length, showing an improvement in the duration of the live cell imaging. They suggest that noise in their measurements in mean square displacement are due to noise, but it is hard to be sure with no cellular markers labeled.

The same group continued to examine singly-labeled influenza virions and their associations with FP-fused host cell factors in subsequent publications.[40,45,47] In Rust *et al.*, the authors examined the entry of labeled influenza virions and their relationship with EYFP-fused clathrin, showing colocalization between the virion and virus-induced clathrin assembly "events" on the other of 1 min out of a 7 min trajectory.[47] The work of Chen *et al.* showed that epsin 1 might be an adaptor that is specific to certain cargoes that are internalized by clathrin mediated endocytosis, such as the influenza virus.[45] Finally, the work of Sun *et al.* demonstrated the association between labeled influenza virus and the coat protein I (COPI) complex, which coats vesicles trafficking between the Golgi apparatus and the endoplasmic reticulum (ER) as well as regulates endocytosis.[40] However, their conclusions make it seem like COPI subunits do not interact directly with the virus so much as disrupt global endosomal trafficking.

A slightly more complex attempt at using the quenching of lipophilic dyes was made three years later by Sakai *et al*. (whose labeling technique was adapted to RSV recently by Krzyzaniak *et al.*[48] which will be discussed later) in which two lipophilic dyes are used, DiO and R18. Initially the DiO fluorescence is quenched by R18, but upon fusion the DiO and R18 are no longer in close proximity and both begin to fluoresce. They use their labeled virus to show colocalization between influenza virus and fluorescently labeled EGF, which when combined with TEM suggested that influenza virus is capable of entering the cell in relatively small endosomes.

Some viruses will allow fluorescent protein fusions to be incorporated into their genomes, as has been done with HIV[49,50]. In Jouvenet *et al.* 2008, the authors incorporated Gag-mCherry and Gag-GFP fusions in HIV-1 virus like particles (VLPs).[49]

They used expressed FP-fusions, along with untagged Gag, to monitor VLP assembly, suggesting that slowly moving Gag puncta were actual VLPs. The puncta assembled over 5-6 min, but did not move away from the surface which is likely due to the limits of the experimental setup (the cells were flipped over to allow for TIRF imaging). In an extension of this work in Jouvenet *et al.* 2009, the authors labeled the RNA using the MS2-GFP system to be discussed later and Gag with an FP-fusion in order to gain a more detailed picture of VLP assembly.[50] They demonstrated that a small number of Gag molecules is capable of "anchoring" the RNA to the membrane, onto which more Gag molecules can then assemble to make a complete VLP. However, how the RNA is transported to the particular site of assembly was not addressed.

There are a few points from the previous virus labeling attempts that deserve emphasis. First, it is clear that covalent conjugation of organic fluorophores is typically tolerated and can be applied to non-enveloped viruses. For enveloped viruses, the method of choice is a lipophilic dye. Second, lipophilic dyes are limited by their ability to observe the virus only up until the moment of fusion, as they are not associated with the viral nucleocapsid. They might provide evidence of acidification of the endosome if that is the mechanism of entry of the virus and that the loading of the lipophilic dye within the virion is significantly high enough to achieve initial quenching. Third, most of the viruses previously studied have not been as pleomorphic as RSV. This presents a challenge, as most of the virus is cell associated, implying that the filaments extending from the cell surface are important in transmission of the infection, so it is necessary to monitor both spherical virions as well as filamentous ones. This thesis attempts to emphasize the filamentous virions, as long filaments are not present in previous attempts by other

groups to label RSV. Fourth, in order to observed viral entry, the observation period must be several minutes long. This requires that the sample must fluoresce with high intensity and succumb to as little photobleaching as possible, which is challenging enough for certain organic fluorophores, let alone for fluorescent proteins. It is also necessary to observe for long periods of time in order to gather long enough trajectories for tracking purposes. Fifth, it is necessary to observe virions at appreciably high frame-rates, so as to avoid undersampling the motion. Indeed, the particle tracks observed for influenza especially contain high frequency information that might indicate modes of transport other than simple passive diffusion. Given the fact that the goal of this thesis was to study a cell-associated, pleomorphic RNA virus, which will require observation of events leading up to and post fusion, and given that RSV is relatively intolerant to FP-structural protein fusions[51], it is the belief of this author that the best target for labeling RSV in a specific fashion is to label the genomic RNA itself.

Motivation for imaging RNA

There are several reasons for imaging RNA at high resolution. For cellular mRNAs, the expression level of a particular mRNA is not the sole regulator of translation into proteins.[52] Indeed, the translation and stability of an mRNA are controlled through a variety of mechanisms. The spatial localization of a particular RNA within a cell helps to control its translation and can reflect the developmental fate of a particular cell or organism, as has been observed in yeast, *Drosophila melanogaster, Xenopus oocytes*, and fibroblasts.[53]. In addition, an RNA can be regulated by the type and number of RNA binding proteins (RBPs) or miRNAs with which it interacts. For example, ribosomal assembly and translation initiation is highly dependent on the recognition of an mRNA 5’

cap by the appropriate eukaryotic initiation factors (eIFs). These eIFs also interact with polyA binding protein to change the structure of the mRNA to facilitate translation.[54]. Another example is the RNA binding protein HuR, which binds to one or more AU rich sequences in the 3' untranslated regions (UTRs) of mRNAs in order to stabilize them.[55] To give a final example with a virus, the proteins within the influenza RNP help regulate the trafficking, transcription, replication, and packaging of its segmented genome, ensuring that a virion contains each and every segment with high fidelity.[56] Clearly, imaging can help preserve spatial information for a given RNA and given a high enough resolution, can help to elucidate the complicated structures that RNA and RBPs form.

Previous RNA imaging

Fixed and live cell RNA imaging has been pursued as a way to determine the spatial localization, associated proteins, and temporal changes of an RNA imaging. Fluorescent, fixed cell RNA imaging was popularized by fluorescence in situ hybridization (FISH)[57]. This technique involves fixing cells and introducing short, antisense oligonucleotides that are labeled with fluorophores or dioxigenin. It has been used by Sundell *et al.*to show that β-actin mRNAs localize to the periphery of chicken embryonic fibroblasts when the actin cytoskeleton is intact.[57] It has also been used by Long *et al*. to show the localization of *lacZ* induced transcripts in yeast cells, with and without deletions to introns that might inhibit nuclear export.[58] The related technique, RNA in situ hybridization, has been used to determine RNA localization on actin filaments at the ultrastructural level.[59] However, many of these early fluorescence studies lacked single molecule sensitivity, which is important considering that there are far fewer mRNAs than proteins in a cell. They also were limited to observing gross temporal

effects; more subtle effects like motor driven transport occur on timescales that are far too short to observe using fixed cell techniques.

Live cell techniques solve the temporal problem of fixed cell techniques. They include the aforementioned MS2-GFP along with λ_N-GFP, Pumilio homology domains (Pum-HD), and RNA aptamers such as Spinach. The most popular, MS2-GFP, involves transfecting cells with a GFP-fused a GFP fused RNA binding protein (specifically MS2, a bacteriophage coat protein) along with a target mRNA that contains multiple hairpin repeats.[60] MS2-GFP utilizing six stem-loop sequences was first used by Bertrand *et al.* to show the localization of *ASH1* mRNA to the budding tip of yeast cells.[60] However, in order to achieve single molecule sensitivity needed to observe both localized and non-localized mRNAs, more stem-loop repeats were needed. In the work by Fusco *et al.*, the authors introduced 24 stem-loop repeats into inducible mRNA reporters that contained the 3' UTR of β-actin, and imaged at a rate of 9 Hz to show that mRNAs can undergo directed motion at a velocity of up to 1 μm/s, contingent on an intact cytoskeletal network.[61] Similarly, the work of Shav-Tal *et al.* used a 24 stem-loop inducible reporter mRNA to examine nuclear transport, which while not purely directed motion was also found to be more complex than simple diffusion.[62] The work of Yamagishi *et al.* further extended the work of Fusco *et al.* by using the entire β-actin ORF and 3' UTR followed by four MS2 repeats to suggest that actin microfilaments might confine mRNAs at the cell periphery.[63] They suggest that single-molecule sensitivity can be achieved by intensity measurements and Gaussian fitting, thus fewer MS2 sites are needed. The MS2-GFP system was taken a step further by engineering a transgenic mouse to stably express the MS2-GFP and the target mRNA.[64]

However, all of the MS2-GFP work hinges on the assumption that cells can be transfected with reporter mRNAs. This assumption might not hold true for mRNAs (and viral RNAs for that matter), in which the addition of so many repeat sequences might interfere with RNA secondary structure and RBP sites necessary for proper post-transcriptional processing. Additionally, it might change RNA:RBP stoichiometry, leading to improper regulation. As for imaging the RNAs, given that the fluorescent protein fusion is constitutively expressed, high backgrounds from unbound proteins can reduce the signal to noise ratio and make it hard to distinguish single puncta (although MS2 is typically engineering with a nuclear localization sequence to diminish this problem). For cells, not all cell types are easily transfectable. For viruses, not all viral titers are able to be rescued after inserting so many nucleotides.

An alternative system to MS2-GFP is the λ_N-GFP system. This system utilizes a 22 amino acid peptide, λ_N, fused to 3 copies of a GFP and a nuclear localization sequence.[65] The peptide binds to a 15 nucleotide stem-loop called boxB that is expressed as part of a reporter mRNA, with only four repeats of boxB needed to label the mRNA. Originally described by Daigle *et al,* the system was used to examine the localization of reporters containing β-actin zip code protein binding sequences. It was also used to examine the localization of an mRFP fused reporter containing signal recognition particle receptor subunit B, thereby allowing the authors to observe the localization of the reporter in one wavelength and the translated protein in another wavelength simultaneously. The λ_N-GFP system was combined with MS2-GFP by Lange *et al.*, showing the colocalization of two different mRNA species into the budding tip of yeast.[66] However, the original work by Daigle does not demonstrate single molecule sensitivity.

Concerns about suitability of the MS2-GFP system to certain mRNAs/cell types also apply to the λ_N-GFP system.

RNA aptamers represent a different approach from the RBP-FP strategy. These RNA sequences that bind organic molecule mimicking the fluorophore in GFP and EGFP were found by systematic enrichment and directed evolution.[67] These aptamers, named Spinach,[68] Spinach2,[69] and Broccoli,[70] can be coded into a reporter RNA and when the appropriate organic mimic ligand is delivered to cells, will fluoresce. These aptamers have been used in mammalian cells to track the noncoding RNA 5S. However, there are several caveats to using this method as opposed to other RBP-FP methods. Most importantly, the folding of the aptamer might be perturbed by changes in temperature, cellular ion concentration, or adjacent sequences within the reporter RNA. The sensitivity to adjacent sequences might necessitate the insertion of further nucleotides or "spacer" sequences, increasing the length of the aptamer. Also, multiple Spinach repeats are needed to achieve multiple sequence specificity. Finally, depending on the particular reporter, post-transcriptional regulation and interactions with native RBPs might be perturbed by the presence of the aptamer, potentially changing localization.

Another alternative to MS2-GFP is the Pum-HD system, first described by Ozawa *et al.*[71] In this system, two different constructs of the Pumilio homology domain, a protein domain of the RBP human PUMILIO1, are each fused with half of EGFP. The Pum-HD retains its ability to bind to a specific 8 nucleotide sequence, and by mutating the translated protein sequence, different RNA target sequence specificity can be achieved. Ozawa *et al.* used the Pum-HD system to target mitochondrial RNA, observing its localization with and without the presence of reactive oxygen species.[71] Later on, the

same group demonstrated that the Pum-HD system could be engineered to localize β-actin mRNA.[72] One advantage of the Pum-HD system over the MS2-GFP system it abrogates the need to express a reporter mRNA. It also has lower background as the unbound Pum-HD molecules are not fluorescent. However, the affinity of Pum-HD for its target sequence must be carefully examined every time a mutation is introduced. Also, the dissociation constant of the two FP halves is relatively low, so a positive fluorescence signal might persist even in the event of dissociation or degradation of the target mRNA.

In order to increase the specificity of the probe to the RNA target over that achieved by engineered RBP methods, other groups have turned to using antisense oligonucleotides that bind using Watson-Crick pairing. One such method is the molecular beacon, which consists of an oligonucleotide with a fluorophore bound to one end and a quencher to the other. The 5' and 3' end sequences are complimentary to each other, so when there is no target present the molecular beacon exists as a stem-loop. The presence of a target RNA allows the stem to open and the beacon to bind to the target sequence, separating the fluorophore from the quencher spatially and allowing fluorescence. This system was first described by Tyagi *et al.* for an *in vidrio* system[73], but has since been used intracellularly.[74] In live cells, the beacons have been microinjected to track native mRNAs in *Drosophila* oocytes[74] and native β-actin mRNAs,[75] albeit using a ratio with control molecule beacons for the latter case. While the idea of an activatable mRNA probe is compelling, the switching of molecular beacons is problematic for a couple of reasons. Designing beacon sequences with the proper affinity for native RNAs can be somewhat challenging. Also, non-covalent interactions between the fluorophore and the

quencher, or the beacons for other cellular structures, can decrease the positive signal and increase the background, respectively.

A simpler approach might be to use a linear oligonucleotide, but to increase its affinity using modified bases. One example of this is the work of Molenaar *et al*, in which the authors used linear 2'-O-methyl RNA oligonucleotides with fluorophores to image U1, U2, U3 small nuclear RNAs, 28S rRNA, polyA mRNA, and human cytomegalovirus gene IE1 RNA within the nucleus of a live cell using microinjection.[76] It is likely that the authors picked the nucleus because microinjection is able to flood organelles such as the nucleus with high numbers of probes. A more delicate approach is the delivery of nucleic acids using the bacterial pore-forming toxin streptolysin-O (SLO), which was compared to traditional transfection methods using a modified oligonucleotide by Spiller *et al.*[77]

Our own group previously reported the multiply labeled tetravalent RNA imaging probe (MTRIP) for fixed and live cell imaging.[78,79] This method consists of four fluorescently labeled oligonucleotides, end-labeled with biotin, that are complexed together with streptavidin to achieve single molecule sensitivity. Combining the modified probes with the SLO delivery enables enough probes to enter the cell cytoplasm and bind to mRNAs, of which single molecules are bright enough to be detected. It is this probe that formed the starting point for the work in the next chapters.

Imaging modalities utilized

Finally, the imaging modalities used in this work will be briefly described. Conventional fluorescence microscopy is limited in resolution by the diffraction of visible light. Within the past decade, research has been focused on different methods of

circumventing this limit and achieving "sub-diffraction" or "super-resolution" beyond the classical optics limits. The two systems to which we had access were a stimulated emission depletion (STED) microscope and a direct stochastic optical reconstruction microscope (dSTORM). STED, first described by Hell and Wichmann,[80] uses two lasers, one to excite the fluorophores in the sample and one in the shape of a donut (STED beam) to induce stimulated emission for all but the most central fluorophores that had been excited. The result is that the point spread function is essentially decreased in size and the resolution increased. On the other hand, dSTORM uses a high intensity light source and chemically modified buffers to deactivate and reactivate individual fluorophores in a sample.[81] Only a few points of light are collected per image, they are then computationally fitted to find the centroid, and after thousands are images are processed, the structures in the image can be observed. Both of these techniques help bridge the resolution gap between light microscopy and electron microscopy.

Finally, we utilized cryo-electron microscopy (cryo-EM) and cryo-electron tomography (cryo-ET) to examine the ultrastructure our RNA probes bound to a target. These techniques involve flash freezing a biological sample to preserve its native, hydrated state. For cryo-ET, the sample is tilted through a range of angles and several low electron dose images are acquired. After reconstruction, a 3D volume of the specimen is generated.[82]

A summary of the achievable lateral an axial resolutions using STED, dSTORM, and cryo-electron tomography, in this case for the well described nuclear pore complex (NPC), can be found in Table 1.1.

	STED	dSTORM	cryo-ET
Lateral resolution	20-30 nm[83]	15 nm[84]	5-8 nm[85]

Table 1.1 Resolution of the nuclear pore complex by STED, dSTORM, and cryo-ET.

References

1.Pickles, R. J. & DeVincenzo, J. P. Respiratory syncytial virus (RSV) and its propensity for causing bronchiolitis. *The Journal of Pathology* **235,** 266-76 (2014).

2.Collins, P. L., Fearns, R. & Graham, B. S. Respiratory syncytial virus: virology, reverse genetics, and pathogenesis of disease. *Current Topics in Microbiology and Immunology* **372,** 3-38 (2013).

3.Meng, J., Stobart, C. C., Hotard, A. L. & Moore, M. L. An overview of respiratory syncytial virus. *PLoS Pathog.* **10,** e1004016 (2014).

4.Nair, H. *et al.* Global burden of acute lower respiratory infections due to respiratory syncytial virus in young children: a systematic review and meta-analysis. *The Lancet* **375,** 1545 (2010).

5.Arbiza, J. *et al.* Characterization of two antigenic sites recognized by neutralizing monoclonal antibodies directed against the fusion glycoprotein of human respiratory syncytial virus. *J. Gen. Virol.* **73 (Pt 9),** 2225-34 (1992).

6.Karron, R. A. *et al.* Identification of a recombinant live attenuated respiratory syncytial virus vaccine candidate that is highly attenuated in infants. *J. Infect. Dis.* **191,** 1093-104 (2005).

7.Boyoglu-Barnum, S. *et al.* An anti-G protein monoclonal antibody treats RSV disease more effectively than an anti-F monoclonal antibody in BALB/c mice. *Virology* **483,** 117-125 (2015).

8.Clarke, M. O. *et al.* Discovery of β-d-2′-deoxy-2′-α-fluoro-4′-α-cyano-5-aza-7,9-dideaza adenosine as a potent nucleoside inhibitor of respiratory syncytial virus with excellent selectivity over mitochondrial RNA and DNA polymerases. *Bioorganic & Medicinal Chemistry Letters* **25,** 2484 (2015).

9.Deval, J. *et al.* Molecular Basis for the Selective Inhibition of Respiratory Syncytial Virus RNA Polymerase by 2‘-Fluoro-4’-Chloromethyl-Cytidine Triphosphate. *PLoS Pathog.* **11,** e1004995 (2015).

10.Norrby, E., Marusyk, H. & Orvell, C. Morphogenesis of respiratory syncytial virus in a green monkey kidney cell line (Vero). *J. Virol.* **6,** 237-42 (1970).

11.Bächi, T. & Howe, C. Morphogenesis and ultrastructure of respiratory syncytial virus. *J. Virol.* **12,** 1173-80 (1973).

12.Mitra, R., Baviskar, P., Duncan-Decocq, R. R., Patel, D. & Oomens, A. G. P. The human respiratory syncytial virus matrix protein is required for maturation of viral filaments. *J. Virol.* **86,** 4432-43 (2012).

13.Bakker, S. E. *et al.* The respiratory syncytial virus nucleoprotein-RNA complex forms a left-handed helical nucleocapsid. *J. Gen. Virol.* **94,** 1734-8 (2013).

14.Tawar, R. G. *et al.* Crystal structure of a nucleocapsid-like nucleoprotein-RNA complex of respiratory syncytial virus. *Science* **326,** 1279-83 (2009).

15.Hastie, M. L. *et al.* The human respiratory syncytial virus nonstructural protein 1 regulates type I and type II interferon pathways. *Mol. Cell Proteomics* **11,** 108-27 (2012).

16.Kotelkin, A. *et al.* The NS2 protein of human respiratory syncytial virus suppresses the cytotoxic T-cell response as a consequence of suppressing the type I interferon response. *J. Virol.* **80,** 5958-67 (2006).

17.Boyapalle, S. *et al.* Respiratory syncytial virus NS1 protein colocalizes with mitochondrial antiviral signaling protein MAVS following infection. *PloS one* **7,** e29386 (2012).

18.Zhou, H., Cheng, X. & Jin, H. Identification of amino acids that are critical to the processivity function of respiratory syncytial virus M2-1 protein. *J. Virol.* **77,** 5046-53 (2003).

19.Bermingham, A. & Collins, P. L. The M2-2 protein of human respiratory syncytial virus is a regulatory factor involved in the balance between RNA replication and transcription. *Proc. Natl. Acad. Sci. U.S.A.* **96,** 11259-64 (1999).

20.Beeler, J. A. & van Wyke Coelingh, K. Neutralization epitopes of the F glycoprotein of respiratory syncytial virus: effect of mutation upon fusion function. *J. Virol.* (1989).

21.McLellan, J. S. *et al.* Structure of RSV Fusion Glycoprotein Trimer Bound to a Prefusion-Specific Neutralizing Antibody. *Science* **340,** 1113 (2013).

22.Mastrangelo, P. & Hegele, R. G. RSV fusion: time for a new model. *Viruses* **5,** 873-85 (2013).

23.Noton, S. L. & Fearns, R. Initiation and regulation of paramyxovirus transcription and replication. *Virology* **479-480,** 545 (2015).

24.García, J., García-Barreno, B., Vivo, A. & Melero, J. A. Cytoplasmic inclusions of respiratory syncytial virus-infected cells: formation of inclusion bodies in transfected cells that coexpress the nucleoprotein, the phosphoprotein, and the 22K protein. *Virology* **195,** 243-7 (1993).

25.Roberts, S. R., Compans, R. W. & Wertz, G. W. Respiratory syncytial virus matures at the apical surfaces of polarized epithelial cells. *J. Virol.* **69,** 2667-73 (1995).

26.Heminway, B. R. *et al.* Analysis of respiratory syncytial virus F, G, and SH proteins in cell fusion. *Virology* **200,** 801-5 (1994).

27.Ueba, O. Respiratory syncytial virus. I. Concentration and purification of the infectious virus. *Acta Med. Okayama* **32,** 265-72 (1978).

28.Iwasaki, K. & Omura, T. Electron tomography of the supramolecular structure of virus-infected cells. *Current Opinion in Structural Biology* **20,** 632-9 (2010).

29.Kopek, B. G., Perkins, G., Miller, D. J., Ellisman, M. H. & Ahlquist, P. Three-dimensional analysis of a viral RNA replication complex reveals a virus-induced mini-organelle. *PLoS Biol.* **5,** e220 (2007).

30.Risco, C. *et al.* Three-Dimensional Imaging of Viral Infections. *Annual Review of Virology* **1,** 453 (2014).

31.Chu, H. Y. & Englund, J. A. Respiratory syncytial virus disease: prevention and treatment. *Current Topics in Microbiology and Immunology* **372,** 235-58 (2013).

32.Li, D. *et al.* Association of respiratory syncytial virus M protein with viral nucleocapsids is mediated by the M2-1 protein. *J. Virol.* **82,** 8863-70 (2008).

33.Tran, T. *et al.* The respiratory syncytial virus M2-1 protein forms tetramers and interacts with RNA and P in a competitive manner. *J. Virol.* **83,** 6363-74 (2009).

34.Blondot, M. *et al.* Structure and functional analysis of the RNA- and viral phosphoprotein-binding domain of respiratory syncytial virus M2-1 protein. *PLoS Pathog.* **8,** e1002734 (2012).

35.Seisenberger, G. *et al.* Real-time single-molecule imaging of the infection pathway of an adeno-associated virus. *Science* **294,** 1929-32 (2001).

36.Brandenburg, B. *et al.* Imaging poliovirus entry in live cells. *PLoS Biol.* **5,** e183 (2007).

37.Vaughan, J. C., Brandenburg, B., Hogle, J. M. & Zhuang, X. Rapid actin-dependent viral motility in live cells. *Biophysical journal* **97,** 1647-56 (2009).

38.Schelhaas, M. *et al.* Entry of human papillomavirus type 16 by actin-dependent, clathrin- and lipid raft-independent endocytosis. *PLoS Pathog.* **8,** e1002657 (2012).

39.Lakadamyali, M., Rust, M. J., Babcock, H. P. & Zhuang, X. Visualizing infection of individual influenza viruses. *Proc. Natl. Acad. Sci. U.S.A.* **100,** 9280-5 (2003).

40.Sun, E., He, J. & Zhuang, X. Dissecting the role of COPI complexes in influenza virus infection. *J. Virol.* **87,** 2673-85 (2012).

41.Saxton, M. J. Single-particle tracking: models of directed transport. *Biophysical journal* **67,** 2110 (1994).

42.van der Schaar, H. M. *et al.* Dissecting the cell entry pathway of dengue virus by single-particle tracking in living cells. *PLoS Pathog.* **4,** e1000244 (2008).

43.Coller, K. E. *et al.* RNA interference and single particle tracking analysis of hepatitis C virus endocytosis. *PLoS Pathog.* **5,** e1000702 (2009).

44.Nanbo, A. *et al.* Ebolavirus is internalized into host cells via macropinocytosis in a viral glycoprotein-dependent manner. *PLoS Pathog.* **6,** e1001121 (2010).

45.Chen, C. & Zhuang, X. Epsin 1 is a cargo-specific adaptor for the clathrin-mediated endocytosis of the influenza virus. *Proc. Natl. Acad. Sci. U.S.A.* **105,** 11790-5 (2008).

46.Sakai, T. *et al.* Dual wavelength imaging allows analysis of membrane fusion of influenza virus inside cells. *J. Virol.* **80,** 2013-8 (2006).

47.Rust, M. J., Lakadamyali, M., Zhang, F. & Zhuang, X. Assembly of endocytic machinery around individual influenza viruses during viral entry. *Nat. Struct. Mol. Biol.* **11,** 567-73 (2004).

48.Krzyzaniak, M. A., Zumstein, M. T., Gerez, J. A., Picotti, P. & Helenius, A. Host cell entry of respiratory syncytial virus involves macropinocytosis followed by proteolytic activation of the F protein. *PLoS Pathog.* **9,** e1003309 (2013).

49.Jouvenet, N., Bieniasz, P. D. & Simon, S. M. Imaging the biogenesis of individual HIV-1 virions in live cells. *Nature* **454,** 236-40 (2008).

50.Jouvenet, N., Simon, S. M. & Bieniasz, P. D. Imaging the interaction of HIV-1 genomes and Gag during assembly of individual viral particles. *Proc. Natl. Acad. Sci. U.S.A.* **106,** 19114-9 (2009).

51.Hallak, L. K., Collins, P. L., Knudson, W. & Peeples, M. E. Iduronic acid-containing glycosaminoglycans on target cells are required for efficient respiratory syncytial virus infection. *Virology* **271,** 264-75 (2000).

52.Schwanhäusser, B. *et al.* Global quantification of mammalian gene expression control. *Nature* **473,** 337-42 (2011).

53.Martin, K. C. & Ephrussi, A. mRNA localization: gene expression in the spatial dimension. *Cell* **136,** 719-30 (2009).

54.Sonenberg, N. & Hinnebusch, A. G. Regulation of translation initiation in eukaryotes: mechanisms and biological targets. *Cell* **136,** 731-45 (2009).

55.Simone, L. E. & Keene, J. D. Mechanisms coordinating ELAV/Hu mRNA regulons. *Current Opinion in Genetics & Development* **23,** 35-43 (2013).

56.Eisfeld, A. J., Neumann, G. & Kawaoka, Y. At the centre: influenza A virus ribonucleoproteins. *Nature Reviews Microbiology* **13,** 28-41 (2014).

57.Sundell, C. L. & Singer, R. H. Requirement of microfilaments in sorting of actin messenger RNA. *Science* **253,** 1275-7 (1991).

58.Long, R. M., Elliott, D. J., Stutz, F., Rosbash, M. & Singer, R. H. Spatial consequences of defective processing of specific yeast mRNAs revealed by fluorescent in situ hybridization. *Rna* (1995).

59.Bassell, G. J., Powers, C. M., Taneja, K. L. & Singer, R. H. Single mRNAs visualized by ultrastructural in situ hybridization are principally localized at actin filament intersections in fibroblasts. *J. Cell Biol.* **126,** 863-76 (1994).

60.Bertrand, E. *et al.* Localization of ASH1 mRNA particles in living yeast. *Mol. Cell* **2,** 437-45 (1998).

61.Fusco, D. *et al.* Single mRNA molecules demonstrate probabilistic movement in living mammalian cells. *Curr. Biol.* **13,** 161-7 (2003).

62.Shav-Tal, Y. Dynamics of Single mRNPs in Nuclei of Living Cells. *Science* **304,** 1797 (2004).

63.Yamagishi, M., Ishihama, Y., Shirasaki, Y., Kurama, H. & Funatsu, T. Single-molecule imaging of β-actin mRNAs in the cytoplasm of a living cell. *Experimental Cell Research* **315,** 1142 (2009).

64.Grünwald, D. & Singer, R. H. In vivo imaging of labelled endogenous β-actin mRNA during nucleocytoplasmic transport. *Nature* **467,** 604 (2010).

65.Daigle, N. & Ellenberg, J. LambdaN-GFP: an RNA reporter system for live-cell imaging. *Nat. Methods* **4,** 633-6 (2007).

66.Lange, S. *et al.* Simultaneous transport of different localized mRNA species revealed by live-cell imaging. *Traffic* **9,** 1256-67 (2008).

67.You, M. & Jaffrey, S. R. Structure and Mechanism of RNA Mimics of Green Fluorescent Protein. *Annual Review of Biophysics* **44,** 187-206 (2015).

68.Paige, J. S., Wu, K. Y. & Jaffrey, S. R. RNA mimics of green fluorescent protein. *Science* **333,** 642-6 (2011).

69.Strack, R. L., Disney, M. D. & Jaffrey, S. R. A superfolding Spinach2 reveals the dynamic nature of trinucleotide repeat-containing RNA. *Nat. Methods* **10,** 1219-24 (2013).

70.Filonov, G. S., Moon, J. D., Svensen, N. & Jaffrey, S. R. Broccoli: rapid selection of an RNA mimic of green fluorescent protein by fluorescence-based selection and directed evolution. *Journal of the American Chemical Society* **136,** 16299-308 (2014).

71.Ozawa, T. *et al.* Imaging dynamics of endogenous mitochondrial RNA in single living cells. *Nat. Methods* **4,** 413-9 (2007).

72.Yamada, T., Yoshimura, H., Inaguma, A., Ozawa, T. & Ozawa, T. Visualization of nonengineered single mRNAs in living cells using genetically encoded fluorescent probes. *Analytical Chemistry* **83,** 5708-14 (2011).

73.Tyagi, S. & Kramer, F. R. Molecular Beacons: Probes that Fluoresce upon Hybridization. *Nat. Biotechnol.* **14,** 303 (1996).

74.Bratu, D. P., Cha, B., Mhlanga, M. M., Kramer, F. R. & Tyagi, S. Visualizing the distribution and transport of mRNAs in living cells. *Proc. Natl. Acad. Sci. U.S.A.* **100,** 13308-13 (2003).

75.Tyagi, S. & Alsmadi, O. Imaging native beta-actin mRNA in motile fibroblasts. *Biophysical journal* **87,** 4153-62 (2004).

76.Molenaar, C. *et al.* Linear 2' O-Methyl RNA probes for the visualization of RNA in living cells. *Nucleic Acids Res.* **29,** E89-9 (2001).

77.Spiller, D. G., Giles, R. V., Grzybowski, J., Tidd, D. M. & Clark, R. E. Improving the intracellular delivery and molecular efficacy of antisense oligonucleotides in chronic myeloid leukemia cells: a comparison of streptolysin-O …. *Blood* (1998).

78.Santangelo, P. J. *et al.* Single molecule-sensitive probes for imaging RNA in live cells. *Nat. Methods* **6,** 347-9 (2009).

79.Lifland, A. W., Zurla, C., Yu, J. & Santangelo, P. J. Dynamics of native β-actin mRNA transport in the cytoplasm. *Traffic* **12,** 1000-11 (2011).

80.Hell, S. W. & Wichmann, J. Breaking the diffraction resolution limit by stimulated emission: stimulated-emission-depletion fluorescence microscopy. *Optics Letters* **19,** 780-782 (1994).

81.van de Linde, S. *et al.* Direct stochastic optical reconstruction microscopy with standard fluorescent probes. *Nat Protoc* **6,** 991-1009 (2011).

82.Lučič, V., Rigort, A. & Baumeister, W. Cryo-electron tomography: the challenge of doing structural biology in situ. *J. Cell Biol.* **202,** 407-19 (2013).

83.Göttfert, F., Wurm, C. A., Mueller, V., Berning, S. & Cordes, V. C. Coaligned dual-channel STED nanoscopy and molecular diffusion analysis at 20 nm resolution. *Biophysical journal* (2013).

84.Löschberger, A. *et al.* Super-resolution imaging visualizes the eightfold symmetry of gp210 proteins around the nuclear pore complex and resolves the central channel with nanometer resolution. *J. Cell. Sci.* **125,** 570-5 (2012).

85.Yahav, T., Maimon, T., Grossman, E., Dahan, I. & Medalia, O. Cryo-electron tomography: gaining insight into cellular processes by structural approaches. *Current Opinion in Structural Biology* **21,** 670-7 (2011).

CHAPTER 2

FLUORESCENT LABELING OF RSV

The work presented here is excerpted from the following publications: Alonas, E., Lifland, A.W., Gudheti, M., Vanover, D., Jung, J., Zurla, C., Kirschman, J., Fiore, V.F., Douglas, A., Barker, T.H., Yi, H., Wright, E.R., Crowe Jr., J.E., & Santangelo, P.J. Combining single RNA sensitive probes with subdiffraction-limited and live-cell imaging enables the characterization of virus dynamics in cells. *ACS Nano* **8**, 302-15 (2014); Lifland, A.W., Jung, J., Alonas, E., Zurla, C., Crowe Jr., J.E., & Santangelo, P.J. Human respiratory syncytial virus nucleoprotein and inclusion bodies antagonize the innate immune response mediated by MDA5 and MAVS. *J. Virol.* **84**, 12274-85 (2012); and Kiss, G., Holl, J.M., Williams, G.M., Alonas, E., Vanover, D., Lifland, A.W., Gudheti, M., Guerrero-Ferreira, R.C., Nair, V., Yi, H., Graham, B.S., Santangelo, P.J., & Wright, E.R. Structural analysis of respiratory syncytial virus reveals the position of M2-1 between the matrix protein and the ribonucleoprotein complex. *J. Virol.* **88**, 7602-17 (2014).

Background

Previous methods for labeling viruses fluorescently have several shortcomings. Lipophilic membrane dyes will insert themselves into all membranes and do not reveal any information as to whether or not a particular virion contains the necessary factors that make it replication competent. Moreover, for a fusogenic, enveloped virus like RSV, the ability to observe virus replication ends after fusion[1], when the viral membrane fuses with the membrane, allowing the dye to diffuse throughout the rest of the plasma membrane. We have also shown that the membrane dye DiO does not integrate well into RSV filamentous virions.

Fluorescent fusion proteins have different advantages and disadvantages. While generating a fluorescent protein allows for the specific labeling of one viral protein, the expression and function of the fusion protein might not be the same as the native one. Indeed, most viral proteins have amino acid sequences that are of similar length as most fluorescent proteins, so insertion of the fluorescent protein leads to a large proportional increase in the genome size. Ultimately, this can manifest itself as an inability to rescue the virus. For RSV specifically, there has been only a few fluorescent protein versions created to date; the SH gene was deleted and replaced by a fluorescent protein, such as GFP.[2]

RNA specific dyes suffer from similar drawbacks. While they enable the observation of the viral ribonucleoprotein, they are not specific for a particular RNA and might diffuse to other cellular RNAs in the cytoplasm after virion entry. They have also largely been used only in nonenveloped viruses, such as the picornavirus polio[3], and so their performance with enveloped viruses is largely unknown.

Fluorescent fusion RNA binding proteins might seem to be a solution to the specificity problem by binding to RNA secondary structure motifs (in the case of MS2-GFP these are hairpins) that are introduced into the virion genome. This has been done for the enveloped HIV virus.[4,5] However, introducing several hairpins into a relatively small genome poses the same problem as introducing a fluorescent protein encoding sequence. Moreover, the need to express both the MS2-GFP and the RNA at high copy number might lead to false conclusions due to changed protein:RNA stoichiometry. For instance, it is thought that the RSV genome is helix wrapped entirely in N protein[6,7], introducing too many motifs could disrupt this arrangement and potentially prevent replication.

Clearly, there is a need for a new approach. This approach would be sensitive enough to detect single genomic RNAs of RSV, enable observation for long periods of time, and would not significantly interfere with viral replication (as defined by changes in

viral morphology and/or logarithmic decreases in titer). The multiply labeled, tetravalent RNA imaging probe, first described in Santangelo *et al.* 2009[8] satisfies most of these criteria, as the following text should demonstrate. Furthermore, the use of this probe enabled variations in chemistry that can be used with different imaging techniques.

In order to test this approach, we developed a protocol for isolated single filamentous virions on glass. We examined these not only for RNA content, but the content of viral proteins and other host cell factors of interest.

Isolating single virions

We started this process by demonstrating that we could isolate single RSV virions on glass and immunostain for specific markers. Using poly-L-lysine coated coverslips, we centrifuged virus that had been previously clarified using membrane filters onto coverslips and examined them for the presence of viral proteins (**Fig. 2.1**). The membrane filter sizes were chosen to correspond to those previously described for the characterization of RSV budding from the apical side of polarized Vero cells.[9] We were able to specifically detect viral proteins on the inside and the outside of the viral filaments, depending on whether or not the filament was first permeabilized with Triton X-100.

Next, we examined whether or not we were capturing all of the particles in our clarified virus preparation with centrifugation. To do this, we took the same sample of clarified virus and iteratively centrifuged it onto fresh poly-L-lysine coated coverslips (**Fig 2.2**). We were able to capture the large majority of particles on the first centrifugation, ensuring that the particles on the coverslip were indeed representative of the particles in the clarified virus sample.

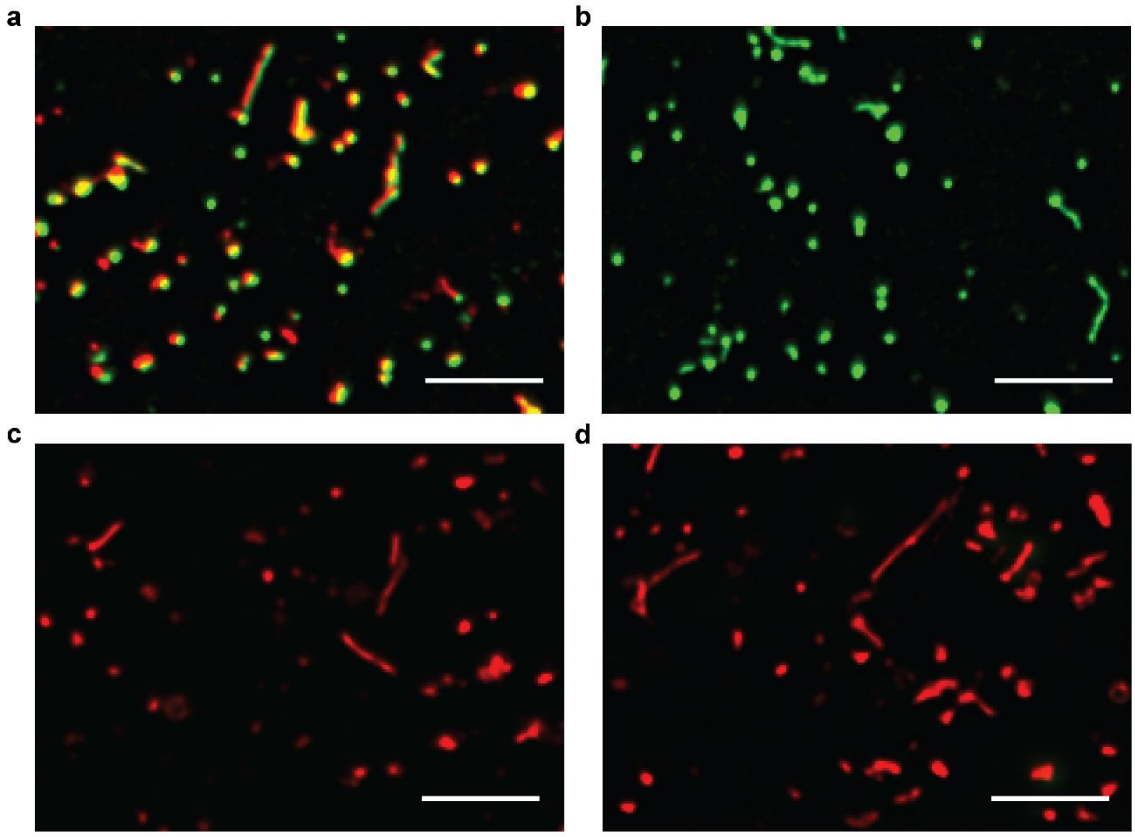

Figure 2.1 Antibody staining controls for RSV virions on coverslips. Merged image of RSV virions immunostained for RSV N (green) and RSV F (red) (**a**). No primary control for RSV F (**b**). No primary control for RSV N (**c**). No permeabilization with triton X-100 (**d**). Single-plane, widefield deconvolved image shown. Scale bars 5 µm.

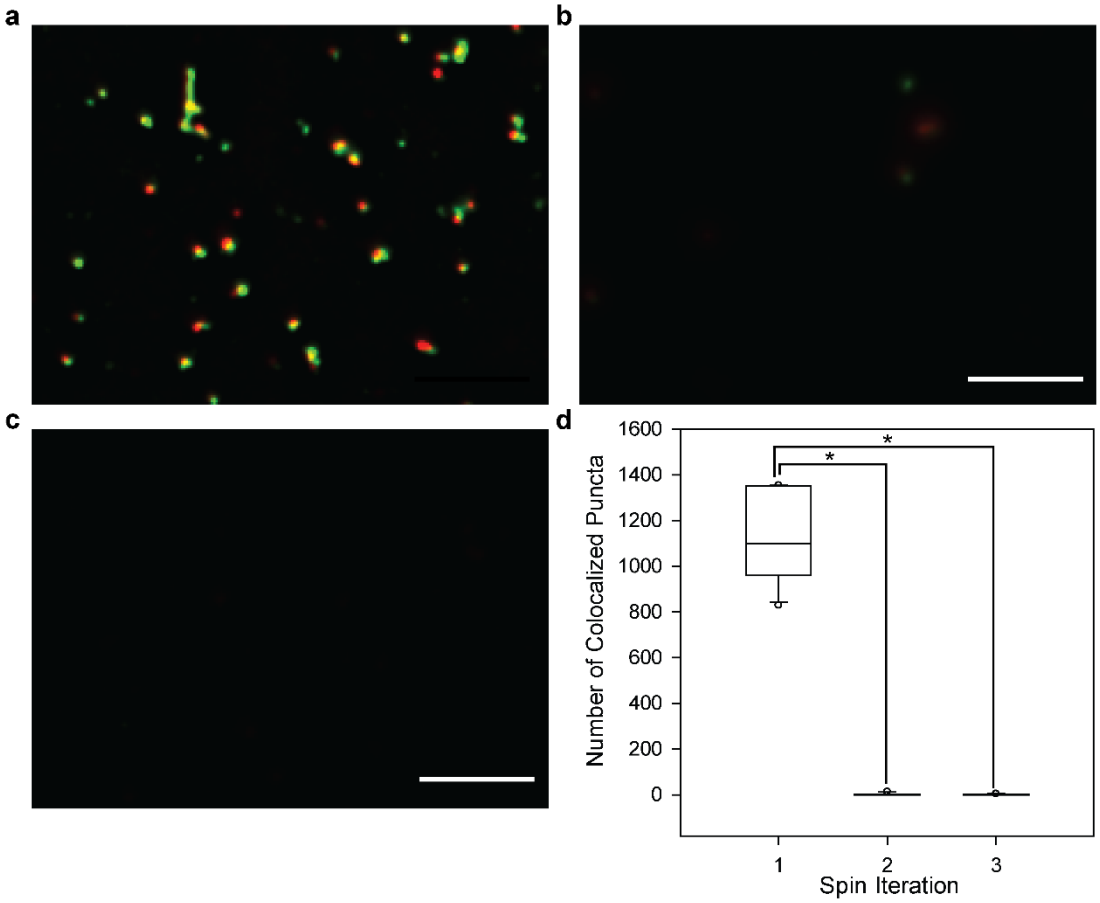

Figure 2.2. Iterative centrifugation of the same RSV sample. RSV virions immunostained for N and F captured on the first spin (**a**). RSV virions captured on the second spin (**b**). RSV virions captured on the third spin(**c**). Box-and-whisker plot of the number of virions captured on each spin per microscopic field (Kruskal-Wallis one way ANOVA on ranks with post-hoc Tukey test for multiple comparisons, * indicates $P < 0.05$) (**d**). Single-plane, widefield deconvolved image shown. Scale bars 5 µm.

Staining for other viral proteins in isolated virions

Since we now had an established method for examining the protein localization within individual filamentous virions, we decided to examine what the localization of other viral proteins and some host proteins. In particular, we were curious as to whether or not the alternate reading frame of the RSV matrix protein, M2-1, is actually a structural part of the mature virion. M2-1 has previously been described as a transcription processivity factor for the L polymerase,[10]but more recently it has been shown to interact with the phosphoprotein P[11] and associate with the matrix protein M[12]. We began by examining the matrix protein late in the infection within cells (**Fig. 2.3**). While the dynamic range within the sample becomes an issue, given the high expression level of M, it is clear that there is indeed M2-1 localized in the filamentous virions when compared to no-primary-antibody cells to control for secondary antibody crosstalk (**Fig. 2.4**). However, the M2-1 was difficult to detect, and those filaments on the cell surface are not necessarily the ones that will be isolated from the cell and be infectious.

That being said, we applied our technique of staining isolated filamentous virions to this problem. Additionally, we used an in situ proximity ligation assay to detect protein-protein interactions on the order of 40nm, which is below the diffraction limit of conventional optical microscopy. Performing PLA for M-M2-1 interactions of isolated virions revealed the presence of interactions between these two proteins (**Fig. 2.5**) when compared to control cells (**Fig. 2.6**). Clearly, there is M2-1 within close proximity to M within the isolated virus.

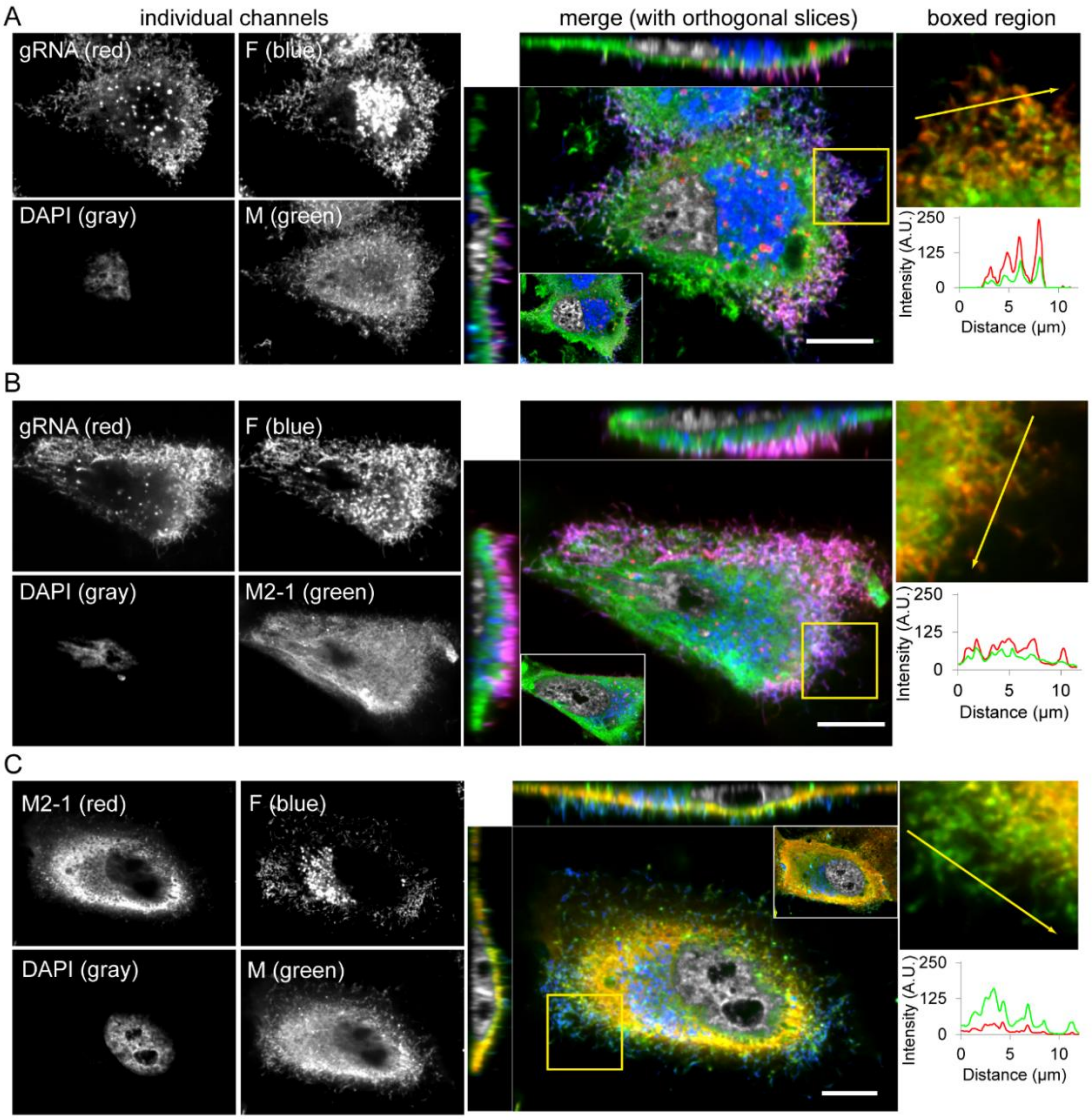

Figure 2.3 M and M2-1 immuno-staining and confocal fluorescence microscopy. (A) HEp2-cells infected with RSV A2 (M.O.I. 1) had RNA imaging probes targeting the RSV genomic RNA (red) delivered to them at 24 hr P.I. and were fixed and immuno-stained for the viral F (blue) and M (green) proteins. Also included is a DAPI nuclear stain (gray). To the right, a merged image of an XY plane near the top of the cell is shown with orthogonal slices through the middle of the cell. Inset shows merged image of an XY plane near the bottom of the cell (to emphasize regularity of cell nuclei); boxed region shows magnified image of filamentous virions protruding from the cell membrane with the F and DAPI channels removed to emphasize the clarity of colocalization. Fluorescence intensity profile plot along arrow in the boxed region is also shown. (B) RSV infected HEp-2 cells with RNA imaging probes (red) and immuno-staining for viral F (blue) and M2-1 (green) proteins. (C) RSV infected HEp-2 cells immuno-stained for viral F (blue), M (green), and M2-1 (red) proteins. Single optical plane, laser scanning confocal images shown. Scale bars 10 μm.

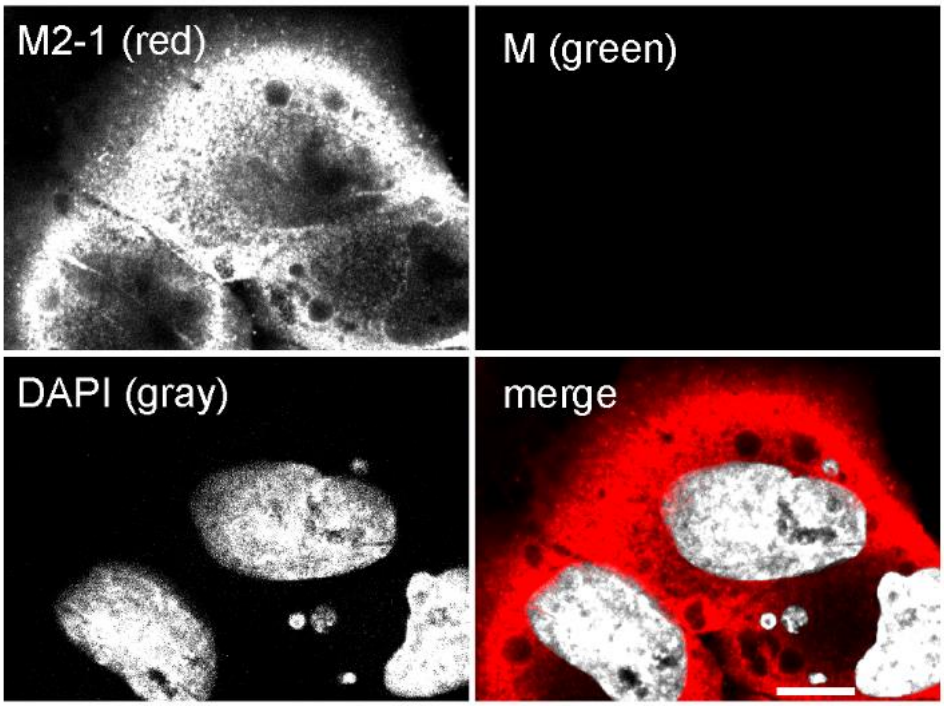

Figure 2.4. Antibody staining controls. In order to test the species conversion antibody staining protocol, the second primary antibody (anti-M) was replaced with a sham solution of PBS.

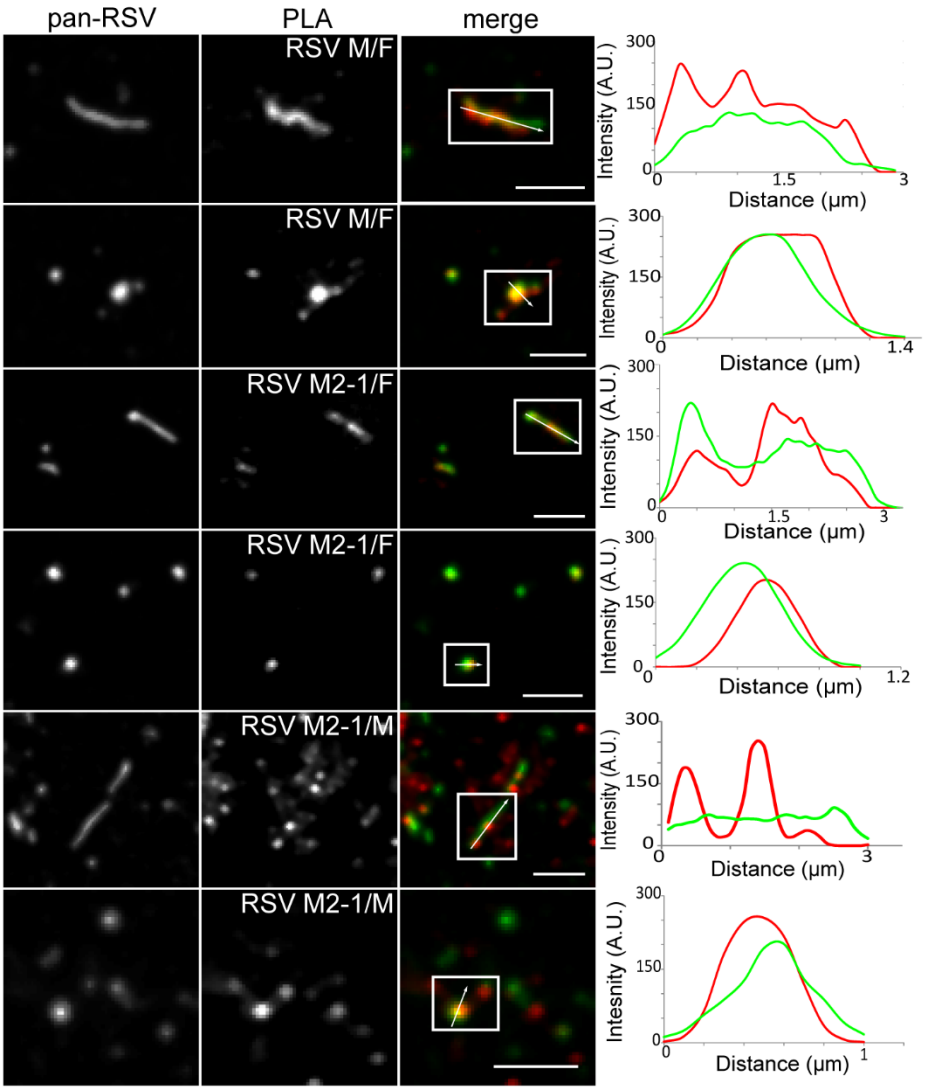

Figure 2.5 Proximity ligation assay between F and M, F and M2-1, and M and M2-1. RSV virions on glass were assayed for interactions between F and M, F and M2-1, and M and M2-1 by PLA. The virions were also immuno-stained for pan-RSV for context. Note that PLA signal is only an indication of two molecules in close proximity and may not colocalize with staining. From left to right, Column 1 shows pan-RSV staining. Column 2 shows PLA signal between F and M (panel A), F and M2-1 (panel B), and M and M2-1 (panel C). Column 3 shows the merged image of columns 1 and 2 with pan-RSV signal in green and PLA signal in red. Column 4 shows the fluorescence intensity profile plot along the arrow. First rows show filamentous virion morphologies while second rows show spherical virion morphologies. Boxes indicate viral particles of interest; scale bars 2.5 μm. Experiments and Figure by DV in consultation with EJA.

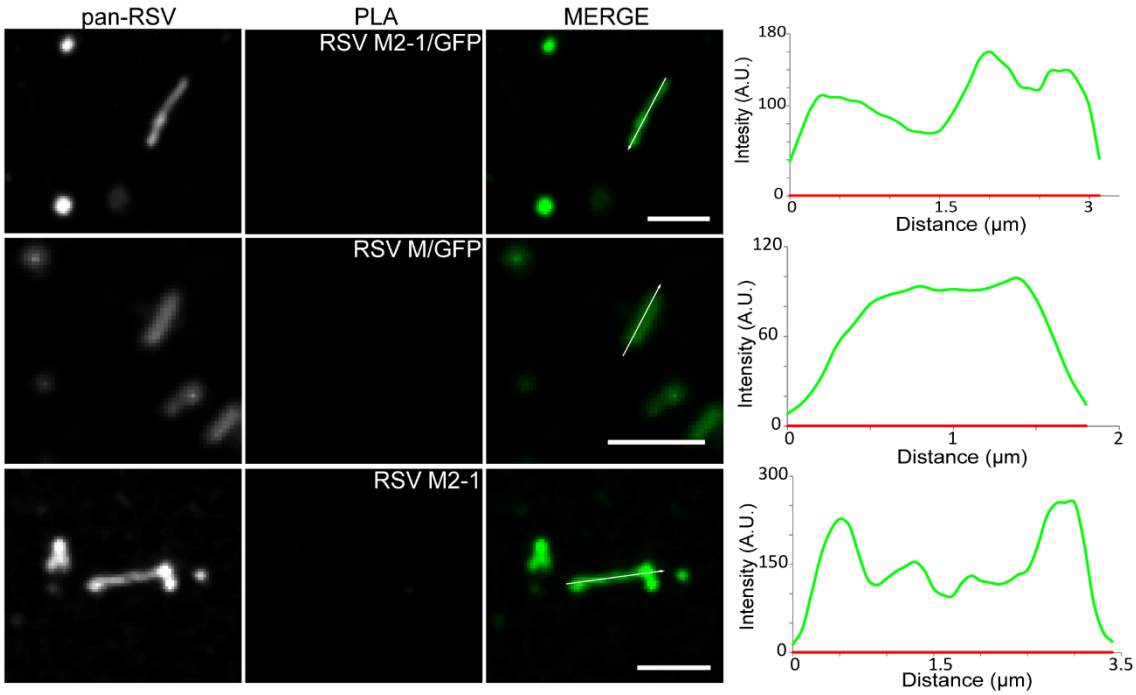

Figure 2.6. Isolated virion PLA controls. (left column) Filaments were stained with a pan RSV antibody to show the extent of the filament. (middle column) PLA signal between the indicated pairs on antibodies, note that there is no GFP present in the cell in this example, so the GFP antibody serves as an isotype control. (right column) Merged images of the left and middle column with adjacent fluorescence intensity profiles drawn along the filament. Scale bar 5μm.

Staining for host cell proteins

Continuing further along in this direction, we decided to examine the presence of host cell proteins within the isolated filamentous virions. Of particular interest was a group of proteins known as the RIG-I like receptors (RLRs). This group of proteins recognizes single and double stranded nucleic acids and have been realized to be part of the innate immune response to virus[13]. In the case of RSV, the nonstructural proteins NS1 and NS2 had previously been shown to influence this response.[14] Given that the RSV genome enters the cytoplasm where these RLRs are located, we decided to look for RLR proteins in the isolated filamentous virions to see if they might be localized in similar places to the genome. Isolation and staining of the filamentous virions revealed that of three RLRs examined, only melanoma differentiation-associated gene 5 (MDA5) was localized to the filamentous virions (**Fig. 2.7**). This suggests that MDA5 interacts with one of the viral components, which we demonstrate later in that particular publication to be RSV N.

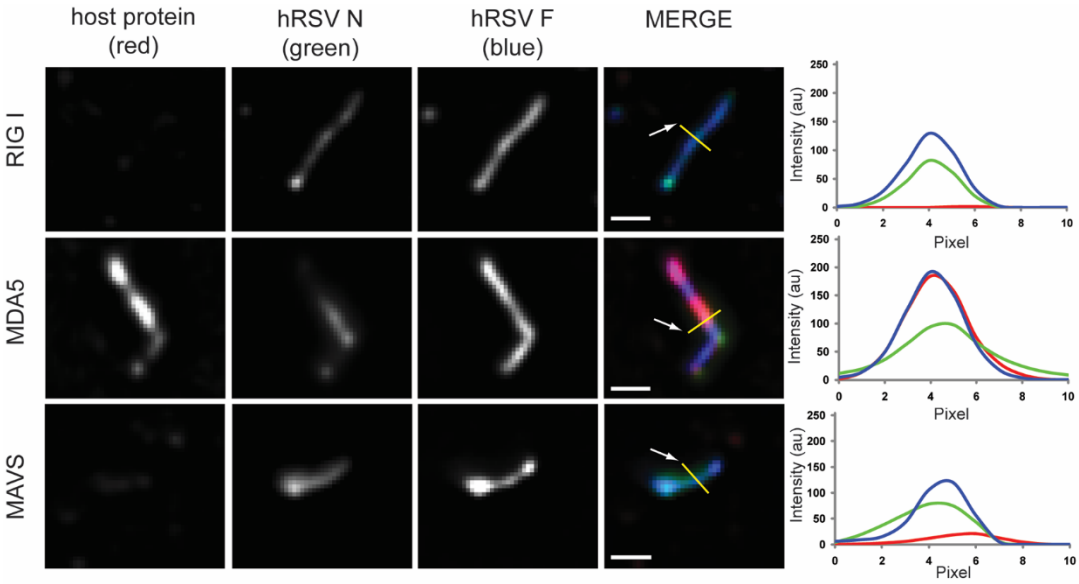

Figure 2.7 MDA5 colocalized with isolated viral filaments. HEp-2 cells we infected with RSV strain A2 at an MOI=0.1 and viral filaments were isolated 4 dpi. Viral filaments were isolated by filtration and adsorbed onto coverglass for immunostaining. Column 1 shows the host protein RIG-I, MDA5, or MAVS, red in the merge. Column 2 shows RSV N staining, green in the merge. Column 3 shows RSV F staining, blue in the merge. Column 4 shows the merge. Column 5 shows an intensity profile through the lines in the merged images, arrow denotes pixel number 1. Scale bar is 1 µm.

Labeling the genomic RNA of RSV

Before we begin, it should be noted that we did attempt to label the virus using the membrane stain DiO, despite the previously mentioned drawbacks. Unlike another group which used DiO to stain spherical RSV virions[1], we found that DiO did not stain the isolated filamentous virions (**Fig 2.8A**), nor infected cells (**Fig 2.8B**). However, DiO had no trouble staining noninfected cells (**Fig 2.8C**). One reason for this could be the high number of viral glycoproteins in the membrane exclude the membrane dye. Additionally, the fact that DiO does not yield any information about the nucleoprotein contents of the virus led us to abandon this approach in favor of MTRIPs.

A brief description of the method, with accompanying fluorescent images at each step in the process, is shown in (**Fig 2.9**). Briefly, MTRIPs were assembled by incubating biotinylated, fluorescently-labeled oligonucleotides with neutravidin, and excess oligonucleotides were removed by filtration[8]. These MTRIPs, which bind *via* Watson-Crick base-pairing to a short, repeated sequence within the intergenic-gene start regions of the RSV genome, were delivered into RSV infected cells *via* reversible streptolysin-O permeabilization, a pore-forming toxin of *Streptococcus pyogenes*. The MTRIPs bound to the RSV gRNA and were assembled into cell-associated virions on the cell surface. Virus was harvested from cells by scraping, aliquoting, and storage at -80 °C. After thawing an aliquot, virus was centrifuged through centrifugal membrane filters to remove cell debris and isolate filamentous virions, as well as spherical-like particles.[9]

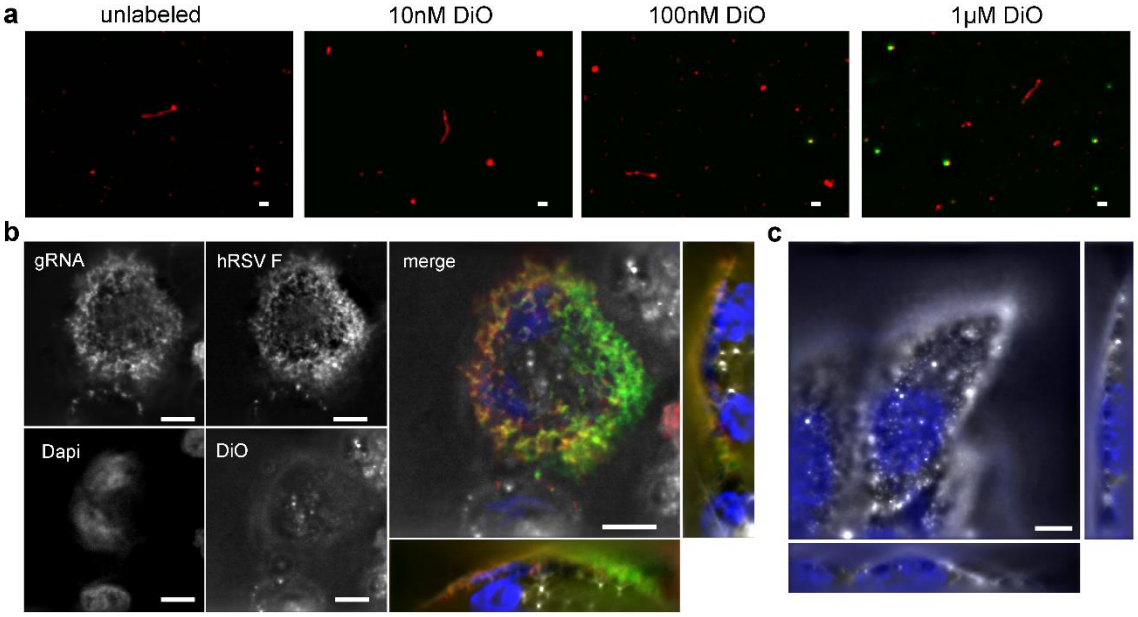

Figure 2.8 DiO labeling of RSV filamentous virions. MTRIP-labeled RSV virions were shaken with various concentrations of DiO before being filtered and centrifuged onto poly-L-lysine coated coverslips and imaged (**a**). RSV infected HEp-2 cells (MOI 1, 48 hr PI) with 30nM MTRIP probes (red), a primary dye-labeled antibody against F protein (green), DiO (white), and nuclear stain (blue) (**b**). A noninfected cell for comparison (**c**). Single-plane, widefield deconvolved images shown. Scale bars 1 μm and 10 μm for (**a**) and (**b**) (**c**), respectively.

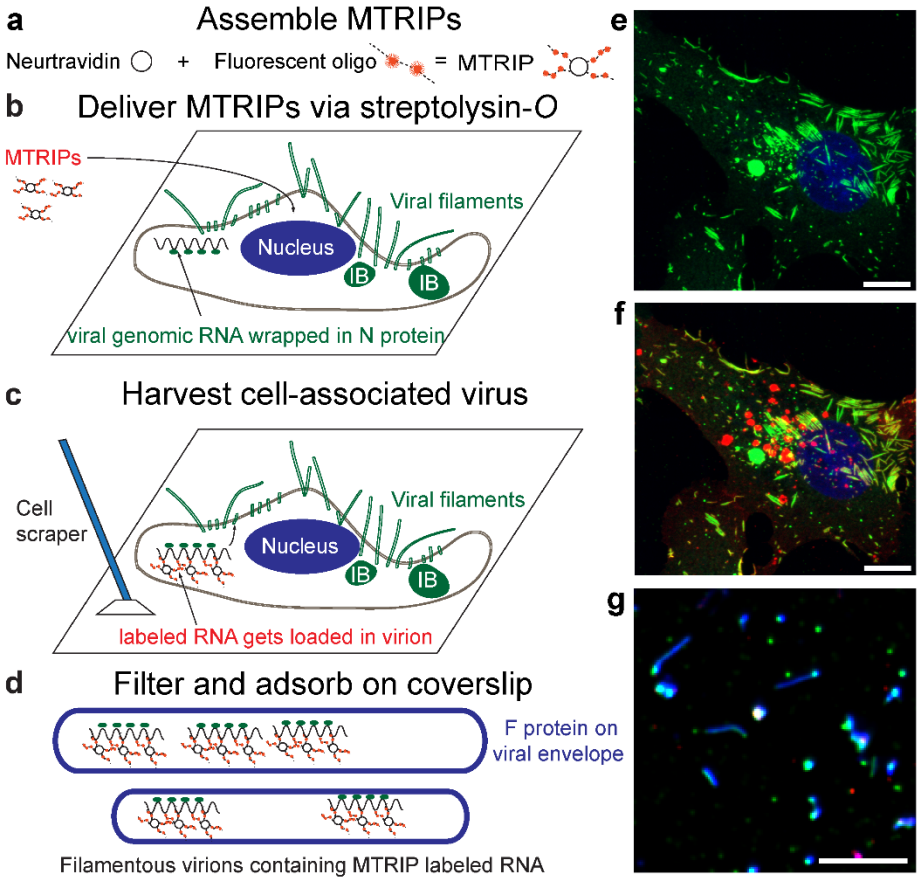

Figure 2.9. Illustration of MTRIP delivery and virus isolation methodology. (**A**) The MTRIP design consists of oligonucleotides that are internally labeled with fluorophores (red dots with carbon linkers on deoxy-thymine bases) and biotinylated on the 5' end (green dot). These oligonucleotides are tetramerized by mixing them with neutravidin (blue circle). The actual probe sequence is shown. (**B**) RSV is allowed to infect HEp-2 cells for 96 hr before MTRIP probe delivery. A cartoon cell is shown on the left and a cartoon viral filament sticking out of the cell membrane is shown on the right. A single intergenic sequence of the RSV genome is shown just below the filament (the ellipsis on either end of the sequence represent the other 16kb of the RSV genome). (**C**) During probe delivery, streptolysin-O is used to permeabilize the cell membrane (step 1) allowing MTRIP probes to diffuse into the cell cytoplasm and bind to the intergenic sites of the RSV genome *via* Watson-Crick base-pairing (step 2). (**D**) Streptolysin-O is removed allowing the pores in the cell membrane to close and the RSV genome/MTRIP complex to be loaded into the filamentous virion (step1). The labeled virions are detached from the cell by scraping and can be aliquoted and frozen for further experiments (step 2).

Validation of labeling

In order to validate that MTRIP labeling did not significantly affect the virus, we monitored viral mRNA replication and protein expression during the first cycle of infection. We performed real-time qRT-PCR for nascent RSV phosphoprotein (P), polymerase (L), and major glycoprotein (G) mRNA at three time points post-infection (6, 12, and 24 hr post infection) and showed that there were no statistically significant changes in the transcript quantities generated by the MTRIP labeled virus compared to unlabeled, wild-type virus at any of the timepoints examined (**Fig. 2.10A**). We also performed Western blotting for the P and G proteins at 12 and 24 hr post infection to confirm that infection with the labeled virus expressed similar amounts of protein (**Fig. 2.10B**). Blotting for the P protein produced a single band at the expected molecular weight for infections with labeled and unlabeled viruses. Blotting for the G protein produced multiple bands for the fully glycosylated and partially glycosylated versions of the protein for infections with labeled and unlabeled viruses.[15] We further quantified the amounts of protein using densitometry and found that at the timepoints examined, there were no statistically significant changes in the amount of either P or G between the labeled and unlabeled infections (**Fig. 2.10C**). We also spot-checked the total amount of protein produced at the 12 hr post infection timepoint by ELISA, using a polyclonal antibody against the whole virus (**Fig. 2.10D**). No significant differences in the amounts of protein were detected using this method either. Finally, we checked the virus titer later in the infection (96 hr post infection) to ensure that labeling did not affect the long term kinetics of virus growth (**Fig. 2.10E**). Both unlabeled and labeled viruses reached titers on the order of 10^6 pfu/ml, the maximum achievable titer without using high-density

culture systems, and were not statistically different. These results show that MTRIP labeling does not significantly affect the RSV replication cycle.

Furthermore, we examined the virus *via* transmission electron microscopy (TEM) to ensure that the labeling procedure did not affect virion morphology. We imaged cells infected with unlabeled virus, cells infected with unlabeled virus that had MTRIP probes delivered at 24 hr post infection, and cells that had been infected with labeled virus using thin section TEM (**Fig. 2.10F**). In all three cases, infected cells generated filamentous and spherical virions, with characteristic electron dense envelopes and glycoprotein "spikes" (Low magnification images). Close examination of filaments (High magnification images) reveals filamentous virions 100 nm to 200 nm in diameter and over 1 μm in length in all three cases. From these images, it appears that MTRIP delivery and labeling does not affect virion morphology.

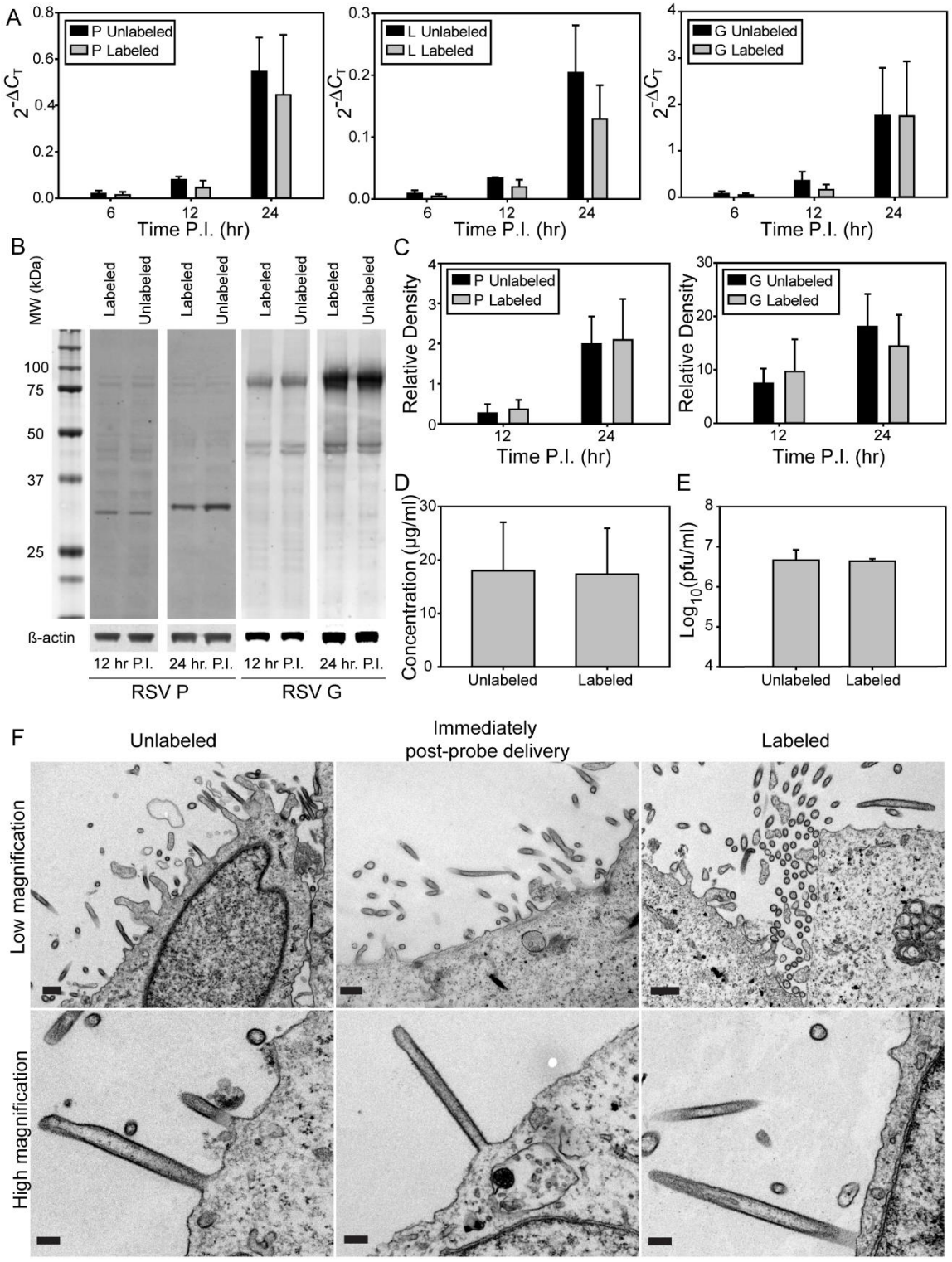

Figure 2.10. Validation of Efficient Virus Replication and Virus Morphology of MTRIP labeled virions. (**A**) Cycle threshold comparisons from real-time qRT-PCR to detect nascent RSV P, L, and G transcripts generated from infections of HEp-2 cells using labeled or unlabeled RSV (M.O.I. 0.1 at 6, 12, and 24 hr post infection). There were no statistically significant differences at any timepoint for any gene (t-test, n=3,

P>0.05). (**B**) Representative western blots for RSV P and RSV G from cells infected with labeled or unlabeled virus (M.O.I. 0.1 at 12 and 24 hr post infection) with representative molecular weight marker and β-actin loading control. (**C**) Replicate western blots were further quantified by densitometry to compare signals from labeled and unlabeled virus relative to actin loading control. There were no statistically significant differences at any timepoint (t-test, n=3, P>0.05). (**D**) Total RSV protein ELISA from HEp-2 cells infected with labeled or unlabeled virus (M.O.I. 0.1 at 12 hr post infection). There were no statistically significant differences (t-test, n=3, P>0.05). (**E**) Plaque assay results for labeled and unlabeled virus grown in HEp-2 cells to a saturation point at 96 hr post infection. There were no statistically significant differences (t-test, n=3, P>0.05). (**F**) Thin section TEM of Vero cells infected with unlabeled virus, unlabeled virus with MTRIP probes delivered immediately before fixation, or labeled virus (M.O.I. 0.1 at 24 hr post infection). Low magnification fields show the pleiomorphic nature of RSV; high magnification fields show single filamentous virions protruding from cell surface. Scale bars 0.5 μm and 0.2 μm for low and high magnification images, respectively.

We then utilized fluorescence colocalization between the immunostained N and F proteins and the MTRIP-labeled gRNA to characterize the virions on coverslips. We found that the distributions of the gRNA and N protein were discontinuous, whereas the F protein was distributed continuously (**Fig. 2.11A, B**). To further verify that MTRIP probes were inside the virions, we replaced the neutravidin core of the MTRIP with a 5 nm gold nanoparticle/streptavidin conjugate. This change allowed us to image labeled virions on glass using darkfield microscopy, after reductive silver enhancement of the gold nanoparticles (**Fig. 2.11C**). Since unbound probes were removed during centrifugation through membrane filters, the only MTRIPs in the sample were most likely inside of the virions. After isolating both neutravidin-MTRIP and gold/streptavidin-MTRIP labeled viruses and filtering to remove unbound probes, we detected a large peak in the gold/streptavidin-MTRIPs at around 620 nm, compared to the neutravidin-MTRIPs (**Fig. 2.11D**). This peak was likely due to the increased plasmon scattering[16] of the silver-enhanced particles inside the virions.

Finally, the concentration of MTRIPs was titrated and the number of particles containing gRNA and N and F was determined *via* blob colocalization[17] (**Fig. 2.11E**). The number of three-color particles appeared to saturate upon delivery of 100 nM to 500 nM MTRIPs to infected cells. Unless otherwise noted, all subsequent virus labelings were carried out with 100 nM probe. The accuracy of particle counting was confirmed by counting Tetraspeck beads of known particle density after they were centrifuged onto coverslips (**Fig 2.12**). The number of objects containing three colors was in essence a signal to noise calculation - demonstrating that as the number of "red"/probe labeled objects increased, there was an optimal maximum of the number of objects detected (**Fig.**

2.13). The number of objects, or "blobs", containing three colors was calculated using the BlobProb ImageJ plugin[17] and was used because of its extension to multiple colors and more conservative estimates of colocalization than the typical voxel based approach. The resulting numbers were within an order of magnitude of viral titers measured by plaque assay, confirming that the labeled viral particles were likely infectious virions.

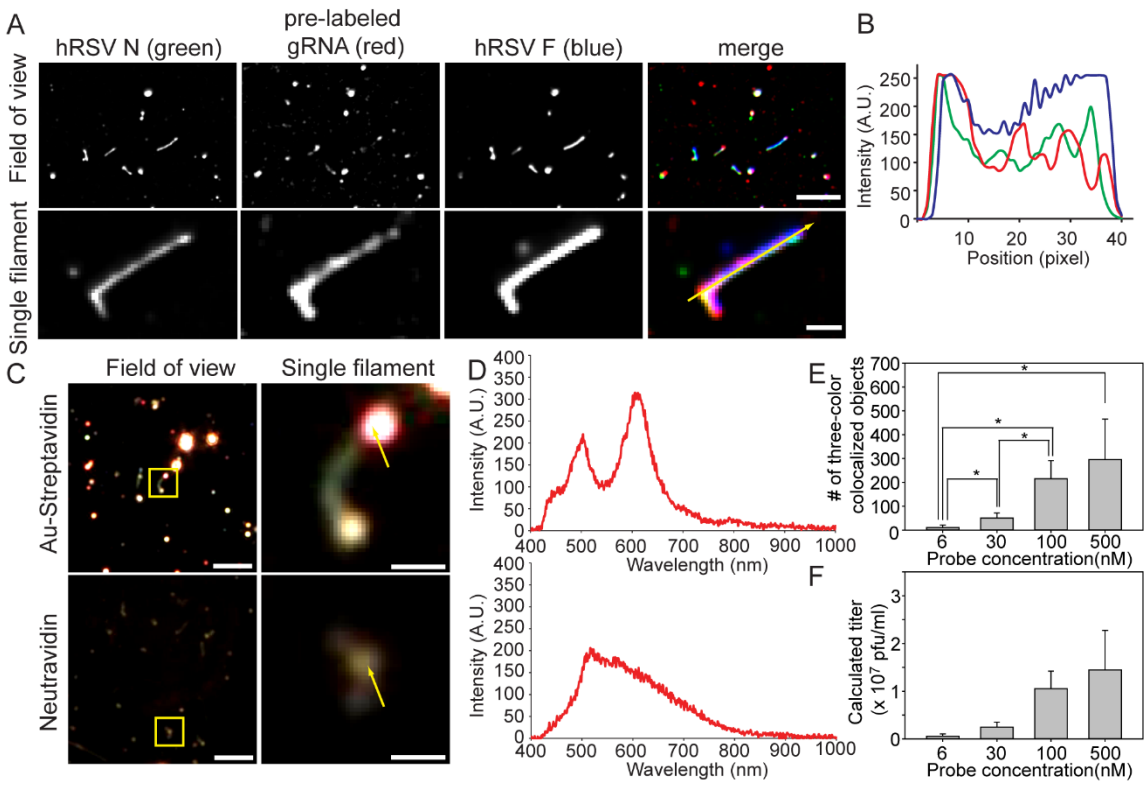

Figure 2.11 Characterization of MTRIP labeled RSV virions. (**A**) MTRIP labeled virions were immobilized on a coverglass and RSV proteins N and F were detected *via* immunofluorescence. A representative field of view and a magnified filamentous virion are shown. The RSV N (green), RSV F (blue), and labeled gRNA (red) are shown individually as well as merged. (**B**) Profile plot of the fluorescence intensity along the length of the filament shown in Figure 3A. (**C**) Darkfield images of gold-streptavidin MTRIP-labeled RSV and neutravidin MTRIP-labeled RSV. Samples were silver enhanced prior to imaging. Field of view is shown on left, boxed region indicates single filament featured in the magnified image to the right. (**D**) Spectra of light emitted from one pixel in the single filament image (indicated by arrow) for Au-Streptavidin labeled virus (top) or neutravidin labeled virus (bottom). (**E**) The effect of varying MTRIP probe concentration on the number of objects detected on coverglass from infected cells containing RSV N, RSV F, and gRNA (above, Kruskal-Wallis one-way ANOVA, * indicates $P<0.05$). (F) These numbers were used to calculate a theoretical estimate of viral titer. Single-plane, widefield deconvolved images shown in (**A**). Scale bars 5 µm and 1 µm, respectively. Single-plane, darkfield image shown in (**C**). Error bars indicate standard deviation.

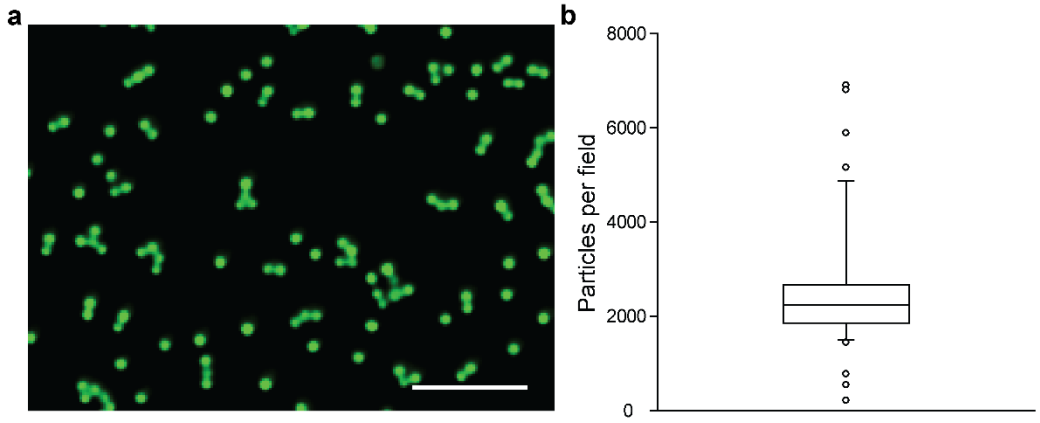

Figure 2.12. Counting of fluorescent beads per field. Tetraspeck beads of nominal diameter 0.5 µm centrifuged onto a 384 glass-bottomed well plate (**a**). Box-and-whisker plot of the number of particles per field (one-sample signed rank test, hypothesized median of 2560 particles per field based on manufacturer's particle density, well size, and CCD size, P=0.207) (**b**). Single-plane, widefield deconvolved image shown. Scale bar 5 µm.

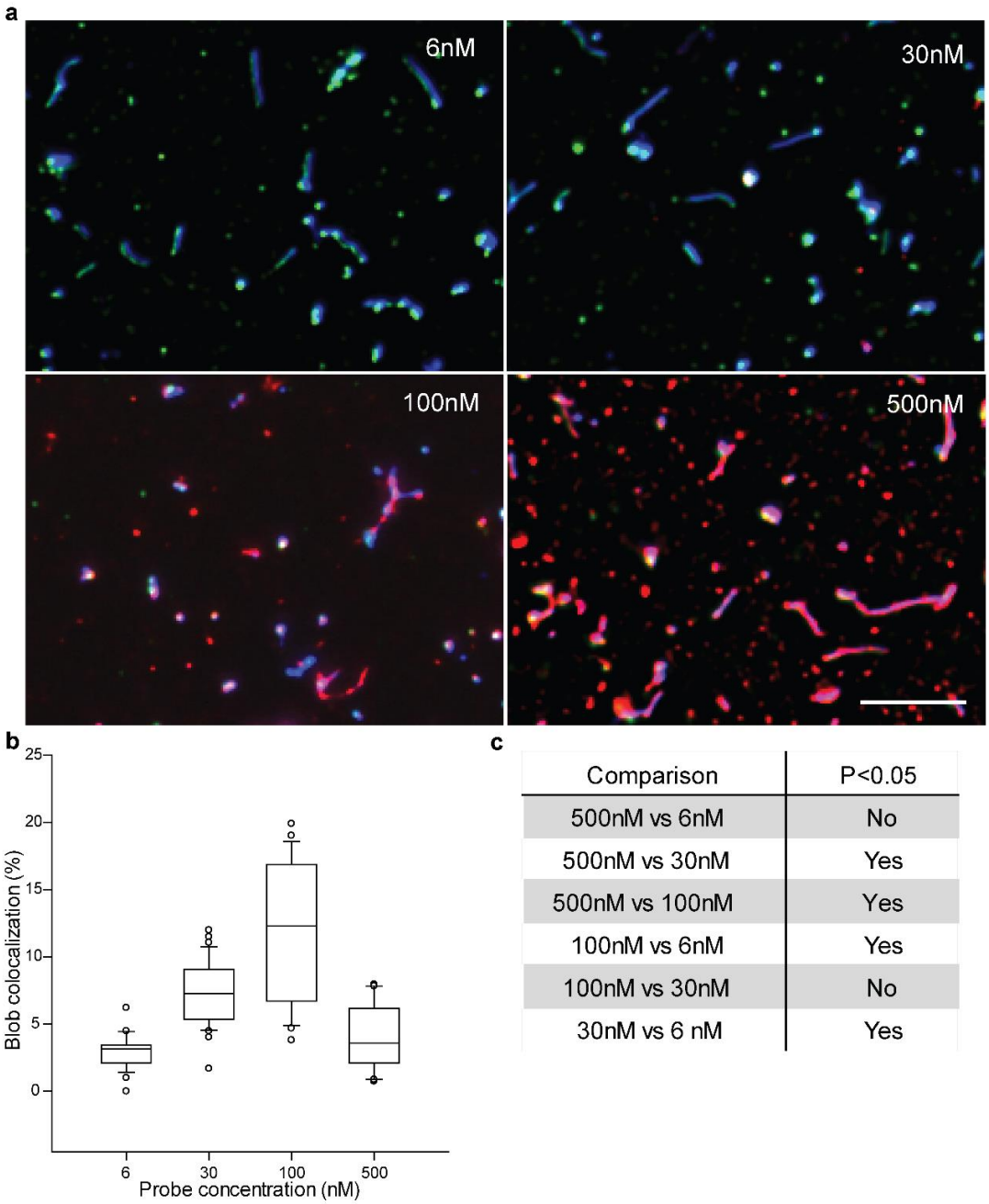

c

Comparison	P<0.05
500nM vs 6nM	No
500nM vs 30nM	Yes
500nM vs 100nM	Yes
100nM vs 6nM	Yes
100nM vs 30nM	No
30nM vs 6 nM	Yes

Figure 2.13. Titration of MTRIP probe concentration delivered to infected cells. MTRIPs (red) were delivered to RSV infected cells and the virus was isolated and immunostained for viral proteins N (green) and F (blue) at several concentrations: 6 nM, 30 nM, 100 nM, and 500 nM (**a**). Box-and-whisker plot of the number of MTRIP blobs that colocalize with N and F blobs as a percentage of the total number of MTRIP blobs, indicating the signal-to-noise ratio of the probe labeling (Kruskal-Wallis one way ANOVA on ranks with post-hoc Dunn's method for multiple comparisons) (**b**). The result of the multiple comparisons procedure is summarized in the table next to the plot (**c**). Single-plane, widefield deconvolved image shown. Scale bar 5 µm.

Labeled virus dynamics in cell culture

In addition to biochemical and plaque assays, we examined MTRIP-labeled virion replication in cell culture using fluorescence microscopy. After inoculating cells with MTRIP-labeled RSV, we delivered MTRIPs with a different fluorophore and fixed the cells at subsequent timepoints (**Fig. 2.14**). Fluorescence from the pre-labeled gRNA was observed even at 48 hr post infection, and remained colocalized with newly made gRNA and N protein. Infections with MTRIP-labeled virions produced filaments and inclusion bodies similar to infections with unlabeled virions.

Next, we compared MTRIP-labeled virion entry to a traditional GFP-based viral fusion assay, which uses citric acid to remove unbound virions from the surface of cells. A recombinant strain of RSV A2 expressing a GFP reporter gene in place of the RSV small hydrophobic (SH) protein gene, rgRSV-GFP,[2] was labeled with MTRIPs using the same protocol as the conventional A2 strain. This MTRIP-labeled rgRSV-GFP was used to inoculate cells for different time durations before unbound virions were inactivated with citric acid. Cells were imaged immediately after the citric acid wash, in order to count the number of labeled gRNAs inside cells, as well as twenty four hours later to count the number of GFP-positive infected cells (**Fig. 2.15**). The number of labeled gRNAs inside cells increased with time after inoculation, as did the number of GFP-positive cells. This finding suggests that the number of gRNAs, determined immediately after viral contact with the cells, could be used as a rapid indicator of virion fusion, as opposed to waiting up to twenty-four hours for GFP expression in the conventional assay.

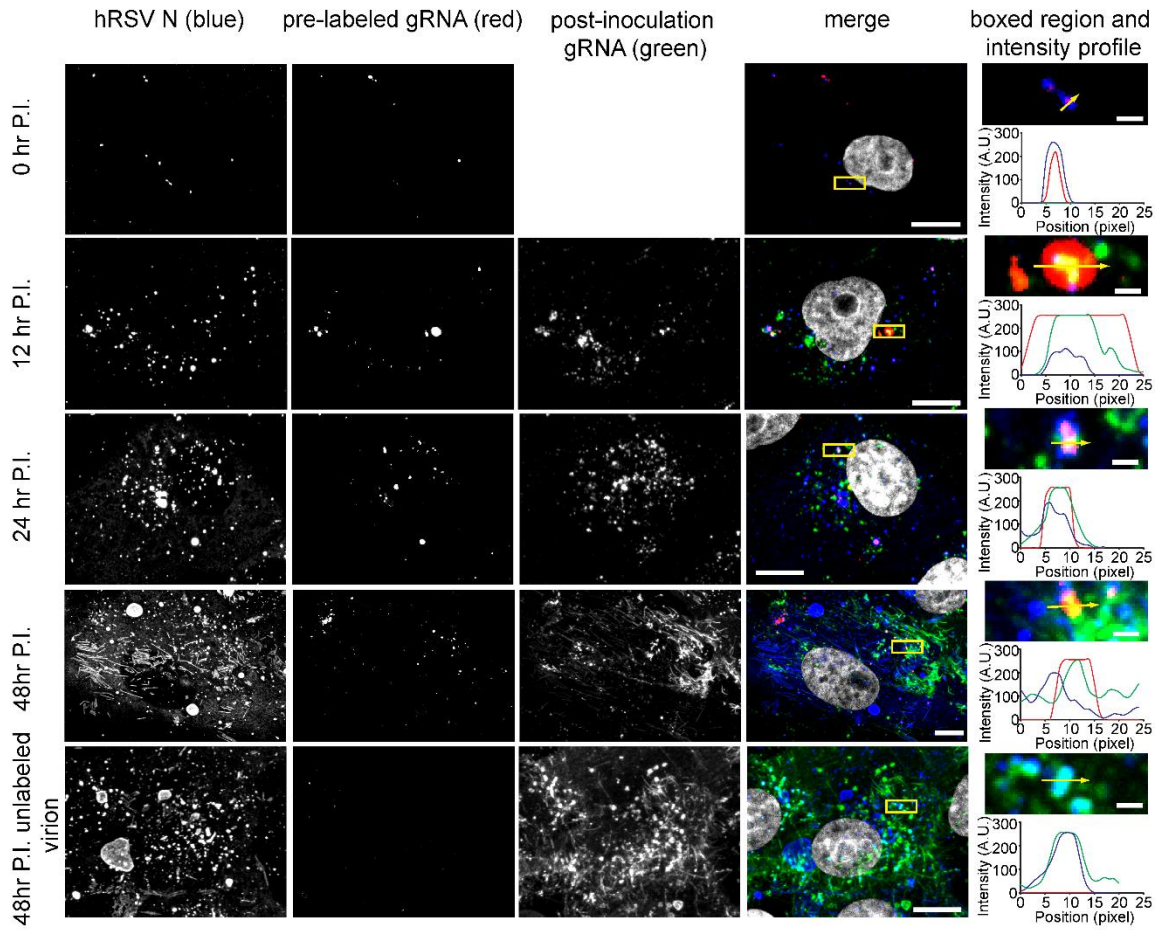

Figure 2.14 Confocal imaging of MTRIP-labeled RSV infections in cell culture. Vero cells were infected with MTRIP-labeled RSV at an M.O.I. of 1 and fixed at 0 hr, 12 hr, 24 hr, and 48 hr P.I. (rows). Columns show (from left to right): RSV N (blue), pre-labeled gRNA (red), post-inoculation gRNA (green), merged image, and magnification of boxed regions and fluorescence intensity profile plots along arrow in magnified image. Extended-focus, laser-scanning confocal images shown. Scale bars 10 µm and 1 µm for merged image and magnified boxed regions, respectively.

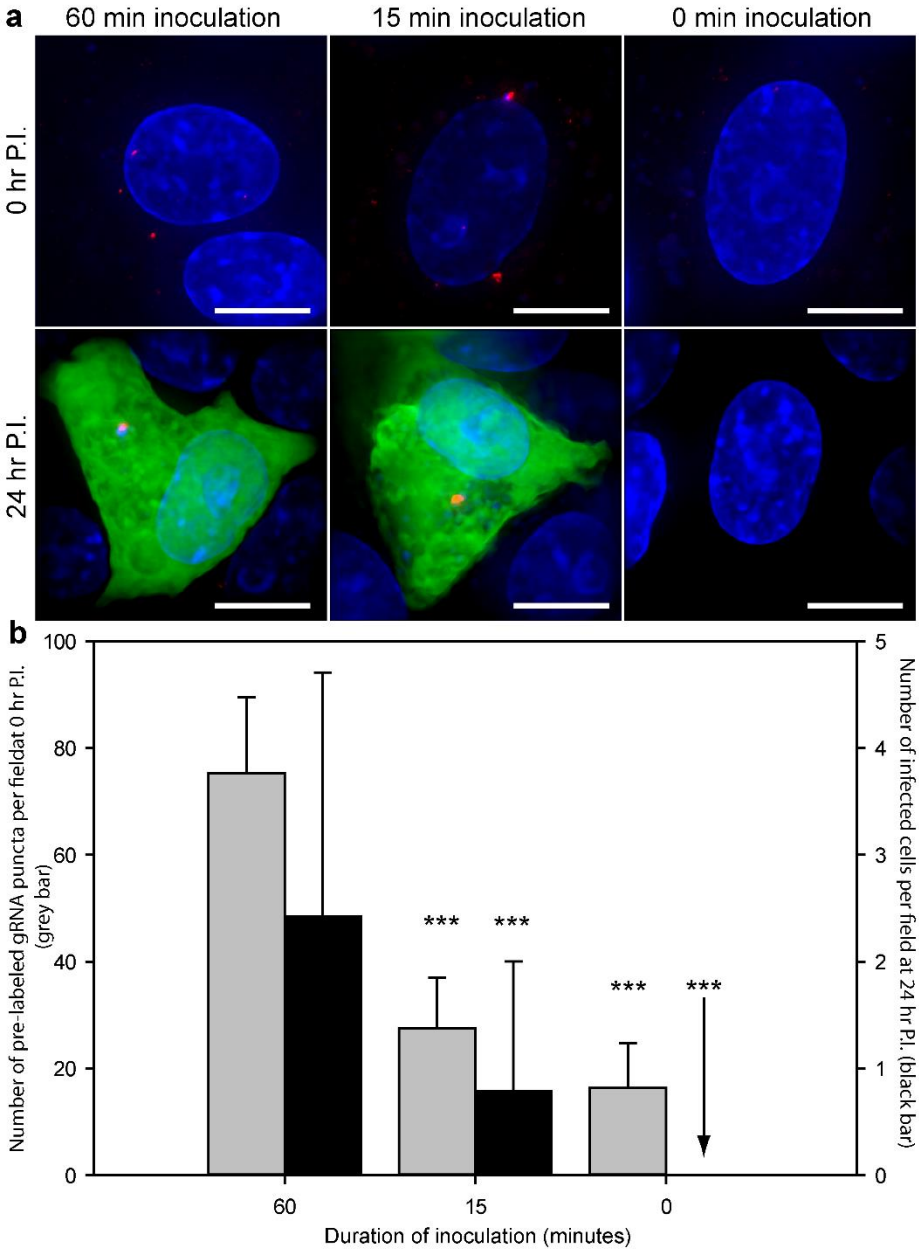

Figure 2.15 GFP-based fusion assay with MTRIP-labeled virions. MTRIP-labeled rgRSV-GFP virions were used to infect Vero cells at a M.O.I. of 1. Cells were inoculated for 0 min, 15 min, or 60 min (columns) and were imaged post-citric acid wash at 0 hr and 24 hr (rows) (**a**). Bar graph showing number of gRNA puncta per field of view (grey) at 0 hr P.I. and number of GFP-positive cells per field of view (black) at 24 hr P.I. (**b**). Extended focus, widefield deconvolved image shown. Scale bar 10 μm. Error bars s.d.

In live cells, MTRIP labeling of virions was used to assist in the visualization of the dynamic nature of a filamentous virion infecting a single cell. MTRIP-labeled virions were adsorbed to a cell monolayer at 4 °C and then imaged at 37 °C over the course of 40 min (**Fig. 2.16A**). The resulting videos showed a dynamic process, including periods of motion, rest, and changes in morphology of the filament. In an attempt to quantify whether this motion was the result of active or passive transport, we examined the absolute displacement, relative to the start coordinates, as well as the velocity and radius of gyration of a point on the filament (**Fig. 2.16B**).[18-20] We segmented the tracks over a rolling window of 4 minutes. This analysis showed that after an initial temperature-dependent transient motion (which we defined as the first five minutes of recording), filaments displayed small peaks in velocity accompanied by periods of little motion, leading to small changes in the absolute displacement. However, when the radius of gyration extent parameter was considered, these peaks were smaller and similar to the baseline values. Results from Monte Carlo simulations indicated that a threshold of R_G^2 = 0.3 μm^2 was sufficient to discriminate between periods of active and diffusive motion for a model virion (**Fig 2.17**). On this basis, trajectory segments were classified as either passive or active, as opposed to using the velocity directly. Using this threshold, we generated histograms of diffusion coefficients (for passive states) or velocities (for active states), as well as the time duration of active states for 15 virion tracks (**Fig. 2.16C**). For passive states, a log-normal fit obtained a median diffusion coefficient of 8.8 x 10^{-4} $\mu m^2 s^{-1}$. For active states, a Gaussian fit obtained a mean velocity of 6.1 x 10^{-3} $\mu m s^{-1}$. For the temporal duration of active states, the data was fitted to an exponential decay with median time 6.3 x 10^{-2} s. These measurements indicated that the motion exhibited by a

virion undergoing fusion was largely diffusive, with short, nonlinear durations of active transport interspersed during the course of observation.

We also confirmed that the motion and shape changes of the filaments were most likely due to fusion and not endocytosis by immunostaining for markers of early (EEA1) or late (CD63) endosomes and lysosomes (LAMP1). Labeled gRNA did not colocalize with any of these markers (**Fig. 2.18A**). We also recorded live-cell videos of filamentous virion dynamics in cells transduced with a baculovirus adapted to mammalian cell culture expressing Rab5-GFP, showing that Rab5 did not accumulate around a filament as it underwent fusion (**Fig. 2.18B**). Taken together, these results indicate that the changes in morphology and motion of a filament during fusion to cells were not due to endocytosis, but rather due to the viral fusion process with cell membrane.

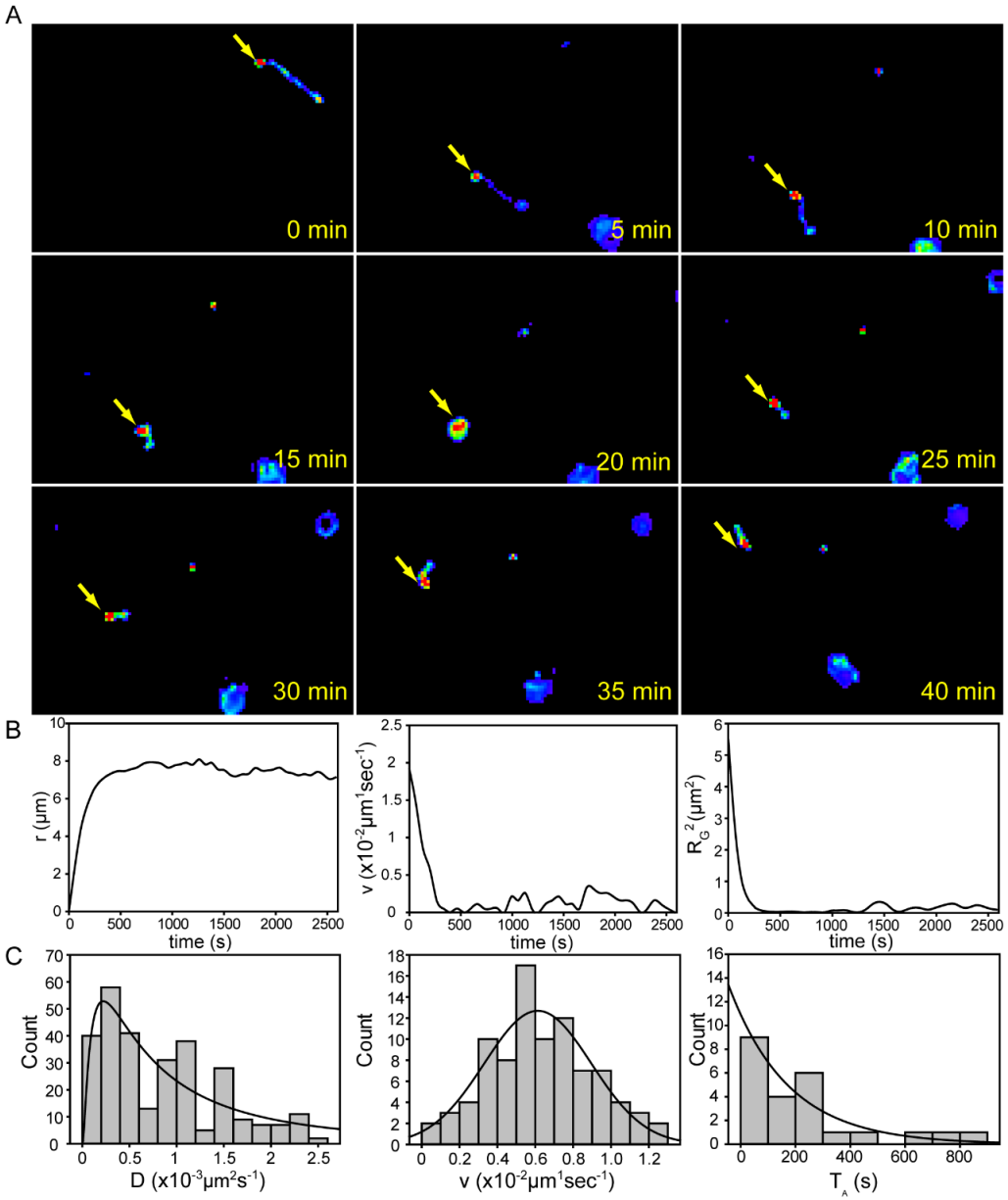

Figure 2.16 Single virion imaging reveals dynamic, largely-diffusive behavior for MTRIP-labeled filamentous virions infecting cells. Cells were inoculated with MTRIP-labeled virions at 4 °C before live cell imaging at 37 °C. (A) Frames from a typical live cell video, acquired at 1 frame/min over the course of 40 min. Arrow indicates the end of the filamentous virion that was monitored *via* single particle tracking. (B) Absolute displacement (from the position at t=0 min), instantaneous velocity, and square of the radius of gyration over time for the virion shown in Figure 5A. (C) Histograms of the diffusion coefficient during passive states (left), instantaneous velocity for active states (center), and temporal duration of active states (right) for 15 individual filamentous virions over two different experiments. Black line indicates log-normal fit, Gaussian fit, and exponential decay fit, respectively. Single-plane, widefield deconvolved images shown.

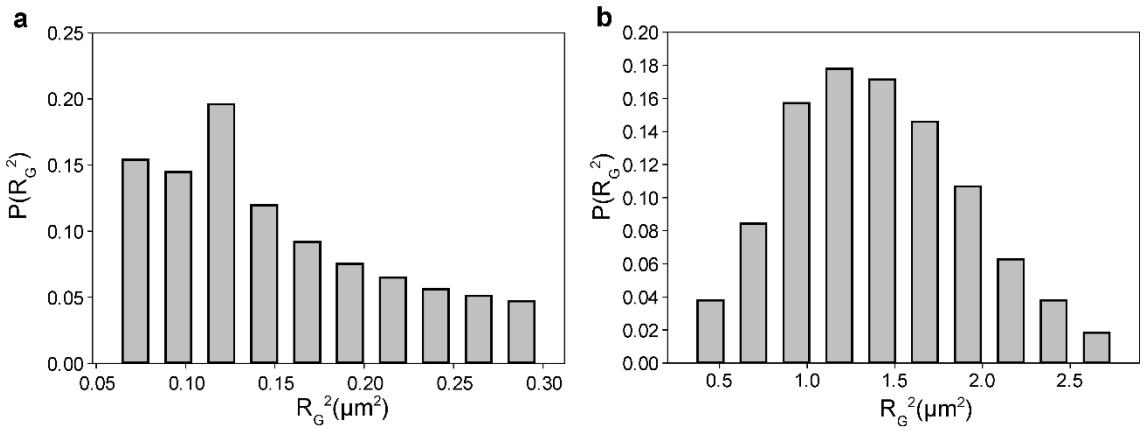

Figure 2.17. Monte Carlo simulations of active and passive transport. Histograms of radius of gyration squared for 10,000 track segments for a virion diffusing (diffusion coefficient of 1 x 10-4 $\mu m^2 s^{-1}$) generated from Monte Carlo simulations (a). Histograms of radius of gyration squared for 10,000 track segments for a particle undergoing diffusion and active transport (velocity of 1μm/min) (b). Radius of gyration squared threshold was set to 0.3 due to a less than 1% overlap at this point for the above distributions.

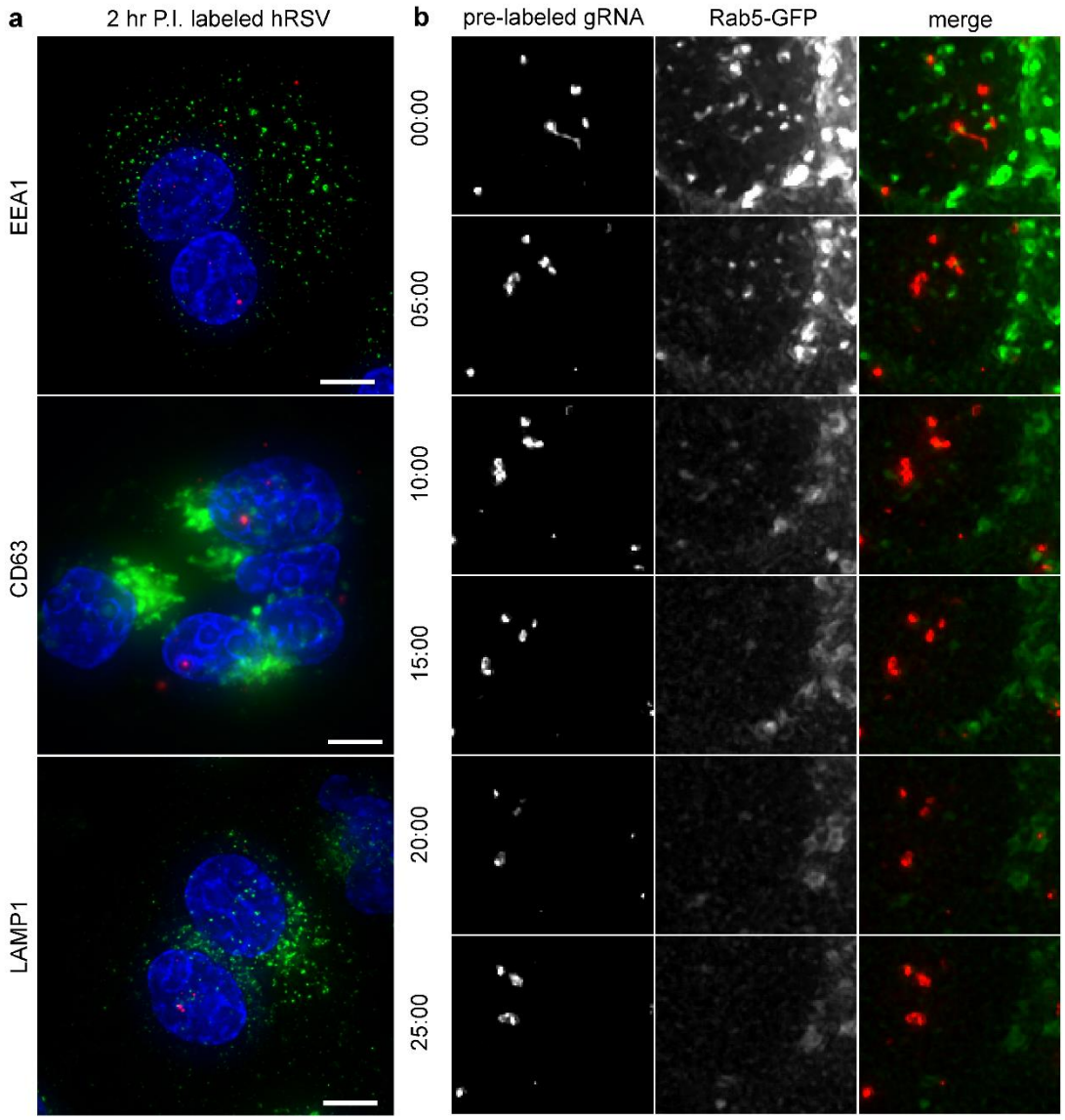

Figure 2.18 Compartmentalization of MTRIP-labeled virions. MTRIP-labeled RSV virions (red) were used to infect Vero cells and were fixed and immunostained at 2 hr P.I. for EEA1, CD63, and LAMP1 (green) (**a**). Frames from a live cell video taken at 0.033Hz (rows are every 5 min) showing an MTRIP-labeled filamentous virion on top of a cell that has been transduced with a Rab5-GFP baculovirus (**b**). Single-plane, widefield deconvolved image shown. Scale bar 10 µm.

Finally, we used MTRIP-labeled virions to track the same set of live cells as they progressed through an RSV infection. Using cells plated on a fibronectin-patterned 35 mm coverslip-bottomed dish, we watched HEp-2 cells inoculated with RSV for eight hours, delivering MTRIP probes, labeled with a spectrally distinct fluorophore than those labeling the virion, every four hours to monitor new gRNA production (**Fig. 2.19A**). The combination of cell patterning and MTRIP-labeling allowed the same cell to be relocated and imaged over multiple timepoints. By delivering MTRIPs with a spectrally distinct fluorophore at varying timepoints, we were able to quantify changes in the volume, intensity, and number of nascent gRNA puncta on a per-cell basis (**Fig. 2.19B**, **C**, **D**, respectively). It is clear that while the number of gRNA puncta did not change significantly, the sizes of the puncta increased dramatically, accompanied by a small, but significant increase in the normalized intensity. This finding suggested that once RSV gRNA entered the cell, it was confined to certain sites of replication and did not diffuse readily throughout the cytoplasm.

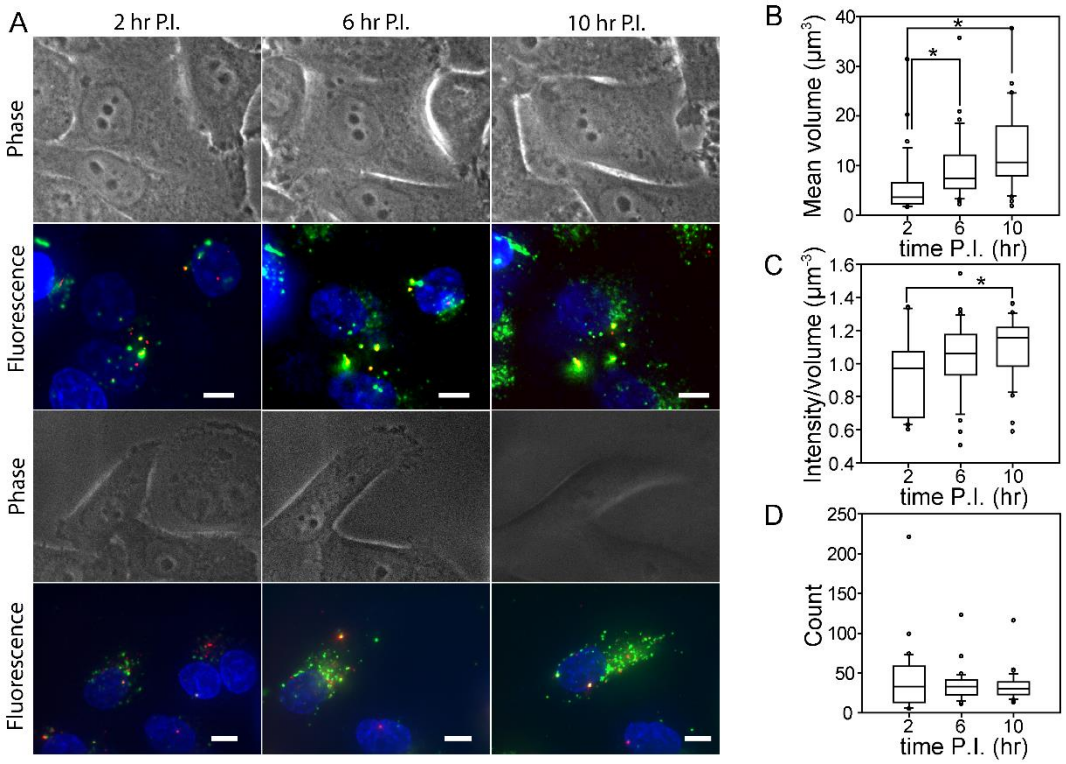

Figure 2.19 MTRIP-labeled RSV virions can be used to follow the same cell over the course of an infection. HEp-2 cells were plated onto a patterned fibronectin substrate and infected with MTRIP-labeled RSV. (**A**) Phase and fluorescence images for two different cells over an eight hour period with pre-labeled gRNA (red), newly produced gRNA (green), and cell nuclei (blue). (**B**) Mean fluorescence volume per puncta of the newly produced gRNA over the three timepoints. (**C**) Fluorescence intensity per volume of the newly produced gRNA over the three timepoints. (**D**) Number of newly produced gRNA puncta per cell over the three timepoints. One-way repeated measures ANOVA with Tukey test multiple comparison procedure, * indicates $P<0.05$.

Conclusion

Our approach provides a method to analyze the distribution of RNA and multiple viral proteins within virions simultaneously, using both conventional and localization microscopy. We demonstrated the isolated filamentous virions contain the viral M2-1, although whether or not M2-1 is attached to M[12], P[11,21], or another viral component within the isolate filament cannot resolved by fluorescence microscopy alone. Also, given the lower M2-1 staining signal relative to M, it is possible that M is in much higher copy number than M2-1; however, this might simply be due to different antibody affinity/accessibility.

We also demonstrated that MDA5 is localized to the isolated filaments. This is possibly due to an interaction with the N protein, which our group showed later on to be able to sequester MDA5 in cell transfected with on N and P plasmids.[22] This is the first repost of an RSV structural protein (which is highly expressed in infected cells) interacting with the RLR family of proteins.

While the imaging analysis of virus on glass has been attempted before using either membrane labeling or fluorescence in situ hybridization (FISH),[23] these methods detected the viral envelope (membrane labeling) or an internal RNA (FISH), not both at the same time. FISH requires fixation, membrane permeabilization, and the use of formamide, which can inhibit antibody binding for identification of proteins.

We also analyzed the dynamics of a filamentous virion undergoing fusion for the first time. The only other filamentous virion to have been labeled and imaged in a live cell is Ebola,[24,25] and that analysis was limited to the colocalization of endocytic markers with GFP-viral fusion proteins (as Ebola traffics through the macropinosome). The

passive motion of filaments during fusion merits further investigation. The velocity in the active states was not as high as those reported for virus surfing along filopodia,[26] and these states constituted a minority of the observed motion. Rather, the largely passive motion we observed might be due to virus attachment to cell surface lectin like molecules by the highly glycosylated RSV G surface glycoprotein followed by diffusion along the membrane and binding of the particles to a *bona fide* cell surface receptor, such as nucleolin,[27] which triggers fusion. An alternative hypothesis might be that the virus diffuses after first being recruited to a lipid raft.[1,28] To date, the study of paramyxovirus fusion proteins has been focused on the ultrastructure of the protein in different conformational states;[29] the ability to observe fusion dynamically could enhance these studies.

The ability to watch gRNA replication in a single cell allowed several important biological observations with implications for both RSV and for other viruses. For RSV, we observed that, in general, the overall number of granules increased slowly over time, but that the volume increased at a higher rate, suggesting that these granules were replication complexes. These complexes have not been defined previously, only assumed. The data also showed the inherent heterogeneity of cell features during RSV infections, which previous imaging studies have revealed, but had yet to be quantified. For viral infections, this approach has the means to ask and answer fundamental questions regarding the sources of heterogeneity of viral infections, because the initial conditions of each cellular infection can be defined, and the infection characterized within the same cells. This method clearly will assist in the quantification and development of mechanistic models of cell-to-cell variation during viral infections.

The MTRIP probe design has several distinct advantages over other virus labeling methods. Since each MTRIP is labeled with 8-12 fluorophores, fewer probes are required to produce a single molecule sensitive fluorescence intensity than other methods such as single fluorophore FISH,[30] increasing sensitivity. Organic fluorophores are also more resistant to photobleaching than fluorescent proteins. While quantum dots have also been used for virus labeling,[31] their size and toxic effects limits their ability to observe the viral gRNA over long periods of time. For high frame rate imaging of viral dynamics, the blinking of the fluorescence intensity of quantum dots[32] might introduce artifacts in single particle tracking and deconvolution algorithms. MTRIPs do not blink under normal buffer conditions and widefield illumination, avoiding this problem. By designing different biotinylated oligonucleotides to bind to different virion sequences, they can be easily adapted to target to different regions on the gRNA, allowing for the possibility of increasing fluorescence intensity in particle tracking experiments and for increased localization accuracy in super resolution microscopy. Lastly, the addition of gold nanoparticles to the neutravidin core of the MTRIP allowed for darkfield imaging *via* silver enhancement, making labeled RNA TEM imaging possible. Most importantly, the MTRIP labeling method does not affect the first cycle of virus replication, or the titer during amplification, or the virus morphology.

In summary, MTRIP-labeling of viral RNA has the potential to become a general methodology for the labeling and study of many different RNA viruses. Assuming unique target sequences can be found within a given virus's genome, MTRIP probes could be designed to bind to it, making our technique broadly applicable to most virus studies. The approach also could also be combined with conventional membrane labeling techniques

and fluorescent fusion protein technology to yield multi-colored virions suitable for live-cell observation of virion infection over the life of the infections.

Materials and methods

The MTRIP probe assembly method is as follows. Briefly, 2'-O-methyl RNA/DNA chimeric nucleic acid ligands (targeting the intergenic-gene start sequences of the RSV A2 genome) containing a 5'-biotin modification (Biosearch Technologies) were labeled with either Cy3B NHS ester (GE Healthcare) or DyLight 650 NHS esters (Pierce). Unbound dye was removed *via* centrifugation in a 3 kDa filter (Millipore) and stored at -20 °C until further use.

To assemble probes, labeled oligonucleotides were mixed with neutravidin (Pierce) in a 5:1 molar ratio and allowed to react at room temperature for 1 hr. Unbound oligonucleotides were removed by centrifugation in a 30 kDa filter (Millipore).

Cells were cultured in the following manner. HEp-2 human epithelial cells (American Tissue Culture Collection CCL-23) and Vero green monkey kidney cells (CCL-81) were maintained in DMEM (Lonza) supplemented with 10% fetal bovine serum (Hyclone) and 100 U mL-1 penicillin and 100 mg mL-1 streptomycin (Invitrogen). Cells were plated on No. 1.5 coverslips (Electron Microscopy Sciences) or 35 mm coverslip bottomed dishes (In Vitro Scientific) one day prior to infection or imaging.

For MTRIP probe delivery, cells were washed in Dulbecco's phosphate buffered saline (DPBS) without Ca^{2+} and Mg^{2+} (Lonza), and subsequently incubated with OptiMEM I (Invitrogen) containing 30 nM MTRIP probes and 0.2 U ml-1 activated streptolysin O (Sigma) for 10 min at 37 °C. Afterwards, the OptiMEM was replaced with complete growth media for 15 min at 37 °C before fixation, imaging, or harvesting virus.

All viruses were grown in the following manner. RSV strain A2 (American Tissue Culture Collection VR-1544) or rgRSV-GFP was propagated in low-passage HEp-

2 cells when the cells were >80% confluent. The medium was removed from cells, the cells were washed with DPBS (without Ca 2+ and Mg2+), and virus was added at an MOI 0.1 for 1 hr before adding fresh medium to the inoculum. Cell-associated virus was harvested by scraping when the cells displayed a high degree of C.P.E. (approximately 90%, or around 96 hr post infection), vortexed briefly, aliquoted, and stored at -80 °C. For MTRIP-labeled virus, MTRIP probes were delivered to cells according to the probe delivery methods section before the cells were scraped.

In order to quantify the titer of unlabeled and labeled RSV, aliquots of frozen virus were thawed and equal volumes of labeled and unlabeled virus (from virus propagation methods section) were serially diluted from 10^{-2} to 10^{-6} and used to inoculate 24-well plates of 100% confluent Vero cells in quadruplicate. Inoculant was allowed to incubate for 1 hr before cells were covered with 1 mL per well of 1.2% microcrystalline methylcellulose (Avicel, FMC Biopolymer) in growth media, similar to Matrosovich *et al.*[33].The cells were incubated with overlay for 6 days post infection, when visible, uniform plaques ~3 mm in diameter had formed. The cells were fixed with 4% paraformaldehyde, blocked with 5% BSA, and stained using a primary antibody and secondary HRP conjugated antibody (listed in antibodies methods section) for incubation times similar to the immunostaining protocol below. A peroxidase substrate was added after washing (TrueBlue, KPL) and allowed to develop for 10 min before washing again. Dilutions with countable numbers of plaques (between 5 and 50) had their plaques counted, averaged over the four replicate wells, and multiplied by the dilution factor to calculate the titer in pfu/ml. This assay was done for three aliquots per batch of virus grown, and the average titer of the three aliquots was used to normalize the number of

input virus between unlabeled and labeled virus for all subsequent experiments with that virus batch.

Viral mRNA load was assessed by qRT-PCR in the following manner. HEp-2 cells were plated in 6 well plates the day before infection at >80% confluence. Cells were infected with unlabeled or labeled virus at an M.O.I. of 0.1 for 6, 12, or 24 hr post infection. Total RNA was extracted using an RNeasy kit (Qiagen) following the manufacturer's protocol. After quantification, messenger RNA was isolated from total RNA using an Oligotex kit (Qiagen) following the manufacturer's protocol. cDNA synthesis was performed using 70.4ng of mRNA and a First Strand Reaction kit (SA Biosciences) according to the manufacturer's protocol. qRT-PCR was performed in triplicate using the Universal MasterMix (Applied Biosystems), Taqman probe/primer sets described in Thornburg *et al.* 2012[34] and a Step-One Plus real-time thermocycler (Applied Biosystems). Human GAPDH probe/primers (Applied Biosystems) were used as a loading control. Cycle threshold detection was performed using the Applied Biosystems software. Infections and extractions were repeated three times.

Western blotting for viral proteins was done as follows. HEp-2 cells were plated in 6 well plates the day before infection at >80% confluence. Cells were infected with unlabeled or labeled RSV at an M.O.I. of 0.1 for 12 or 24 hr post infection. Cells were lysed by adding RIPA buffer (Pierce) spiked with 50X Complete Protease Inhibitor (Roche), scraping, and clarifying by centrifugation. Protein concentration was quantified using a BCA assay (Pierce) following the manufacturer's protocol. Lysates were stored at -80 °C until use.

For SDS-PAGE gel, 12 µg of lysates were mixed with a 4X SDS loading buffer (LI-COR Biosciences), boiled for 10 min at 70 °C, chilled on ice, and loaded into wells of a 10% Bis-Tris pre-cast gel (Invitrogen) along with a molecular weight marker (LI-COR). Gel was run in an XCell Surelock Mini Cell system (Invitrogen) in 1X MOPS running buffer (Invitrogen) at 200V constant for 50 min. Protein was transferred to 0.45 µm pore nitrocellulose membranes (Invitrogen) using an XCell II Blot module (Invitrogen) running at 30V constant for 1 hr in 1X western transfer buffer (Invitrogen).

Blots were stained using a Snap i.d. blot holder (Millipore). First, non-specific binding was blocked using blocking solution (LI-COR). Vacuum was immediately turned on for 20 s to remove solution. Next, the primary antibody against the protein (along with a β-actin antibody) was added and allowed to incubate for 10 min. Vacuum was turned on a blots were washed three times with 1X PBS containing 0.1% Tween-20. Finally, the secondary antibodies was added and allowed to incubate for 10 min. Blots were washed three times with PBS containing Tween-20 and then imaged using an Odyssey IR imager (LI-COR). Exposure times and gain settings were kept fixed for each protein, and only linear contrast enhancement was performed for the final representative image. Each isolation was performed three times and all blots were quantified by densitometry using the Image Studio software package (LI-COR). Total signals in the 700 nm channel were recorded using a rectangular ROI that covered ~1/3 the lane width and the entire lane length.[35] Background was subtracted using a median filter to find the actual protein signal. This procedure was repeated for β-actin in the 800 nm channel, and the protein signal was divided by the actin signal for each lane (replicate extraction) to yield the relative density.

ELISAs for total viral protein were performed as follows. A total RSV protein ELISA kit (Bioo Scientific) was used according to the manufacturer's protocol using 100 µg of protein per well. Each sample was assayed in duplicate, and three samples (from three different infections and extractions) were done for each condition (labeled or unlabeled).

Thin section transmission electron microscopy was done according to the following method. Vero cells were plated in a 6-well plate at >80% confluence and were infected with unlabeled or labeled virus (M.O.I. 0.1). At 24 hr post infection, probes were delivered to one set of cells infected with unlabeled virus (for "immediately post probe delivery" condition) and all cells were fixed overnight at 4 °C with 2.5% glutaraldehyde in 0.1 M cacodylate buffer (pH 7.4, Electron Microscopy Sciences). Cells were then washed and post- fixed in 1% osmium tetroxide with 1.5% potassium ferrocyanide in the same buffer for one hour. The samples were subsequently rinsed with 2 or 3 exchanges of de-ionized water, dehydrated through an ethanol series ending with three exchanges of 100% absolute ethanol, and embedded in Eponate 12 resin (Ted Pella) by placing resin infiltrated cells in a 60 °C oven for 2 days.

Upon resin polymerization, hardened resin blocks with monolayer cells on the bottom surface were removed from the culture plate, sawed into smaller pieces, and thin-sectioned perpendicular to the cell surface at 70 nm. Sections were then picked up with 200 mesh Formvar-coated copper grids, stained with 5% aqueous uranyl acetate and 2% lead citrate, and viewed on a JEOL JEM_1400 transmission electron microscope (JEOL) equipped with a Gatan US1000, 2k x 2k CCD camera (Gatan, Inc.).

In all imaging experiments (not virus propagation), unlabeled or labeled virus used for infecting cells was first centrifuged through 5 μm and 0.45 μm filters (Millipore) at 5,000 x g and 4 °C for 4 min and 1 min, respectively, to isolate single filaments. This filtration is important for imaging experiments, because it removes the dead cell debris from the cell-associated RSV. The cell debris complicates the imaging of single filamentous virions on glass or in cells. However, this centrifugal filtration leads to a loss of infectivity, regardless of whether or not the virus is labeled, because some virus sticks to the filter membrane. Hence, to compensate for this loss in virus, the initial volume of virus filtered was calculated using the titer for that batch, desired M.O.I. for that experimental design, and a scalar factor characteristic of the filters. For example, for an experiment with a desired M.O.I of 1 involving 100,000 cells per well, a virus batch with a titer of 1 x 10^6 pfu/mL, and a filter correction factor of 2 (about 50% of viruses is lost in the filter), the initial volume of virus needed (before filtration) would be

$$100{,}000\ \frac{cells}{well} \times 0.1 \frac{virions}{cell} = 10{,}000\ virions\ post\ filtration$$
$$10{,}000\ virions \times 2 = 20{,}000\ virions\ pre\ filtration$$
$$20{,}000\ virions \times (1 \times 10^6 \frac{pfu}{ml})^{-1} = 0.020ml\ virus\ needed\ pre\ filtration$$

The stated M.O.I. for both the labeled and unlabeled viruses (seen in most figure captions) accurately reflects this adjustment in the volume.

For synchronized inoculation of virus, cells were chilled on ice at 4 °C to prevent endocytosis and synchronize virion fusion. Cells were then washed with chilled DPBS (without Ca^{2+} and Mg^{2+}) and virus in chilled growth medium was added to the cells and allowed to adsorb for 30 min on ice at 4 °C. Afterwards, cells were moved to an incubator at 37 °C and the virus was allowed to fuse for 2 hr before being removed and

replaced with complete growth media, except for the filament dynamics experiments, which were imaged immediately after adsorption of virus and after 5 min in the live cell environment to bring them up to 37 °C.

For immunostaining, cells or virus on coverslips were fixed in 4% paraformaldehyde (Electron Microscopy Sciences) in PBS for 10 min at room temperature before permeabilization with 0.2% Triton X-100 (Sigma) for 5 min at room temperature. This step was followed by blocking with 5% bovine serum albumin for 30 min at 37 °C, washing with PBS, primary antibody incubation for 30 min at 37 °C, washing with PBS, secondary antibody incubation 30 min at 37 °C, and a final washing with PBS. Multiple antibody labeling was done simultaneously after checking for cross-reactivity. Cells then were stained with DAPI, and all samples were mounted with Prolong Gold (Invitrogen).

For virus on glass, before fixation, virus was centrifuged through the filters used for infecting cells. This size fraction then was spun down onto poly-L-lysine (Sigma) coated coverslips *via* centrifugation at 3,007 x g and 4 °C for 30 min. Virus then was fixed and immunostained using the above method.

All antibodies used are listed here. For western blot, the primary antibodies used were a mouse monoclonal anti-RSV G (Abcam) and a mouse monoclonal anti-RSV P (clone 3_5, a kind gift of Earling Norrby and Ewa Bjorling). Secondary antibodies used were donkey anti-mouse DyLight 680 (Pierce) and donkey-anti rabbit IRDye 800 (LI-COR).

For plaque assay, the primary antibody used was a goat polyclonal anti-RSV (Abcam). The secondary antibody was a donkey anti-goat HRP (Jackson Immunoresearch).

For imaging, primary antibodies used were: mouse anti-RSV N (Abcam), human anti-RSV F (MedImmune), mouse anti-EEA1 (BD Biosciences), mouse anti-CD63, and mouse anti-LAMP1 (both from Developmental Studies Hybridoma Bank). Secondary antibodies used were: donkey anti-mouse Alexa Fluor 488 (Invitrogen), donkey anti-human DyLight 650, and donkey anti-human Alexa Fluor 647 (Jackson Immunoresearch).

Fixed and live cell images were acquired in the following manner. Images for fixed cell pulse-chase experiments were taken on a LSM 710 laser scanning confocal microscope (Zeiss) with a 63X, NA 1.4 plan-apochromat objective. RSV N and pre-labeled gRNA were taken on separate tracks to minimize bleed through; DAPI and post-inoculation gRNA were taken on the same track. Lasers used for DAPI, RSV N, pre-labeled gRNA (Cy3B), and post inoculation gRNA (DyLight 650) were 405 nm, 488 nm, 555 nm, and 635 nm, respectively. Z stacks were taken in increments of 0.4 μm, pinhole set to 1 Airy disk.

All other images were taken on an Axiovert 200M inverted microscope (Zeiss) with a 63X, NA 1.4 plan-apochromat objective and ORCA-ER AG camera (Hamamatsu). The 89000 Sedat Quad-ET filter set (Chroma) was used. Z stacks were taken in increments of 0.2 μm. Images acquired using Volocity software (Perkin Elmer).

Live cell experiments were taken using cells in 35 mm coverslip bottom dishes with Leibovitz's CO_2 independent L-15 medium (Invitrogen) supplemented with 10%

FBS medium. Dishes were kept warm during imaging using a Chamlide TC-L live cell environment (Live Cell Instrument). Images were taken using a C9100-02 EMCCD camera (Hamamatsu).

Images were processed in the following manner. All widefield images were deconvolved using Volocity. All object finding and counting conducted using Volocity and exported to Excel (Microsoft) or Sigma Plot (Systat) for graphing and statistical analysis. Exceptions include probe titration, for which the blob colocalization was computed by exporting TIFF images for each channel from Volocity and using the ImageJ plugin described in Fletcher *et al*. [17]

Live cell videos taken with the EMCCD camera were denoised using the ND-Safir binary for Windows described by Boulanger *et al*. [36] using the default settings. Videos were exported from Volocity as TIFF files, assembled into stacks by timepoint using custom programs in MATLAB (MathWorks), and the ND-Safir binary was called repeatedly to process each timepoint. Videos were reassembled in Volocity for deconvolution.

Single particle tracking of filaments was performed manually in Volocity. Manual track coordinates were exported *via* CSV file into MATLAB. Rolling window temporal analysis and Monte Carlo simulations were carried out using custom programs. Results were graphed and fitted using Sigma Plot.

Linear contrast enhancements were performed on images and videos for clarity. All calculations were performed on unenhanced, deconvolved data.

Darkfield imaging was performed as follows. Optical and hyperspectral images along with hyperspectral data were captured utilizing a research grade optical microscope

equipped with the CytoViva advanced darkfield illumination system dual mode fluorescence module and integrated hyperspectral imaging system (CytoViva, Inc., Auburn, AL). This integrated system builds hyperspectral image files by a "push broom" method, enabling the creation of a high signal to noise spectral image file. Subsequent image analysis delineates the reflectance spectral response of the sample elements in each nanoscale pixel of the image file.

The RSV fusion assay was conducted in the following manner. Inoculation of cells with MTRIP-labeled rgRSV-GFP occurred as described above. Virions were allowed to fuse for a designated time at 37 °C before being washed with a 40mM sodium citrate solution containing 10 mM potassium chloride and 135 mM sodium chloride (Sigma) adjusted to pH 3.0. Cells were imaged immediately afterward in L-15 growth media and then allowed to sit in complete growth media for 24 hr before being imaged again.

Cells were transduced with a Rab5-GFP baculovirus adapted for mammalian cell culture, following the manufacturer's protocol (Invitrogen).

Live cell virus replication experiments were done as follows. Micropatterned substrates to control cell spread area and clustering were prepared by microcontact printing of fibronectin, as has been previously described.[37] Briefly, stamps made from PDMS (Sylgard 184 elastomer kit, Dow Corning) consisting of 100 x 100 μm squares were plasma cleaned and inked with 50 μg/mL human plasma-purified fibronectin. Stamps were dried under nitrogen gas, and protein was transferred onto acid-washed No. 1.5 coverglass or 35 mm coverslip-bottomed dishes. The substrates were then blocked with 10% heat-denatured bovine serum albumin to prevent non-specific cell attachment.

Cells were plated the day before infection, inoculated as described above, and had 30 nM DyLight 650 MTRIP probes delivered to them at 2 hr post infection and every four hours thereafter. Cells were left in the Chamlide live cell environment in L-15 medium supplemented with FBS to facilitate relocation of the same cells.

References

1.San-Juan-Vergara, H. *et al.* Cholesterol-rich microdomains as docking platforms for respiratory syncytial virus in normal human bronchial epithelial cells. *J. Virol.* **86,** 1832-43 (2011).

2.Hallak, L. K., Collins, P. L., Knudson, W. & Peeples, M. E. Iduronic acid-containing glycosaminoglycans on target cells are required for efficient respiratory syncytial virus infection. *Virology* **271,** 264-75 (2000).

3.Brandenburg, B. *et al.* Imaging poliovirus entry in live cells. *PLoS Biol.* **5,** e183 (2007).

4.Jouvenet, N., Bieniasz, P. D. & Simon, S. M. Imaging the biogenesis of individual HIV-1 virions in live cells. *Nature* **454,** 236-40 (2008).

5.Jouvenet, N., Simon, S. M. & Bieniasz, P. D. Imaging the interaction of HIV-1 genomes and Gag during assembly of individual viral particles. *Proc. Natl. Acad. Sci. U.S.A.* **106,** 19114-9 (2009).

6.Tawar, R. G. *et al.* Crystal structure of a nucleocapsid-like nucleoprotein-RNA complex of respiratory syncytial virus. *Science* **326,** 1279-83 (2009).

7.Bakker, S. E. *et al.* The respiratory syncytial virus nucleoprotein-RNA complex forms a left-handed helical nucleocapsid. *J. Gen. Virol.* **94,** 1734-8 (2013).

8.Santangelo, P. J. *et al.* Single molecule-sensitive probes for imaging RNA in live cells. *Nat. Methods* **6,** 347-9 (2009).

9.Roberts, S. R., Compans, R. W. & Wertz, G. W. Respiratory syncytial virus matures at the apical surfaces of polarized epithelial cells. *J. Virol.* **69,** 2667-73 (1995).

10.Zhou, H., Cheng, X. & Jin, H. Identification of amino acids that are critical to the processivity function of respiratory syncytial virus M2-1 protein. *J. Virol.* **77,** 5046-53 (2003).

11.Tran, T. *et al.* The respiratory syncytial virus M2-1 protein forms tetramers and interacts with RNA and P in a competitive manner. *J. Virol.* **83,** 6363-74 (2009).

12.Li, D. *et al.* Association of respiratory syncytial virus M protein with viral nucleocapsids is mediated by the M2-1 protein. *J. Virol.* **82,** 8863-70 (2008).

13.Mogensen, T. H. Pathogen recognition and inflammatory signaling in innate immune defenses. *Clinical Microbiology Reviews* **22,** (2009).

14.Barik, S. Respiratory syncytial virus mechanisms to interfere with type 1 interferons. *Current Topics in Microbiology and Immunology* **372,** 173-91 (2013).

15.Takimoto, T. *et al.* Recombinant Sendai virus expressing the G glycoprotein of respiratory syncytial virus (RSV) elicits immune protection against RSV. *J. Virol.* **78,** 6043-7 (2004).

16.Chowdhury, M. H. *et al.* Computational study of fluorescence scattering by silver nanoparticles. *J Opt Soc Am B* **24,** 2259-2267 (2007).

17.Fletcher, P. A., Scriven, D. R. L., Schulson, M. N. & Moore, E. D. W. Multi-image colocalization and its statistical significance. *Biophysical journal* **99,** 1996-2005 (2010).

18.Lifland, A. W., Zurla, C., Yu, J. & Santangelo, P. J. Dynamics of native β-actin mRNA transport in the cytoplasm. *Traffic* **12,** 1000-11 (2011).

19.Saxton, M. J. Single-particle tracking: models of directed transport. *Biophysical journal* **67,** 2110 (1994).

20.Saxton, M. J. Single-particle tracking: the distribution of diffusion coefficients. *Biophysical journal* **72,** 1744 (1997).

21.Blondot, M. *et al.* Structure and functional analysis of the RNA- and viral phosphoprotein-binding domain of respiratory syncytial virus M2-1 protein. *PLoS Pathog.* **8,** e1002734 (2012).

22.Lifland, A. W. *et al.* Human respiratory syncytial virus nucleoprotein and inclusion bodies antagonize the innate immune response mediated by MDA5 and MAVS. *J. Virol.* **86,** 8245-58 (2012).

23.Chou, Y. *et al.* One influenza virus particle packages eight unique viral RNAs as shown by FISH analysis. *Proc. Natl. Acad. Sci. U.S.A.* **109,** 9101-6 (2012).

24.Nanbo, A. *et al.* Ebolavirus is internalized into host cells via macropinocytosis in a viral glycoprotein-dependent manner. *PLoS Pathog.* **6,** e1001121 (2010).

25.Saeed, M. F., Kolokoltsov, A. A., Albrecht, T. & Davey, R. A. Cellular entry of ebola virus involves uptake by a macropinocytosis-like mechanism and subsequent trafficking through early and late endosomes. *PLoS Pathog.* **6,** e1001110 (2010).

26.Lehmann, M. J., Sherer, N. M., Marks, C. B., Pypaert, M. & Mothes, W. Actin- and myosin-driven movement of viruses along filopodia precedes their entry into cells. *J. Cell Biol.* **170,** 317-25 (2005).

27.Tayyari, F. *et al.* Identification of nucleolin as a cellular receptor for human respiratory syncytial virus. *Nat. Med.* **17,** 1132-5 (2011).

28.Brown, G. *et al.* Analysis of the interaction between respiratory syncytial virus and lipid-rafts in Hep2 cells during infection. *Virology* **327,** 175-85 (2004).

29.Steinhauer, D. A. & Plemper, R. K. Structure of the primed paramyxovirus fusion protein. *Proc. Natl. Acad. Sci. U.S.A.* **109,** 16404-5 (2012).

30.Raj, A., van den Bogaard, P., Rifkin, S. A., van Oudenaarden, A. & Tyagi, S. Imaging individual mRNA molecules using multiple singly labeled probes. *Nat. Methods* **5,** 877-9 (2008).

31.Zhang, Y. *et al.* Encapsulating quantum dots into enveloped virus in living cells for tracking virus infection. *ACS nano* **7,** 3896-904 (2013).

32.Galland, C. *et al.* Two types of luminescence blinking revealed by spectroelectrochemistry of single quantum dots. *Nature* **479,** 203-7 (2011).

33.Matrosovich, M., Matrosovich, T., Garten, W. & Klenk, H. New low-viscosity overlay medium for viral plaque assays. *Virology Journal* **3,** 63 (2006).

34.Thornburg, N. J., Hayward, S. L. & Crowe, J. E. Respiratory Syncytial Virus Regulates Human MicroRNAs by Using Mechanisms Involving Beta Interferon and NF- B. *mBio* **3,** e00220-12 (2012).

35.Gassmann, M., Grenacher, B., Rohde, B. & Vogel, J. Quantifying Western blots: pitfalls of densitometry. *Electrophoresis* **30,** 1845-55-1855 (2009).

36.Boulanger, J. *et al.* Patch-based nonlocal functional for denoising fluorescence microscopy image sequences. *IEEE Trans Med Imaging* **29,** 442-54 (2009).

37.Shen, K., Qi, J. & Kam, L. C. Microcontact printing of proteins for cell biology. *J Vis Exp* (2008). doi:10.3791/1065

CHAPTER 3

IMAGING RSV USING DSTORM

The work presented here is excerpted from the following publications: Alonas, E., Lifland, A.W., Gudheti, M., Vanover, D., Jung, J., Zurla, C., Kirschman, J., Fiore, V.F., Douglas, A., Barker, T.H., Yi, H., Wright, E.R., Crowe Jr., J.E., & Santangelo, P.J. Combining single RNA sensitive probes with subdiffraction-limited and live-cell imaging enables the characterization of virus dynamics in cells. *ACS Nano* **8**, 302-15 (2014) and Kiss, G., Holl, J.M., Williams, G.M., Alonas, E., Vanover, D., Lifland, A.W., Gudheti, M., Guerrero-Ferreira, R.C., Nair, V., Yi, H., Graham, B.S., Santangelo, P.J., & Wright, E.R. Structural analysis of respiratory syncytial virus reveals the position of M2-1 between the matrix protein and the ribonucleoprotein complex. *J. Virol.* **88**, 7602-17 (2014).

Background

In an effort to gain increased spatial resolution images of the isolated filamentous and spherical-like virions, we attempted direct stochastic localization microscopy (dSTORM). This technique relies on conventional fluorophores[1] as opposed to photoswitchable fluorophore pairs[2], used in conventional STORM, or photoswitchable fluorescent proteins[3], used in FPALM. The switching properties of several popular organic fluorophores, such as AlexaFluor 647, had already been characterized[1]. Using the biplane approach of the Vutara dSTORM system, we were able to capture the entire virus with subdiffraction-limited resolution in the x and y (~20-30 nm resolution), and z (~50 nm resolution). The biplane setup allows the user to collect 3D information quickly[4,5], as opposed to strictly illuminating on the TIRF plane.

STORM and dSTORM had already been used to resolve fine structures in cells, such as the microtubules, mitochondria [6], and nuclear pore complex.[7]. However, in studying viruses, localization microscopy had only been applied to HIV[8]. Since then, it has also been used to image the tegument and capsid proteins of herpes simplex virus[9]. Our efforts at dSTORM represent the first attempt at imaging a paramyxovirus and demonstrate that MTRIPs are compatible with dSTORM, which had not been previously shown.

Imaging, F, N, and genomic RNA using dSTORM

To investigate how the distribution of gRNA compared to the distribution of viral proteins within filamentous virions, we used localization microscopy to image the labeled virions on coverslips. We found that the gRNA and N protein were distributed along the length of the filament, unevenly, for the first two example filaments shown (**Fig. 3.1A**). However, the N protein did not colocalize exactly with the gRNA, suggesting that the N protein might not be bound to gRNA everywhere inside the virion. Upon examination of 100 nm cross sections through the filaments (boxed regions), we found that gRNA and N protein, in regions where they were both present, overlapped each other tightly. This finding was not the case for the F protein, which was distributed evenly along the length of the filaments and appeared in the cross section to surround, rather than overlap, the gRNA (**Fig. 3.1B**). Note, the F protein was absent on the side of the filaments that was in contact with the glass. This finding likely was due to the antibody failing to access that side of the virion during immunostaining. These observations were quantified using the full width half maximum (FWHM) of the point count for each channel for the cross sections shown (**Fig. 3.1C**). While the axial FWHM did not differ significantly between measurements for the F and N proteins, the lateral FWHM for N was less than that of F,

and closer to the values for gRNA. These data clearly show that N and the MTRIP probes were in the interior of the virion, and the F protein was located further from the center of the virion.

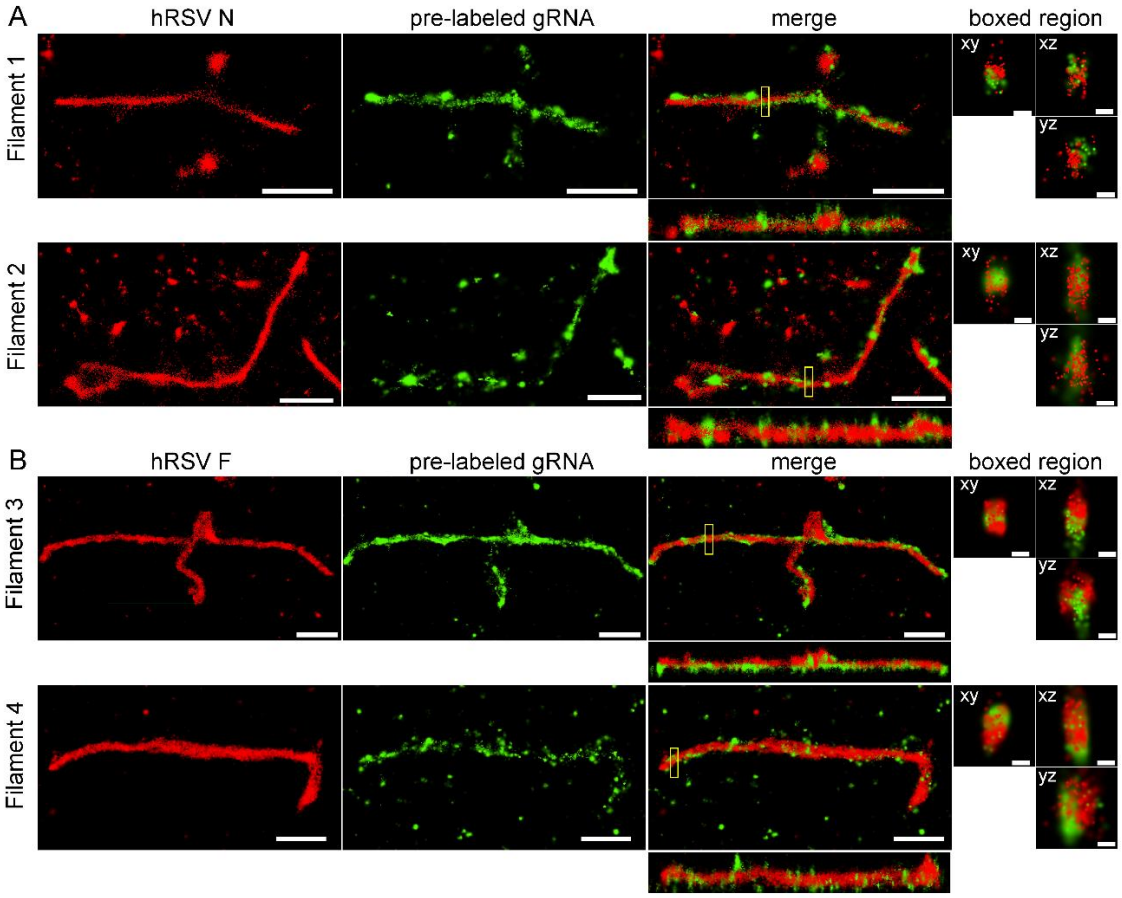

C

Image	hRSV N or F		Pre-labeled gRNA	
	Lateral FWHM[a] (nm)	Axial FWHM (nm)	Lateral FWHM (nm)	Axial FWHM (nm)
Filament 1	117	76	125	85
Filament 2	152	88	215	75
Filament 3	154	144	163	91
Filament 4	196	158	217	72

[a]FWHM – full width half maximum of point count

Figure 3.1 dSTORM images reveal spatial relationships between viral gRNA and viral proteins. (**A**) Two viral filaments showing the distribution of hRSV N (red), pre-labeled gRNA (green), and merged image. A side view of the filament is show below each merged image. The yellow boxed region represents a 100 nm long cross-section through the filament; the magnified xy (top), xz (side), and yz (front) projections of the cross-section are shown to the right of the merged image. (**B**) Two viral filaments showing the distribution of hRSV F (red), pre-labeled gRNA (green), and merged image. Side view and boxed region similar to those in Figure 4A. (**C**) A table describing the measured full-width half-maximum (FWHM) of the point count of the boxed regions. Lateral FWHM derived from yz projection of cross-section shown in boxed region. Axial FWHM derived from xz projection of cross-section shown in boxed region. Scale bars 1 µm for whole filaments and 100 nm for boxed region.

Imaging M and M2-1 using dSTORM

Next, we decided to verify our conventional fluorescence results on the localization of M2-1, as well as understand its spatial relationship to M and the genomic RNA. Our dSTORM images show that both M (**Fig. 3.2A**) and M2-1 (**Fig. 3.2B**) are continuously distributed along the length of the viral filament, whereas the genomic RNA (at least in terms of the sites that the RNA probes bind to) is discontinuously distributed along the length of the filament. Upon closer inspection of a side view of the filament, and of the full-width half-maximum (FWHM) of the protein and RNA signals (**Fig. 3.2C**), it is clear that the M2-1 layer is in slightly closer proximity to the genomic RNA than the M layer. These results verify that M2-1 is present in isolated filamentous virions and might serve as an adaptor between the M and genomic RNA.

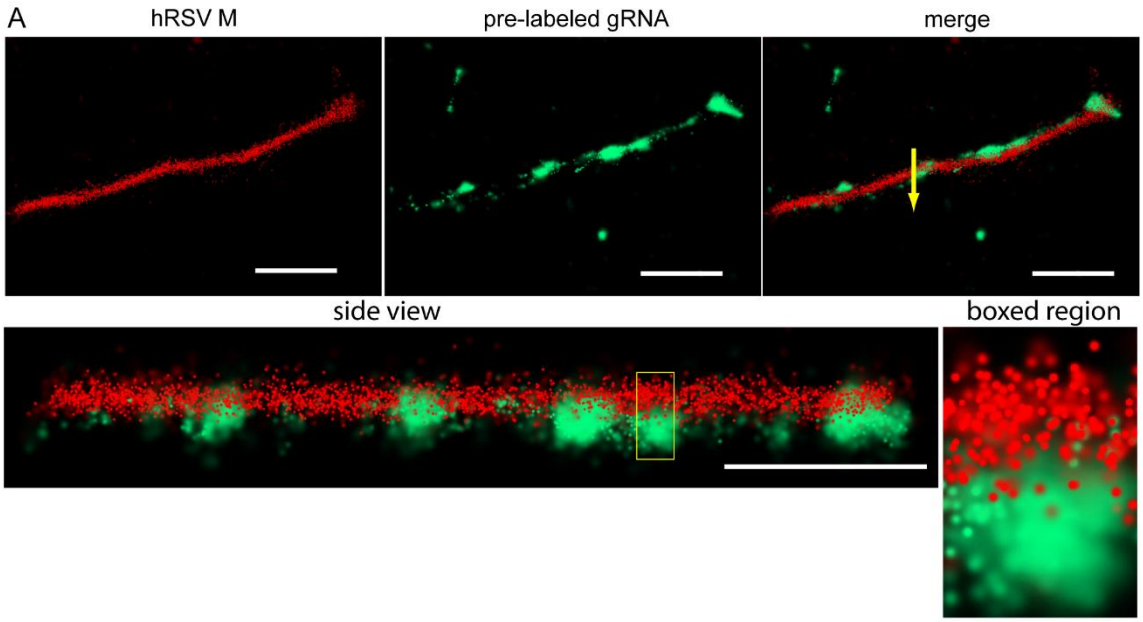

C

Image	Protein Axial FWHM (nm) (n=2)	gRNA Axial FWHM (nm) (n=2)
M and gRNA	153±28.3	81.0±28.3
M2-1 and gRNA	130±12.0	87.5±17.7

[a]FWHM – full width half maximum of point count

Figure 3.2 dSTORM imaging of RSV filamentous virions. (A) Single RSV filamentous virion on glass, with RNA imaging probes targeting the RSV genomic RNA (green) delivered to it prior to isolation from cells and immuno-stained for viral M protein (red). A merged image of M and RNA and a side view are also shown. Magnified images of the boxed region in the side view are shown to the right. Arrow in the merge represents an example 100nm cross section used to measure the axial FWHM. (B) Single RSV filamentous virion on glass with RNA imaging probes that was immuno-stained for the viral M2-1 protein. Similar views to Figure 10A are shown. (C) Table containing axial full-width half maximum measurements (FWHM) of the point count for the viral protein and RNA in the 100 nm boxed region of the filaments shown in A and B. This measurement was repeated for 2 filaments for each protein. Scale bars are 1 µm for whole filaments.

Discussion and conclusion

Our labeling method combined with dSTORM enabled the analysis of RNA/protein distributions in virions with fluorescence at a resolution (~20 nm laterally) smaller than the width of a virion (200 nm width of filament).[10,11]. From these images it is clear that there is likely more N protein than genomic RNA, and some of it may not always be in contact with the RNA. This is not that surprising, because in studies where F, G, M, P and N have been expressed in cells without the RNA, N still localizes to filaments, suggesting an additional mechanism for N localization. Taking this one step further, one unanswered question would be whether these consist of free N protomers, or are actually empty polymerized N capsids. One way to possibly determine this would be to examine the localization of P, which at least one group believes is responsible for maintain free N (at least early on in infections) and therefore preventing the premature formation of empty capsids.[12]

Given the fact that the gRNA was distributed throughout the length of the filament, and that gRNA granules were quite large (~80 nm laterally), it is likely that there is more than one copy of the hRSV genome within large filamentous virions, especially since the helical gRNA and N complex is thought to be only 10 nm wide.[13] This is not the case for other filamentous virions such as the filovirus Ebola, which makes filamentous virions that contain only one genome[14] and is part of the same *Mononegavirales* order as hRSV. Ebola though, tends to make much smaller filaments than RSV. The correlation between incorporation of multiple copies of RNA viral genomes and viral replication efficiency though has yet to be established. Future work could include using localization microscopy to investigate the distribution of other viral

proteins such as the matrix (M) protein and cellular proteins (such as F-actin) within the filament. This approach might help better define principal mechanistic determinants of filament formation, which are still unclear.[15-20]

As for M2-1, it has been speculated to be a connection between the M and the N proteins[21]. However, it is also been speculated to interact with the RNA and P[22,23], so the question of exactly what protein M2-1 directly interacts with is still in question. Also, while we show that the M2-1 exists as a layer, similar to [21], a recent crystal structure of most of the protein (minus the flexible C terminus) disputes the idea of layer formation by finding no M2-1 to M2-1 interaction domain.[24] It is possible that the interaction of these two proteins exists in the structure of the flexible C terminus that was unresolvable. However, it is also possible that the M2-1 is distributed discontinuously at a spacing of <35nm, at which point our dSTORM imaging would no longer be able to resolve it.

Clearly, our methods of labeling and isolating virus are compatible with dSTORM and can yield valuable information on the structure of the virus without having to modify the probe design.

Materials and methods

Cells or virus on coverslips were fixed in 4% paraformaldehyde (Electron Microscopy Sciences) in PBS for 10 min at room temperature before permeabilization with 0.2% Triton X-100 (Sigma) for 5 min at room temperature. This step was followed by blocking with 5% bovine serum albumin for 30 min at 37 °C, washing with PBS, primary antibody incubation for 30 min at 37 °C, washing with PBS, secondary antibody incubation 30 min at 37 °C, and a final washing with PBS. Multiple antibody labeling was done simultaneously after checking for cross-reactivity. Cells were then stained with DAPI, and all samples were mounted with Prolong Gold (Invitrogen). For virus on glass, before fixation, virus was centrifuged through 5 μm and 0.45 μm filters (Millipore) at 5,000 x *g* and 4 °C for 4 min and 1 min respectively, to isolate single filaments from infected cells. This size fraction was then spun down onto poly-L-lysine (Sigma) coated coverslips via centrifugation at 3,007 x g and 4 °C for 30 min. Virus was then fixed and immuno-stained using the above method. For simultaneous staining of M and M2-1 (both antibodies raised in a mouse), several steps were added. After permeabilization and blocking, cells were incubated with M2-1 primary, then rabbit anti-mouse Fab fragment (Jackson Immunoresearch), then a donkey anti-rabbit secondary antibody, followed by a light fixation in 1% paraformaldehyde in PBS for 10 min at room temperature. All incubations were for 30 min at 37 °C and cells were washed twice with PBS between each incubation. Afterwards, cells were stained for viral M and F according to the standard protocol above.

For imaging, primary antibodies used were: mouse anti-hRSV N (Abcam), human anti-hRSV F (MedImmune), mouse anti-RSV M (B135, a gift from James E. Crowe Jr.'s

lab), mouse anti-RSV M2-1 (5H5, Abcam). Secondary antibodies used were: donkey anti-mouse Alexa Fluor 488 (Invitrogen), donkey anti-human DyLight 650, and donkey anti-human Alexa Fluor 647 (Jackson Immunoresearch).

dSTORM imaging was performed according to the following. Super-resolution images were recorded with a Vutara SR 200 (Vutara, Inc., Salt Lake City, UT) commercial microscope based on the Single molecule localization (SML) biplane FPALM technology.[4,5]

Viral proteins and MTRIP probes were imaged using a 647 nm and 561 nm excitation lasers, respectively, and 405 nm activation laser in a photoswitching buffer comprised of 20 mM cysteamine and oxygen scavengers (glucose oxidase and catalase) in 50mM Tris+10 mM buffer at pH 8.0. Images were recorded using a 60X, NA 1.2 water immersion objective (Olympus) and Evolve 512 EMCCD camera (Photometrics) with gain set at 50, frame rate at 50 Hz and maximal powers of 647 nm, 561 nm or 405 nm lasers set at 8, 8, or 0.05 $kWcm^{-2}$, respectively. Total number of frames acquired per channel ranged from 2,000 to 4,000 frames.

Data was analyzed by the Vutara SRX software (version 4.07). Single molecules were identified by their brightness frame by frame after removing the background. Identified particles were then localized in three dimensions by fitting the raw data in a customizable region of interest (typically 16x16 pixels) centered on each particle in each plane with a 3D model function which was obtained from recorded bead data sets. Fit results were stored as data lists for further analysis. The image resolution capable of experimentally being achieved is 20 nm laterally (x and y) and 50 nm axially (in z).

References

1.van de Linde, S. *et al.* Direct stochastic optical reconstruction microscopy with standard fluorescent probes. *Nat Protoc* **6,** 991-1009 (2011).

2.Rust, M. J., Bates, M. & Zhuang, X. Sub-diffraction-limit imaging by stochastic optical reconstruction microscopy (STORM). *Nat. Methods* **3,** 793-5 (2006).

3.Hess, S. T. & Mason, M. D. Ultra-high resolution imaging by fluorescence photoactivation localization microscopy. *Biophysical journal* **91,** 4258-72 (2006).

4.Juette, M. F. *et al.* Three-dimensional sub-100 nm resolution fluorescence microscopy of thick samples. *Nat. Methods* **5,** 527-9 (2008).

5.Mlodzianoski, M. J., Juette, M. F., Beane, G. L. & Bewersdorf, J. Experimental characterization of 3D localization techniques for particle-tracking and super-resolution microscopy. *Opt Express* **17,** 8264-77 (2009).

6.Huang, B., Jones, S. A., Brandenburg, B. & Zhuang, X. Whole-cell 3D STORM reveals interactions between cellular structures with nanometer-scale resolution. *Nat. Methods* **5,** 1047-52 (2008).

7.Löschberger, A. *et al.* Super-resolution imaging visualizes the eightfold symmetry of gp210 proteins around the nuclear pore complex and resolves the central channel with nanometer resolution. *J. Cell. Sci.* **125,** 570-5 (2012).

8.Pereira, C. F., Rossy, J., Owen, D. M., Mak, J. & Gaus, K. HIV taken by STORM: super-resolution fluorescence microscopy of a viral infection. *Virology Journal* **9,** 84 (2012).

9.Laine, R. F. *et al.* Structural analysis of herpes simplex virus by optical super-resolution imaging. *Nature Communications* **6,** 5980 (2015).

10.Bächi, T. & Howe, C. Morphogenesis and ultrastructure of respiratory syncytial virus. *J. Virol.* **12,** 1173-80 (1973).

11.Roberts, S. R., Compans, R. W. & Wertz, G. W. Respiratory syncytial virus matures at the apical surfaces of polarized epithelial cells. *J. Virol.* **69,** 2667-73 (1995).

12.Green, T. J. *et al.* Common mechanism for RNA encapsidation by negative-strand RNA viruses. *J. Virol.* **88,** 3766-75 (2014).

13.Tawar, R. G. *et al.* Crystal structure of a nucleocapsid-like nucleoprotein-RNA complex of respiratory syncytial virus. *Science* **326,** 1279-83 (2009).

14.Bharat, T. A. M. *et al.* Structural dissection of Ebola virus and its assembly determinants using cryo-electron tomography. *Proc. Natl. Acad. Sci. U.S.A.* **109,** 4275-80 (2012).

15.Santangelo, P. J. & Bao, G. Dynamics of filamentous viral RNPs prior to egress. *Nucleic Acids Res.* **35,** 3602-11 (2007).

16.Burke, E., Dupuy, L., Wall, C. & Barik, S. Role of cellular actin in the gene expression and morphogenesis of human respiratory syncytial virus. *Virology* **252,** 137-48 (1999).

17.Gower, T. L. *et al.* RhoA signaling is required for respiratory syncytial virus-induced syncytium formation and filamentous virion morphology. *J. Virol.* **79,** 5326-36 (2005).

18.Jeffree, C. E. *et al.* Ultrastructural analysis of the interaction between F-actin and respiratory syncytial virus during virus assembly. *Virology* **369,** 309-23 (2007).

19.Mitra, R., Baviskar, P., Duncan-Decocq, R. R., Patel, D. & Oomens, A. G. P. The human respiratory syncytial virus matrix protein is required for maturation of viral filaments. *J. Virol.* **86,** 4432-43 (2012).

20.Shaikh, F. Y. *et al.* Respiratory syncytial virus assembles into structured filamentous virion particles independently of host cytoskeleton and related proteins. *PloS one* **7,** e40826 (2012).

21.Li, D. *et al.* Association of respiratory syncytial virus M protein with viral nucleocapsids is mediated by the M2-1 protein. *J. Virol.* **82,** 8863-70 (2008).

22.Blondot, M. *et al.* Structure and functional analysis of the RNA- and viral phosphoprotein-binding domain of respiratory syncytial virus M2-1 protein. *PLoS Pathog.* **8,** e1002734 (2012).

23.Tran, T. *et al.* The respiratory syncytial virus M2-1 protein forms tetramers and interacts with RNA and P in a competitive manner. *J. Virol.* **83,** 6363-74 (2009).

24.Tanner, S. J. *et al.* Crystal structure of the essential transcription antiterminator M2-1 protein of human respiratory syncytial virus and implications of its phosphorylation. *Proc. Natl. Acad. Sci. U.S.A.* **111,** 1580-5 (2014).

CHAPTER 4

IMAGING RSV USING STED

The work presented here is excerpted from the following publications: Liu, Y., Ding, Y., Alonas, E., Zhao, W., Santangelo, P.J., Jin, D., Piper, J.A., Teng, J., Ren, Q., & Xi, P. Achieving λ/10 resolution CW STED nanoscopy with a Ti:Sapphire oscillator. *PLoS One* **7**, e4003 (2012) and Yang, X., Xie, H. Alonas, E., Liu, Y., Chen, X., Santangelo, P.J., Ren, Q., & Jin, D. Mirror confined axial super-resolution microscopy. *Submitted*.

Background

While we achieved excellent results using localization microscopy, there are still some questions in the field as to its quantitative nature. In particular, these relate to protein labeling issues, detection efficiency issues, uncertainty in localization, repeated blinking of the same molecule, and drift.[1] Indeed, there are several competing algorithms and software packages for localization microscopy that produce varied results. [2] As such we attempted to image the virus using stimulated emission depletion microscopy (STED). As a purely optical technique[3], STED should be immune to any computational artifacts.

As originally described, STED required two picosecond, pulsed lasers delivering a high energy density to the sample.[3] The technique was later generalized to use diode lasers[4], continuous wave lasers[5,6], and various two-photon schemes.[7-10] Given the complexities of multi-laser STED, we demonstrated a synchronization-free CW STED microscope with a 6-Watt Diode-pumped Solid State (DPSS) 532 nm laser pumped

Ti:Sapphire laser tuned to CW mode, which is a source broadly available in many two-photon microscope systems.

We also attempted to further increase the resolution of our STED microscopy using mirrors. By adding a first surface mirror under the sample, the PSF should be confined axially due to the formation of a standing wave.[11]. This setup is much less complicated than TIRF, in which the excitation is confined to a ~100nm plane above the coverglass [12]; 4Pi, in which two opposing objectives must be carefully aligned[13]; and I^5M, which also requires very close alignment.[14]

One of the few challenges with STED is that the sample must be illuminated with fairly high power density, leading to increased photobleaching. In order to counteract this, we were required to change mounting media[15] for some of the fluorophores used.

Imaging samples using a de-mode locked Ti:Sapphire

Figure 4.1 illustrates the schematic setup and preliminary evaluation of the stimulated emission depletion efficiencies on different fluorescent dyes. We employed a vortex 0-2π phase plate to generate the doughnut shaped depletion beam (**Fig 4.1b**) for de-exciting the fluorescence excitation (**Fig. 4.1a**) by stimulated emission.[16] We also show an example STED point-spread function (**Fig 4.1c**). As the resolution is determined by the depletion efficiency and not the diffraction limit, we first studied the effect of the depletion ratio η_{CW} of the spontaneous fluorescence by overlapping the STED focus (without phase modulation) with the excitation focus[17]. The saturation intensity I_s (in which the possibility of spontaneous emission and stimulated emission is equal) is measured to be ~17 MW/cm^2 for crimson beads, ~14.4 MW/cm^2 for DyLight 650 and

~23.8 MW/cm^2 for ATTO647N (**Fig. 4.1d**). The reciprocal fitting of $\eta_{CW} = (1 + I_{\mathrm{mod}} / I_s)^{-1}$ agrees well with the experimental data. When the STED beam was switched off, the system worked as a normal confocal system, which was used to obtain data for comparison.

To demonstrate the resolving power of the CW STED nanoscope, we attempted to image microtubules. We acquired a normal confocal image (**Fig. 4.2a**) and a STED image (**Fig. 4.2b**). We further processed the STED image by deconvolving it using a Richardson-Lucy algorithm (**Fig 4.2c**). From the microtubule network of a Vero cell we could see that STED nanoscopy provides ~120 nm FWHM with DyLight 650 staining microtubules (**Fig. 4.2d**). If the size of the microtubule (~25 nm diameter) is deducted, the actual resolution is ~110 nm.

Finally, we attempted, using our de-mode locked Ti:Sapphire setup, to image an RSV infected cell. A lateral resolution of 82 nm was achieved using STED (**Fig. 4.3b,e,f**), compared to a lateral resolution of 290 nm on confocal (**Fig. 4.3a,d,c**).

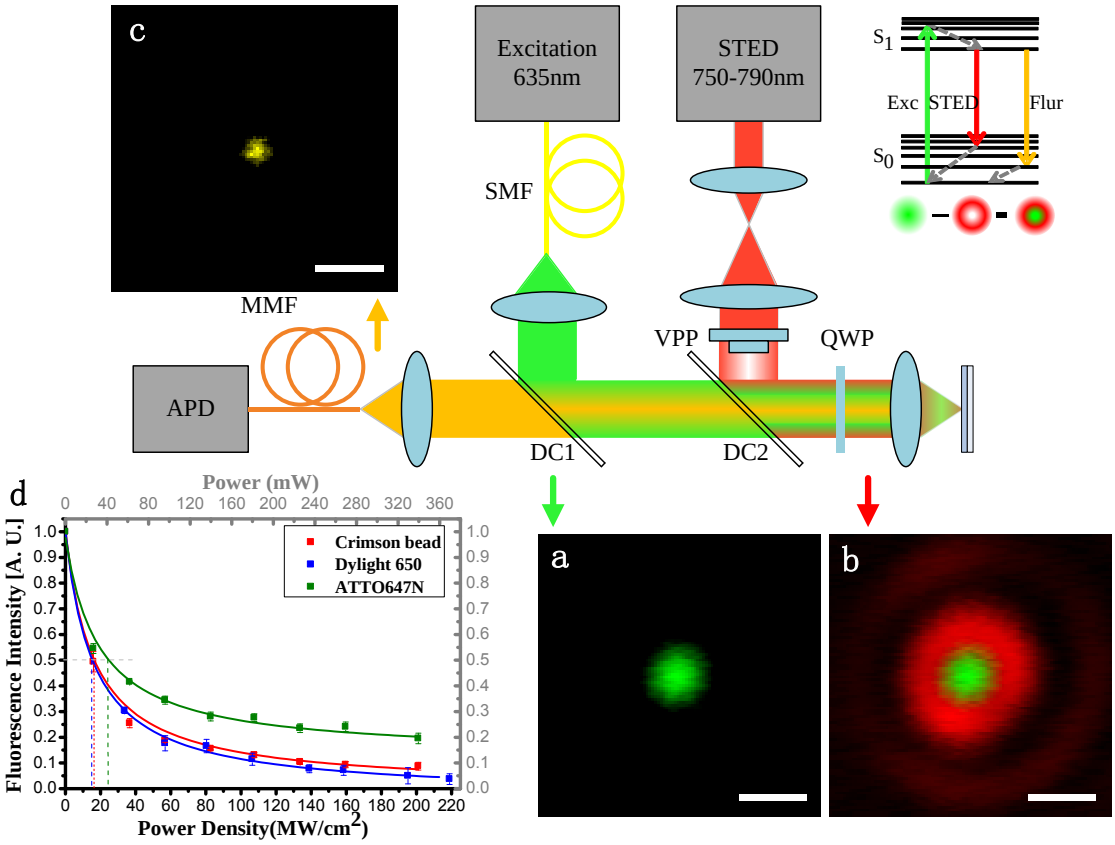

Figure 4.1 Schematic diagram of the STED system setup. The green line represents the excitation 635 nm laser, red line is the CW Ti:Sapphire STED beam, and the yellow line represents the fluorescence signal. SMF: single mode fiber; MMF: multi-mode fiber; DC1 and DC2 are dichotic filters. VPP: vortex 0-2π phase plate; QWP: quarter-wave plate; the excitation PSF (a), doughnut depletion PSF overlapped with excitation PSF (b), and STED PSF (c) clearly shows the process of super-resolution. Scale bar: 500 nm. (d): the modulation efficiency versus the depletion intensity measured with crimson beads, DyLight 650 and ATTO647N solution. The STED wavelengths are 763 nm for crimson beads and Atto647N, and 783 nm for DyLight 650, respectively.

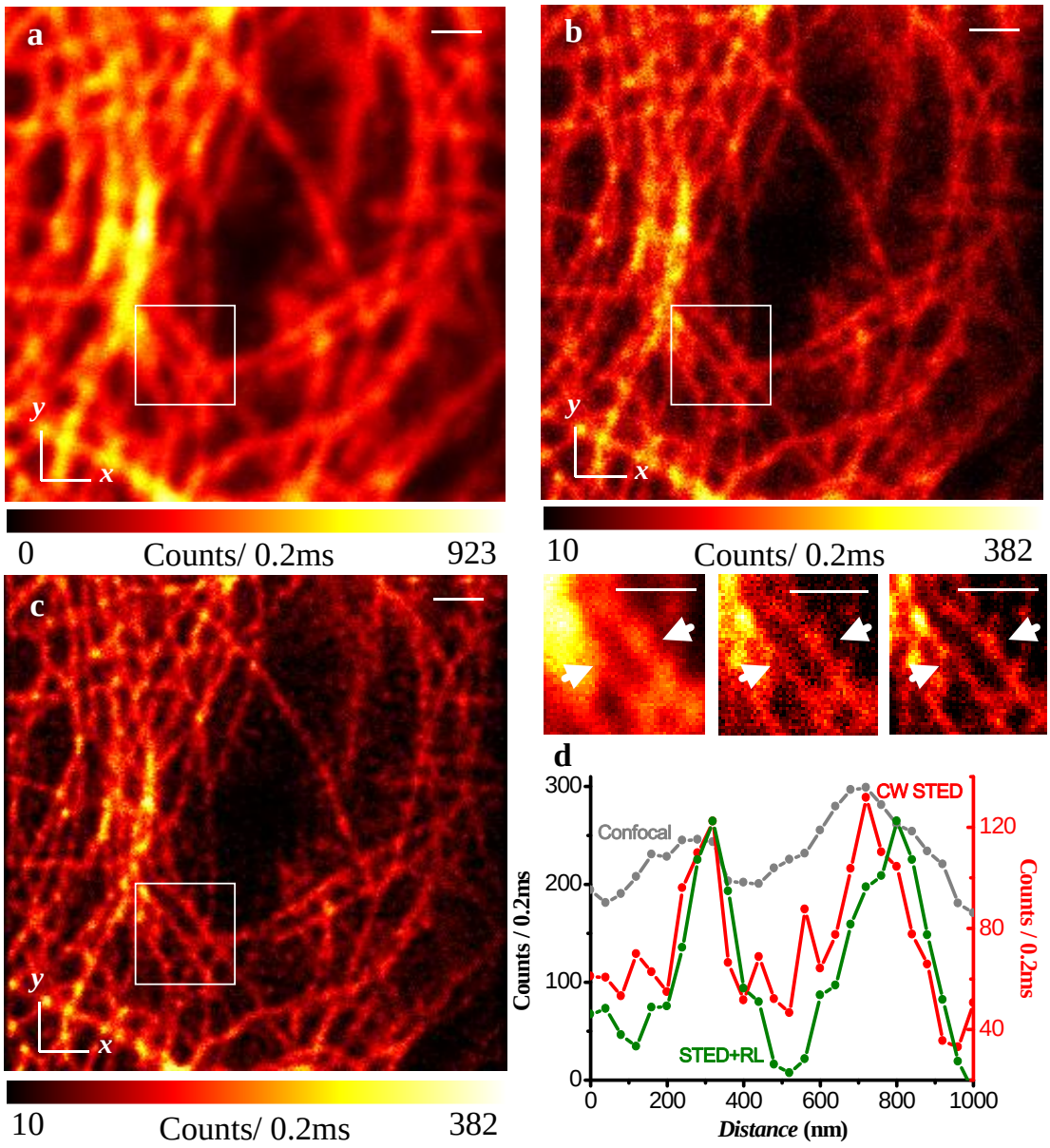

Figure 4.2 STED imaging of microtubules. Confocal (a), corresponding CW-STED (b), and R-L deconvolved (c) images of microtubules in a Vero cell stained with DyLight 650. The intensity at the cross-section marked in a, b, and c inlets are plotted in (d). The wavelength and power density for STED beam is 783 nm and ~220 MW/cm^2. Scale bar: 1 μm.

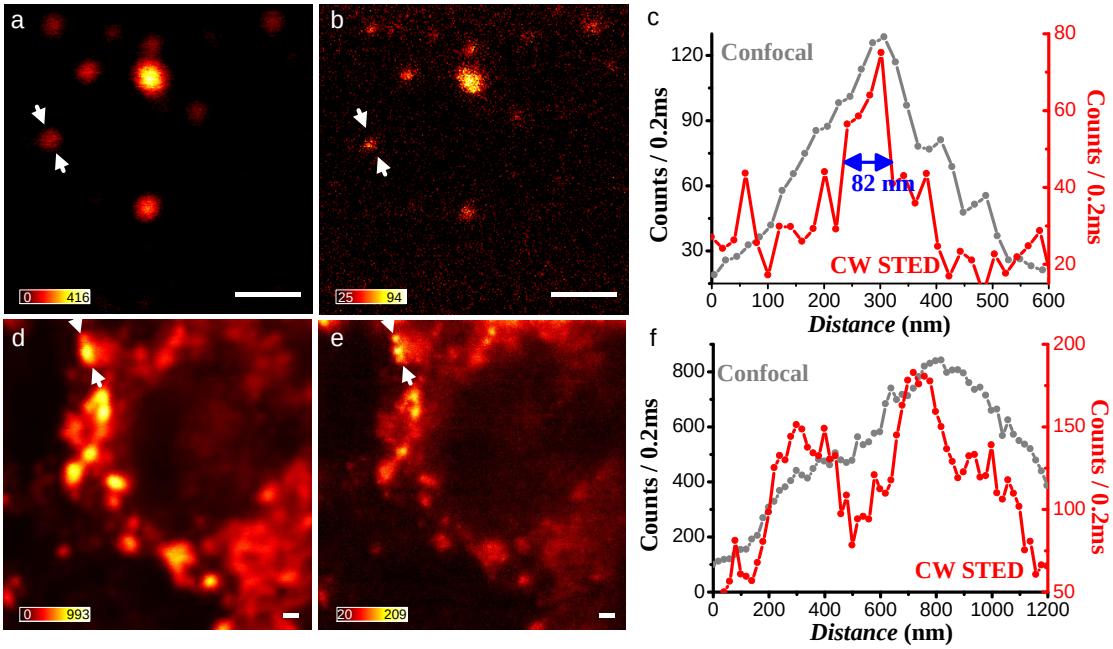

Figure 4.3 STED imaging of RSV gRNA. Confocal (a, d) and corresponding CW-STED (b,e) images of hRSV genomic RNA granules in a HEp2 cell. The intensity at the cross-section marked in d and e are plotted in (e, f). The wavelength and power intensity for STED beam is 783nm and ~180 MW/cm^2. Pixel dwell time: 0.2 ms. Scale bar: 1 µm.

Imaging samples using mirror enhanced STED

In order to increase the resolution further, we turned towards preparing samples on first surface mirrors. A small silicon dioxide coating, the thickness of which we varied from 50 nm to 150 nm, was sufficient to allow protein adsorption and cellular adhesion. We then examined the microtubules again on a normal confocal setup, taking a z-stack at regular intervals (**Fig. 4.4**). The first few images (**Fig. 4.4a,b,c**) were the standard confocal images since those sections were still far away from the interference plane created by the mirror. The plane is approached in the next few images (**Fig. 4.4d,e**). Within the interference plane, the next few images show different signal-to-noise ratios (**Fig. 4.4e-g**), with one particular z-plane representing the maximum signal to noise contrast. This plane represents the maximum constructive interference of incident excitation beam and reflected beam (**Fig. 4.4f**). As the plane of focus gets too close to the mirror (**Fig. 4.4h**), the image is heavily blurred as a result from multiple interferences. However, so long as the objective is focused on the right plane, we expected resolution enhancement.

As an aside, this mirror enhanced microscopy is also compatible to spinning disk confocal microscopy, with the potential application of doing live cell microscopy. We imaged the microtubules (red) and nuclear pore complex (green) of a Vero cell grown on the mirror substrate under a commercial spinning disk microscope (**Fig. 4.5**). We employed an oil immersion objective (100X, N.A. =1.4, Nikon), and 488nm and 647nm as the excitation wavelengths, respectively. Comparing the mirror enhanced spinning disk image (at z = 2.0 μm) to the spinning disk confocal images in 0-1.5 μm, it is clear that the image signal was enhanced.

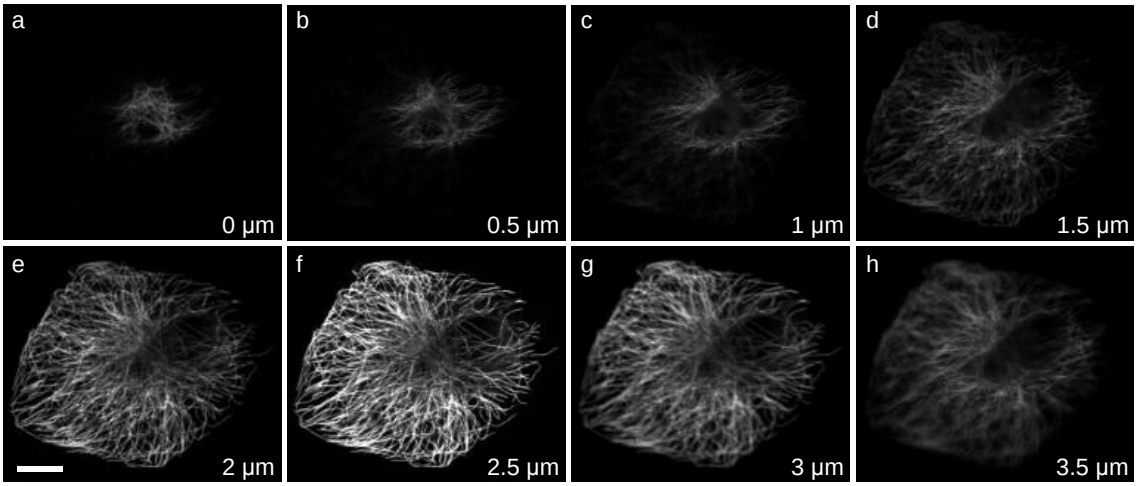

Figure 4.4 Image z-stacks of mirror confocal microscopy. This stack of microtubule images was taken with an Olympus FV-1200, with apochromatic 60×, water immersion objective, NA=1.42. The 8 sequential images at steps of every 0.5 µm away from the top surface (0 µm) towards the mirror substrate were recorded. Scale bar, 10 µm.

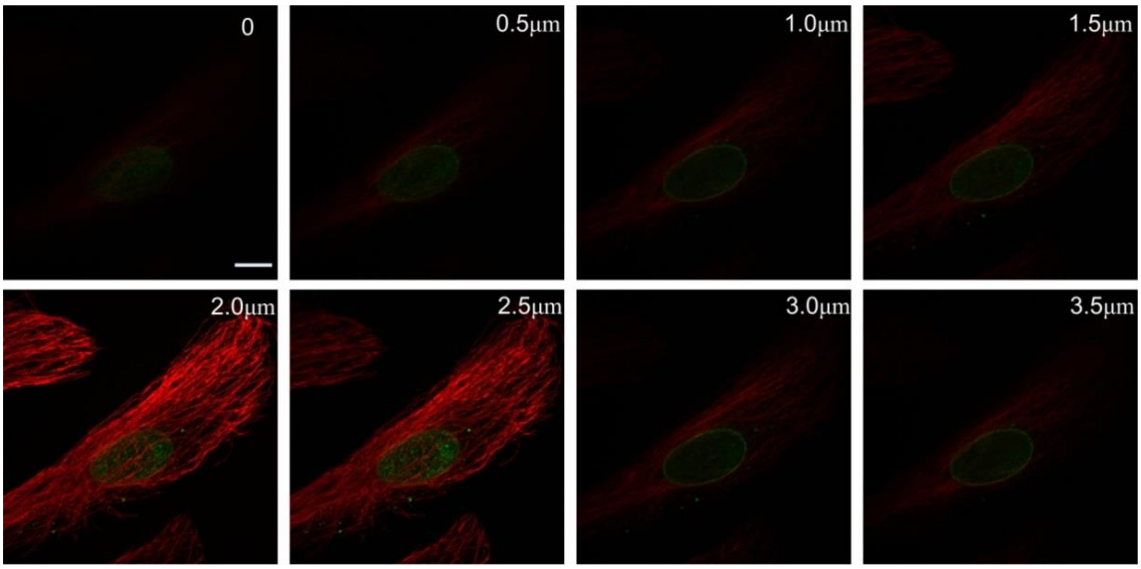

Figure 4.5 Image z-stacks of mirror-enhanced spinning disk confocal microscopy. The 8 sequential images at steps of every 0.5 µm away from the top surface (0 µm) towards the mirror substrate were recorded. Clearly the images 0µm –1.5µm were the standard confocal images since those sections were still far away from the MEANS modality region. The difference between image (1.5µm) and image (2.0µm) indicated that the confocal modality was transferred to the MEANS modality so that a particular section of the cell suddenly showed up. The image (2.0µm) achieved maximum signal to noise contrast indicating the best interference of incident excitation beam and reflected beam. Although image 1.5µm) and (2.5µm) are at the same distance from image (2.0µm), the images at a distance of 3.0 and 3.5um from the top surface is heavily blurred as a result from the multiple interference arises when the focal spot is too close to the mirror. Scale bar, 10 µm.

To combine our mirror-enhanced sample prep with STED nanoscopy, we imaged samples using the commercial Leica TCS SP8 STED 3X super resolution microscope without additional complexity and cost added to the system. First, we began by staining the FXFG Nup proteins of the nuclear pore complex (NPC). These Nups, so named for their phenylalanine-glycine motifs, form the center of the pore and therefore will have the smallest diameter.[18] The NPC has been a popular choice for judging the resolution of other super-resolution systems.[19-21] For our mirror enhanced STED, we were able to achieve 19 nm lateral resolution to visualize the fine inner rim of the NPCs (radius of 26.5nm) using a relatively low 592-nm depletion laser power of 60 mW measured at the back aperture of the objective (**Fig. 4.6a,b,c,d**). Clearly, the mirror approach works with STED.

Finally, we attempted to image our isolated RSV filamentous virions. We stained the F protein on the viral envelope by AlexaFluor 488, and the inside N protein by DyLight 650. Without the mirror, and despite using higher STED depletion power (108 mW at 592 nm) than the MEANS-STED (72 mW), the conventional STED with the axial PSF of over 500 nm cannot resolve the two sides of the viral membrane because too much of the F protein along the top of the filament is being illuminated (**Fig. 4.6e,f,g,h,i**). However, with the mirror-enhancement confining the excitation axially, it is clear that the F protein is on two sides of the membrane, with the N protein in the middle (**Fig. 4.6j,k,l,m,n**).

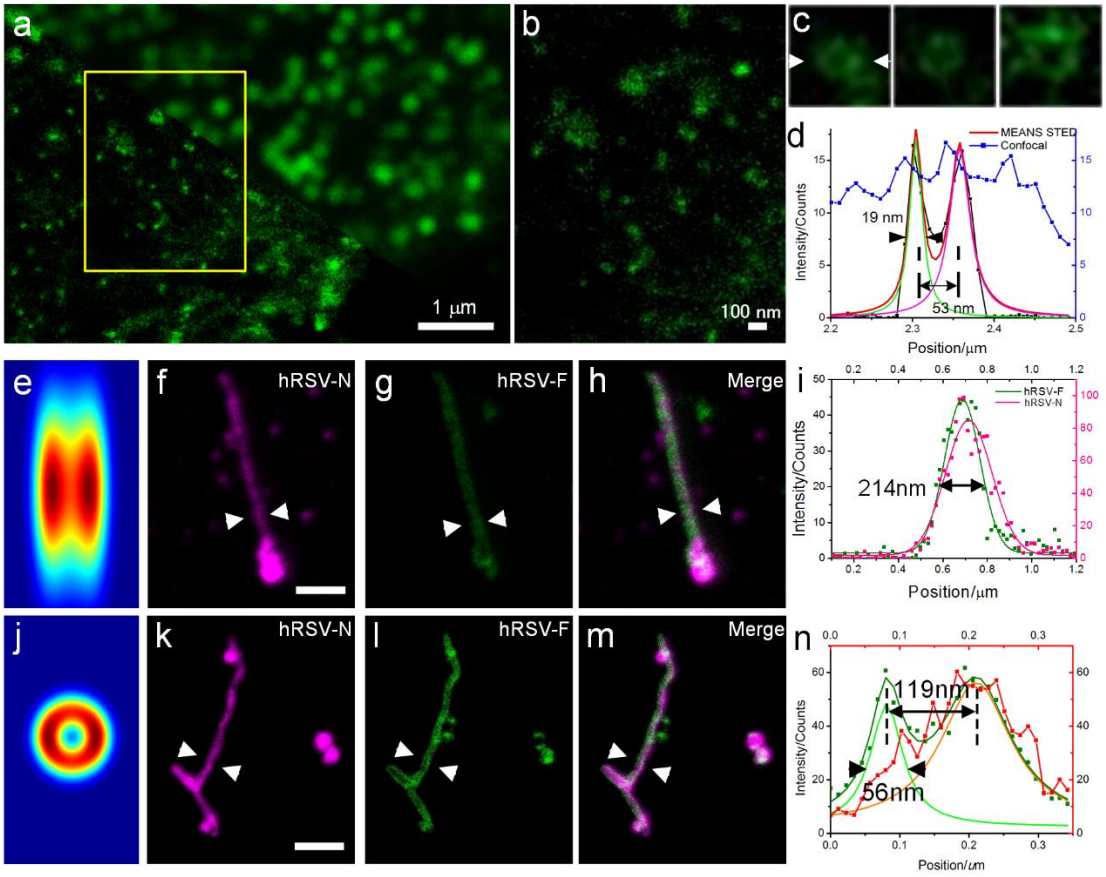

Figure 4.6 NPC and RSV filament imaged using mirror enhanced STED. Mirror enhanced STED gives clearly lateral resolution enhancement in (a). (b) Magnified the boxed area in (a), in which the porous structure of the NPCs can be clearly seen. (c) shows several magnified individual NPCs. (d) is the plot of the intensity distribution along arrows in (c). To demonstrate the advantage of axial confinement the RSV filaments are imaged with conventional STED (on coverglass, f-h) and mirror enhanced-STED (on mirror, k-m). The simulation of the convolution of conventional STED PSF vs. mirror-STED PSF with the tubule structure are shown in (e) and (j), respectively. The split in (k) and (m) indicates the hollow structure of the RSV-F, taking advantage of the optical sectioning of mirror enhanced-STED. (i,n) are the intensity plots of the line indicated by the white arrows in (h) and (m), respectively. Scale bar, 1 μm.

Discussion and conclusion

We have applied CW STED nanoscopy onto the microtubule network and RSV genomic RNA, using a Ti:Sapphire laser tuned to CW mode from a two-photon microscopy setup, and we achieved a super-resolution of 71 nm laterally which is only one-tenth the emission wavelength. We further demonstrated for the first time that STED nanoscopy can discern the DyLight 650-MTRIP labeled viral RNAs in Hep-2 cells, with a resolution of 82 nm. This work might broaden the use of STED nanoscopy, as a Ti:Sapphire laser is a common component of two-photon systems.

We have also demonstrated the use of mirror enhanced STED using the microtubules, the nuclear pore complex, and RSV. The working distance for mirror enhanced super-resolution can be adjusted somewhat by customizing the thickness of the silica coating, and the setup is much simpler than other axial confinement techniques. However, one disadvantage is the lack of 3D optical sectioning capability.

Materials and methods

The Ti:Sapphire un-mode locked STED system was built based on a home-made confocal imaging system with 635 nm excitation. A Ti:Sapphire laser (Griffin-F, KMLabs, USA) pumped by a 6-Watt DPSS 532nm laser (Finesse-6W, Laser Quantum, UK) was employed for the CW STED source. The output from the laser source is ~800mW. To generate the doughnut PSF for effective depletion, a vortex 0-2π phase plate (VPP-A, RPC Photonics) was used. We focused the beams into samples using an oil-immersion objective of NA=1.4 (100x, PlanAPO, Zeiss). To obtain a 2-D image, a piezo scanning stage (Nanomax, Thorlabs) was employed to move the specimen. A photo-counting avalanche photodiode (SPCM-AQRH-13-FC, Perkin Elmer) was used to collect the fluorescence signal. The scanning and data collection were performed with a DAQ board (USB-6259, National Instruments), and image collection was accomplished with Imspector (Max-Plank Innovation, Goettingen, Germany).

Tubulin cell culture conditions were as follows. Vero cells (ATCC CCL-81) were maintained in High Glucose DMEM (Lonza) with 10% FBS (Hyclone), 100 U ml-1 penicillin, and 100 μg ml-1 streptomycin (Invitrogen). Cells were plated the day before fixation at 25% confluency. Cells were fixed with 100% methanol (VWR) for 10 min at -20 °C and permeabilized with 100% acetone (VWR) for 2 min at -20 °C. Nonspecific antibody binding was blocked with 5% bovine serum albumin (EMD) in PBS for 30 min at 37 °C. Cells were then incubated with a primary antibody against alpha tubulin (rabbit, Abcam ab18251) for 30 min at 37 °C, washed twice in PBS, incubated with a polyclonal secondary antibody (goat anti-rabbit DyLight 650, Pierce) for 30 min at 37 °C,

washed twice in PBS, and mounted in mixture of Mowiol 4-88 (Sigma) and DABCO (VWR).

To effectively image the genomic RNA of hRSV in HEp-2 cells, MTRIP probes, labeled with DyLight 650 and targeted against the hRSV genomic RNA, were delivered into live cells with streptolysin O and hybridized to the genomic RNA, 48 hr after infection. The cells were then fixed in 4% paraformaldehyde and mounted in 80% glycerol containing glucose, glucose oxidase, catalase, and beta mercaptoethanol.

The cells were grown on the first-surface mirrors as follows. The mirrors were sterilized with 70% ethanol, washed with water, and then incubated with complete growth media on the top surface for 1 hr at 37°C. Vero cells, cultured according to the aforementioned conditions, were trypsinized and once in suspension, were placed on top of the mirror and allowed to incubate for 1 hr at 37°C before adding more complete media.

Primary antibodies used were rabbit anti-alpha tubulin (polyclonal IgG, Abcam catalog: ab18251) and mouse anti-NPC proteins that contain FXFG repeats (monoclonal IgG, Abcam catalog: ab24609). Secondary antibodies used were goat anti-rabbit DyLight 650 (Pierce) and donkey anti-mouse AlexaFluor 488 (Life Technologies).

In order to capture single hRSV filamentous virions on glass, hRSV A2 was propagated in HEp-2 cells at an MOI of 0.1. At 4 days post infection, the cell-associated and supernatant fractions were scraped, freeze-thawed, and spun through 5-μm- and 0.45-μm-pore-size centrifugal filters (Millipore) at 5,000×g and 4°C for 4 min and 1 min, respectively. The fraction between 0.45μm and 5μm in diameter was collected and immobilized onto a poly-L-lysine (Sigma)-coated first-surface mirror or cover glass by

adsorption of 500uL of filtered virus for 2 hr at 4 °C. The immobilized virions were fixed using 4% paraformaldehyde and immunostained according to the aforementioned protocol. Antibodies used were anti-RSV F monoclonal (palivizumab, MedImmune) and anti-RSV N monoclonal (clone B023, Abcam). Coverslips were mounted in a mixture of Mowiol and DABCO (VWR).

The MEANS-STED imaging was performed with a Leica TCS SP8 STED 3X system equipped with a white light laser as excitation, and 592nm and 660 nm for STED depletion. The HyD detector and 100x oil-immersion objective (N. A. 1.4) were employed. Time-gated detection were also used, in which for AlexaFluor-488 the detection is delayed 0.5ns, whereas for Cy5 the detection is delayed 1ns.

References

1.Shivanandan, A., Deschout, H., Scarselli, M. & Radenovic, A. Challenges in quantitative single molecule localization microscopy. *FEBS Letters* **588,** 3595-602 (2014).

2.Sage, D. *et al.* Quantitative evaluation of software packages for single-molecule localization microscopy. *Nat. Methods* (2015). doi:10.1038/nmeth.3442

3.Hell, S. W. & Wichmann, J. Breaking the diffraction resolution limit by stimulated emission: stimulated-emission-depletion fluorescence microscopy. *Optics Letters* **19,** 780-782 (1994).

4.Westphal, V., Blanca, C. M., Dyba, M., Kastrup, L. & Hell, S. W. Laser-diode-stimulated emission depletion microscopy. *Applied Physics Letters* **82,** 3125 (2003).

5.Wildanger, D., Rittweger, E., Kastrup, L. & Hell, S. W. STED microscopy with a supercontinuum laser source. *Opt Express* **16,** 9614-21 (2008).

6.Willig, K. I., Harke, B., Medda, R. & Hell, S. W. STED microscopy with continuous wave beams. *Nat. Methods* (2007).

7.Moneron, G. & Hell, S. W. Two-photon excitation STED microscopy. *Opt Express* **17,** 14567-73 (2009).

8.Bacallao, R., Sohrab, S. & Phillips, C. in (2006).

9.Ding, J. B., Takasaki, K. T. & Sabatini, B. L. Supraresolution imaging in brain slices using stimulated-emission depletion two-photon laser scanning microscopy. *Neuron* **63,** 429-37 (2009).

10.Scheul, T., D'Amico, C., Wang, I. & Vial, J. Two-photon excitation and stimulated emission depletion by a single wavelength. *Opt Express* **19,** 18036-48 (2011).

11.Bailey, B., Farkas, D. L., Taylor, D. L. & Lanni, F. Enhancement of axial resolution in fluorescence microscopy by standing-wave excitation. *Nature* **366,** 44-8 (1993).

12.Axelrod, D. Total internal reflection fluorescence microscopy in cell biology. *Meth. Enzymol.* **361,** 1-33 (2003).

13.Hell, S. W., Stelzer, E. H., Lindek, S. & Cremer, C. Confocal microscopy with an increased detection aperture: type-B 4Pi confocal microscopy. *Optics Letters* **19,** 222 (1994).

14.Gustafsson,, Agard, Sedat. I5M: 3D widefield light microscopy with better than 100 nm axial resolution. *Journal of Microscopy* **195,** 10 (1999).

15.Wurm, C. A., Neumann, D., Schmidt, R., Egner, A. & Jakobs, S. Sample preparation for STED microscopy. *Methods Mol. Biol.* **591,** 185-99 (2009).

16.Keller, J., Schönle, A. & Hell, S. W. Efficient fluorescence inhibition patterns for RESOLFT microscopy. *Opt Express* **15,** 3361-71 (2007).

17.Harke, B., Keller, J., Ullal, C. K. & Westphal, V. Resolution scaling in STED microscopy. *Optics ...* (2008).

18.Alber, F. *et al.* The molecular architecture of the nuclear pore complex. *Nature* **450,** 695-701 (2007).

19.Schermelleh, L. *et al.* Subdiffraction multicolor imaging of the nuclear periphery with 3D structured illumination microscopy. *Science* **320,** 1332-6 (2008).

20.Löschberger, A. *et al.* Super-resolution imaging visualizes the eightfold symmetry of gp210 proteins around the nuclear pore complex and resolves the central channel with nanometer resolution. *J. Cell. Sci.* **125,** 570-5 (2012).

21.Szymborska, A. *et al.* Nuclear pore scaffold structure analyzed by super-resolution microscopy and particle averaging. *Science* **341,** 655-8 (2013).

CHAPTER 5

ULTRASTRUCTURAL IMAGING OF RSV

The work presented here is excerpted from the following publications: Kiss, G., Holl, J.M., Williams, G.M., Alonas, E., Vanover, D., Lifland, A.W., Gudheti, M., Guerrero-Ferreira, R.C., Nair, V., Yi, H., Graham, B.S., Santangelo, P.J., & Wright, E.R. Structural analysis of respiratory syncytial virus reveals the position of M2-1 between the matrix protein and the ribonucleoprotein complex. *J. Virol.* **88**, 7602-17 (2014) and Yi, H., Strauss, J.D., Ke, Z., Alonas, E., Dillard, R.S., Hampton, C.M., Lamb, K.M., Hammonds, J.E., Santangelo, P.J., Spearman, P.W. & Wright, E.R. Native immunogold labeling of cultured cell surfaces for cryo-electron microscopy and cryo-electron tomography applications**.** *J. Hist & Cytochem.* Online advance access (2015). Protocols for sample prep and some sample prep done by EA, image acquisition and figure making not done by EA.

Background

The ultrastructure of RSV has been previously examined using TEM[1-3] and very recently, cryo-ET.[4] However, the path to completely understanding the structure of the virion is complicated by three key challenges: first, the pleomorphic nature of the virion; second, the phenomenon that most of the infectious particles remain cell-associated in laboratory culture; and third, that the virus grows to a relatively mediocre titer in cell culture and can decrease in titer rapidly over time.[5] Traditionally, the virus is isolated by freeze-thaw, scraping, vortexing, or very gentle sonication. These processes tend to lead to contamination of the virus prep with cellular debris, complicating the ultrastructural analysis.

By and large, the field has turned to sucrose cushions and sucrose gradient ultracentrifugation to clean up the virus prep and concentrate it.[6] While we used a similar protocol for most of our ultrastructural work, this author would like to note that the loss of long filaments from the sucrose prep is most likely the result of their high sedimentation coefficient – they tend to fall out of solution during clarification using tabletop centrifugation (data not shown), although it is still possible that some are transformed into spherical particles during the course of the purification. Only through isolation by membrane centrifugation, similar to Roberts *et al.*[3], has this author seen evidence of any filamentous particles longer than 2 μm.

By now, this thesis has hinted at the importance of M2-1 for proper virus assembly; the previous work done on M2-1 will be further elaborated on here. M2-1 was first described as a structural protein, associated with other nucleocapsid proteins, by detergent extraction of purified virus.[7] The work of Garcia *et al.* demonstrated the 22kDa protein localized to inclusion bodies along with N and P, either in a wild-type infection or as part of a transfected system.[8] The first study to hint at the function of M2-1 was reported by Collins *et al.*, where a plasmid-derived minigenome system was used to show that the presence of M2-1 was necessary for the transcription of full length mRNAs.[9] The same authors later showed that in the absence of the other alternate reading frame, M2-2, the propagation of virus in infected cells resulted in lower genome replication, but in elevated levels of mRNAs.[10] Around the same time, the work of Hardy *et al.* showed that the presence of M2-1 lead to increased transcription "read-through" by the polymerase, ignoring gene end sequences.[11] This work was for the foundation of the idea that M2-1 is a transcription processivity factor.

Several different groups have worked on the structure of M2-1 since then. The N terminus of the protein contains a Cys_3His_1 motif, reminiscent of a zinc binding domain, the was suggested to either bind viral mRNAs,[12] or nonspecific cellular RNAs[13]. There are also residues within this region that are phosphorylated, originally suggested to be

threonine 56 and serine 58,[13] but later suggested to be serine 58 and serine 61 and capable of being phosphorylated by cellular casein kinase I.[12] In particular, the work of Cartee *et al.* showed that mutation of phosphorylation residues was detrimental to transcription processivity, but did not seem to affect the apparent association between M2-1 and N, which was only disrupted by the addition of RNase A.[12] This suggests that despite the potential resemblance to a zinc finger, the putative RNA binding domain is further C terminal. Replacement of the N terminal residues of M2-1 with that of the murine pneumovirus orthologue resulted in a complete abrogation of transcription processivity function in an inducible minigenome system.[14]

The interactions between M2-1 and the RNA have been somewhat unclear. Early on, it was suggested by Mason *et al.* that M2-1 interacted with P by using recombinant proteins and affinity chromatography.[15] However, this is in contrast to the direct interactions between different RNA species and M2-1 described earlier.[11,13] More recently, the work of Tran *et al.* used recombinant M2-1 to show that the C terminal region from residues 59 to 179 were the site of interaction with RNA and P, and to imply that RNA and P might compete with each other for binding to M2-1.[16] More importantly, this paper introduced a new possible function for the N terminus – as a homo-oligomerization domain.

As to how M2 interacts with the rest of the viral components in an assembled virion, there is evidence of a few interaction partners. Early on, the work of Mills *et al.* used immunofluorescent staining of inclusion bodies to show that not only did N and P localize to them, but M did as well.[17] The same research group went on to show that M and M2-1 colocalize in cells in wild type and plasmid derived systems.[18] It might also be possible that the M2-1 binds to one of the cytoplasmic tails of the glycoproteins. Imaging the virus at high resolution will help to understand the spatial relationship between M2-1, gRNA, and VPs in their native state, as opposed to other *in vitro* assays.

Imaging purified RSV virions using cryo-ET

We began by examining sucrose cushion purified RSV virions on grids using cryo-ET. In order to assess the general morphology of RSV purified from Hep-2 cell culture supernatant, 146 tomograms of viral particles were analyzed. In agreement with Liljeroos *et al*.[4], three morphological variants were observed in the purified viral samples: asymmetric, filamentous, and spherical (**Fig. 5.1**). Each particle picture demonstrates the characteristic glycol protein spikes along the envelope as well as a dense RNP that can be seen either isolated in the center of the virion (like in **Fig. 5.1A**), closely following the envelope (like in **Fig. 5.1C**), or arranged in a fashion that is in between these two extremes.

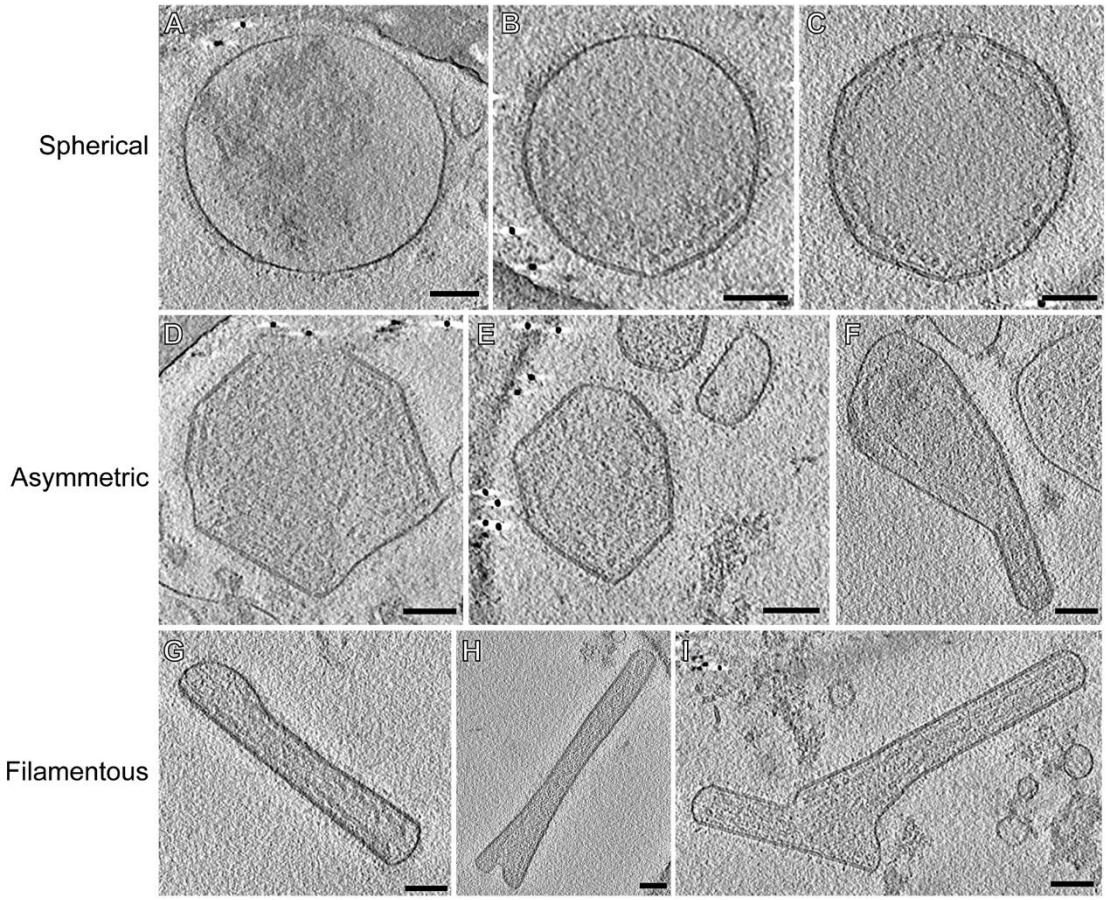

Figure 5.1 Basic morphological characterization of the three RSV morphologies. Representative particles of the three morphology categories found in the RSV sample: spherical (A-C), asymmetric (D-F) and filamentous (G-I). Common structural features present in the 3D reconstructions of all RSV morphologies include the surface glycoproteins, the viral membrane, the matrix protein layer, and the RNP. Images are 7.5 nm central slices from tomographic reconstructions. Scale bars 100 nm.

Returning to the question of M2-1's localization to the viral filaments from earlier, we acquired tomograms using Zernike phase contrast (ZPC)[19,20]. In the raw tomograms of RSV particles, we observed a regularly spaced density localized between the M protein layer and the RNP (data not shown). However, we were unable to resolve additional details regarding its structure or orientation using conventional defocus phase contrast cryo-ET. However, from the ZPC cryo-ET data, we observed small individual densities between the M layer and the RNP (**Fig. 5.2A**). The densities were ~12 nm from the membrane (**Fig. 5.2A**), which corresponded to the M2-1 density present in the linear profiles from the conventional cryo-ET data (data not shown). The discrete M2-1 masses maintained a regular spacing between each other of 12.6 (±2.1) nm (**Fig. 5.2B**). When taken together with the colocalization, PLA, and dSTORM data of isolated filamentous virions (as opposed to colocalization data in cells collected by another group[4]), we are reasonably certain that these regularly spaced puncta represent M2-1.

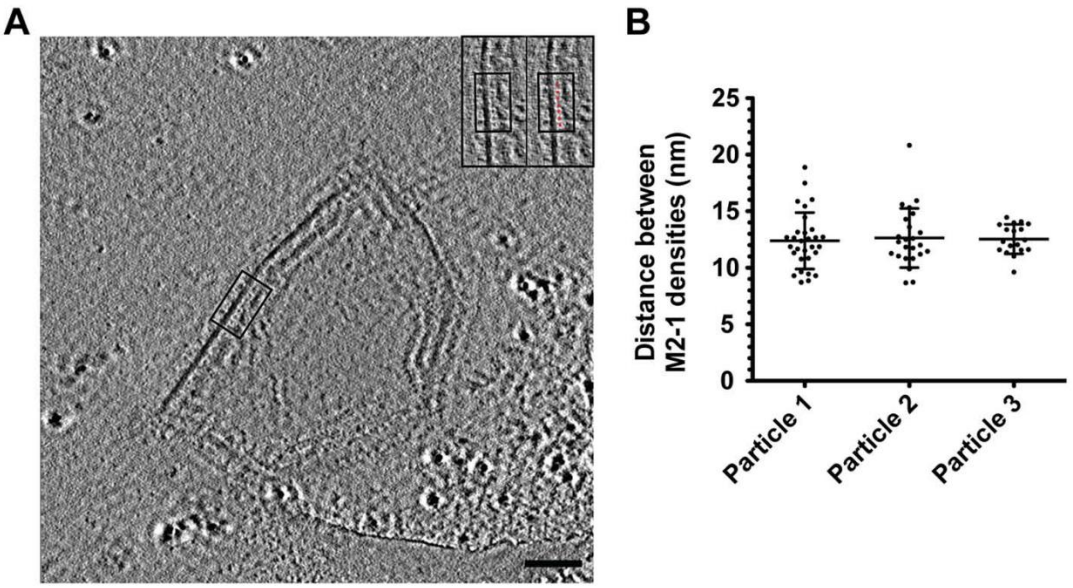

Figure 5.2 Spacing of M2-1 in RSV viral particles collected using ZPC cryo-ET. (A) 7.64 nm slice from a tomographic reconstruction of an RSV viral particle used for measuring M2-1 spacing. Boxed region highlights the location of M2-1 densities in the slice. The inset is a magnified view of the boxed region; red dots mark the M2-1 densities. Scale bar 100 nm. (B) Graph of the distances measured between M2-1 densities in three RSV viral particles. The mean and standard deviation are marked.

Labeling the surface proteins of RSV

After showing that we could perform cryo-ET on the isolated virions, we then set out to demonstrate that we could label them. We imaged virions that were extending from infected cells using both conventional TEM (**Fig. 5.3**) and cryo-ET (**Fig. 5.4**), immunolabeling the F protein with a 6 nm gold conjugated antibody, to determine the distribution of F proteins on the surface and their relation to other viral structural proteins. In TEM (**Fig. 5.3**), we observed many viral filaments, or sections of viral filaments, extending from the cell with typical length and width as has been previously reported.[3] Although individual glycoproteins are not completely visible, it is clear that there is F protein in a varied distribution along the outside of the filament. Upon examination of the 3D volumes in cryo-ET, the immunolabeled F glycoproteins was easily determined along filamentous virions extending outward from an infected cell (**Fig. 5.4**). The arrangement of the F glycoprotein along viral filaments was consistent with what has been reported previously.[4] The matrix protein and ribonucleoprotein (RNP) complex were also resolved along the viral membranes in close proximity to the glycoproteins.

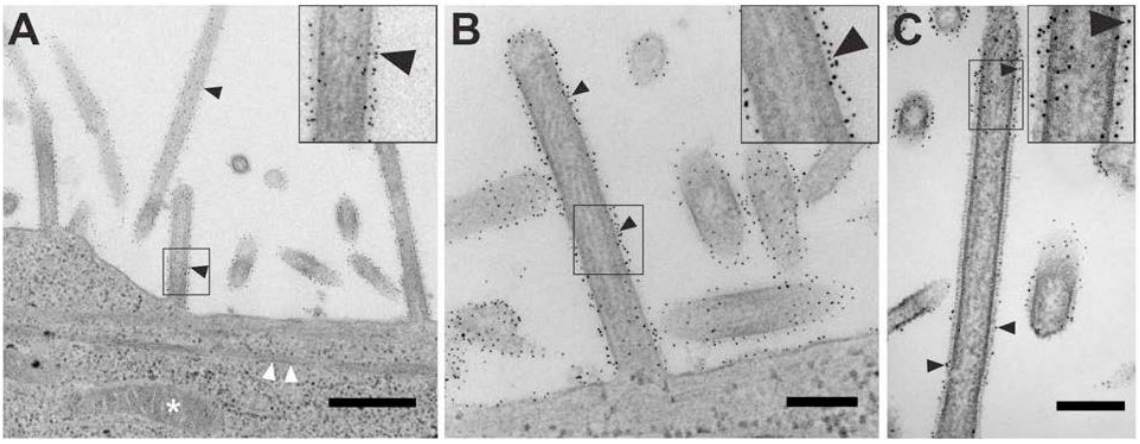

Figure 5.3. Conventional TEM of RSV with the F glycoprotein native immunolabeled. (A-C) black arrowheads point to immunogold labeling along viral filaments both at assembly sites and released RSV filaments. (A) White arrowheads note actin filaments and white asterisk point to mitochondrion. (B) Assembling viral filament extended from the plasma membrane. (C) Intermediate magnification image of filamentous RSV virion with immunogold labeling of the F glycoproteins. Inset in A is 3X while B and C are 2X. Scale bars (A) 500 nm and (B and C) 200 nm.

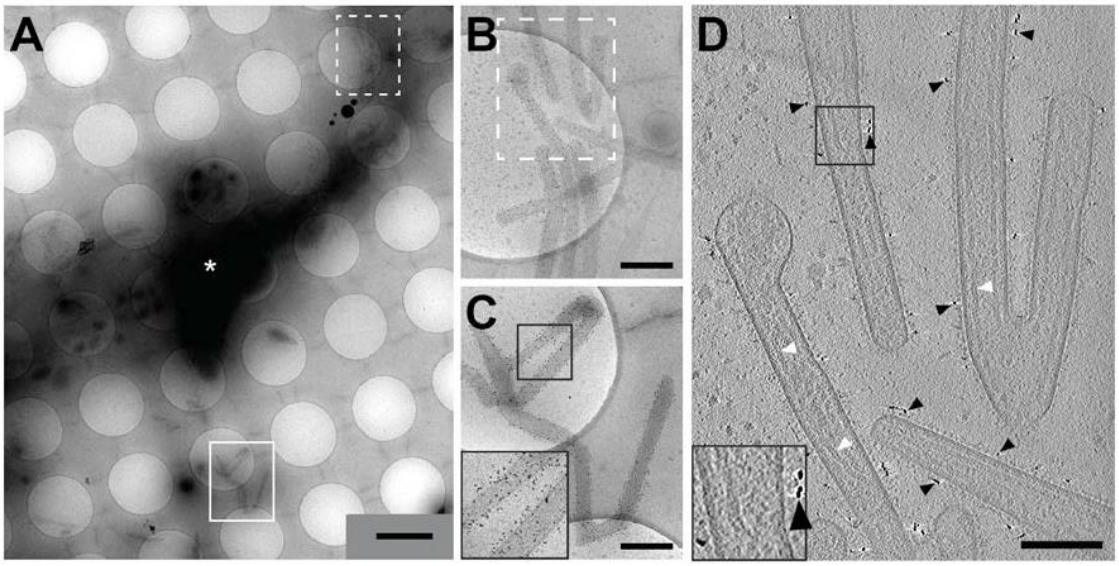

Figure 5.4 Cryo-TEM and Cryo-ET of RSV infected HeLa cells with the RSV Fusion glycoprotein immunolabeled. (A) Low magnification montage of released, filamentous RSV particles and a HeLa cell extension (white asterisk). (B and C) Higher magnification views of montage A highlighting immunolabeling of RSV F along the viral filaments. B and C are from dashed box (B) and solid box (C) from A, respectively. (D) Slice (7.64 nm) from the 3D reconstruction of the area from B (dashed box) illustrating RSV filaments with surface glycoproteins and immunogold (black arrowheads). Note the RNP in some of the virions (white arrowheads). Insets in C and D (black boxes) are 2X. Gold fiducial markers 20 nm in diameter were added to the sample and used as image alignment aids during the 3D tomographic reconstruction process. Scale bars 2 μm (A), 500 nm (B and C), 200 nm (D).

Discussion and conclusion

We have demonstrated the ability to image isolated virions in cryo-ET and have provided evidence to suggest that M2-1 is present in a discontinuous, but periodic layer in between a layer of M and the RNP (at least where the RNP is connected). Given the small spacing of 12.6 (±2.1) nm, it is no surprise that even dSTORM (lateral resolution ~20-35 nm) would be unable to resolve individual M2-1 puncta. This result would seem to agree with the findings in a recent crystal structure of M2-1[21], in which they do not find evidence of an M2-1-to-M2-1 interaction domain. If it were possible to image the virions at high enough resolution to fit the crystal structure, it is likely to support the conclusion that M2-1 exists as a tetramer. Insights into this structure might possibly shed light onto the structure and function of orthologous proteins in the pneumovirus genera and of the VP30 protein of Ebola, which similarly functions as a transcription processivity factor and possibly binds the RNA itself.[22] It has been suggested that VP30 and Ebola are "structurally" similar despite low sequence homology.[23]

As for whether or not M2-1 is bound to the RNA directly or mediated through P, it might be possible to address this question in the future. One experiment that could be done would be to introduce antisense oligonucleotides to block the possible interaction between M2-1 and the RNA using SLO permeabilization, and then quantify a decrease in the length of RNP that is adjacent to the M-layer using cryo-EM. This could also be used as a metric to determine if overexpression of a mutated P disrupts the putative M2-1/P interaction, perhaps both within infected cells and within a minigenome system. Having a labeled RNA during the course of these experiments would provide a means a quickly assessing the affects via fluorescence, using cryo-ET to provide close-up confirmation.

There are many implications of this work regarding the assembly of the RSV virion. First, the fact that M2-1 is observed in discrete puncta in between the M and RNA layers seems to support the work of Li *et al.*, who call the M2-1 an adaptor between the M and the RNA.[18] However, whether or not M is then connected to the G cytoplasmic tail, as was suggested by Ghildyal *et al.*[24] remains to be seen. There has also recently been interest in the F cytoplasmic tail, which has been shown by Oomens *et al.* and Baviskar *et al.* to target F to the perimeter of inclusion bodies and assemble into filaments, respectively.[25,26]

The possible interactions between M2-1, M, and the cytoplasmic tails could provide insight into the cellular entry of RSV and other members of *Pneumovirinae*. Unlike viruses of *Paramyxoviridae*, in which the fusion protein is triggered by the binding of the attachment glycoprotein, the RSV F seems capable of functioning without the presence of G.[27] How conformational changes in either the F or G might lead to the release of M2-1, assuming it is an adaptor to the RNA, during viral entry remain to be seen.

We have also demonstrated that we are capable of labeling the virus, at least externally. It is a bit surprising that the labeling was somewhat sparse, although that might be due to steric hindrance of the primary/secondary antibodies. At least the primary antibody (palivizumab) should bind to both the pre-fusion and post fusion conformations of the F protein.[28] It would be interesting to repeat this study with a primary labeled antibody and/or smaller label and/or pre-fusion specific F antibody, as the structure of the F trimer confined to the pre-fusion state by an antibody is known.

Clearly, the pieces are in place for examining RSV except for an electron-dense version of the RNA probe. Ultimately a better understanding of the spatial relationships between the genomic RNA and the viral proteins could lead to targets for novel small molecule inhibitors.

Materials and Methods

For isolated virus propagation, the A2 strain of RSV was grown in HEp-2 cells under batch conditions and purified to a viral particle count of ~6 x10^9 viral particles/ml. Aliquots of the purified virus suspended in a 10 mM Tris, 150 mM NaCl, 1 mM EDTA, pH 7.5 buffer were acquired from Advanced Biotechnologies Inc. (Columbia, MD).

For cryo-ET preparation and data collection on isolated virions, the purified virus suspension was flash-frozen (plunge frozen) onto glow-discharged Quantifoil grids (Quantifoil Micro Tools GmbH, Jena, Germany) in liquid ethane by using either a Vitrobot Mark III or Mark IV system (FEI, Hillsboro, OR). 10 nm BSA-treated or protein-A-treated colloidal gold was added to the sample and applied to the grid as a fiduciary marker. Cryo-ET data collection was performed by using two microscopes: a JEOL JEM-2200FS 200 kV FEG-TEM (JEOL Ltd., Japan) with a Zernike-style phase plate system, an in-column Omega-style energy filter (slit width: 20 eV), and a 4k x 4k Gatan Ultrascan CCD camera (Gatan, Pleasanton, CA) at the Emory University Robert P. Apkarian Integrated Electron Microscopy Core or an FEI Titan Krios 300 kV FEG-TEM (FEI, Hillsboro, OR) with a GIF-2002 energy filter (slit width: 20 eV) coupled to a 2k x 2k MultiScan^{TM} Gatan Ultrascan CCD camera at the Rocky Mountain Laboratories, DIR, NIAID. Images were acquired with pixel sizes of 0.764 nm and 0.45 nm, respectively, on the specimen. A total electron dose of ~120 e^-/A^2 was fractionated over individual tilt series ranging from -62° to +62°. Data were collected at a defocus ranging between 4 and 6 μm under focus. Tilt series images were taken automatically with 2 tilt increments by using either SerialEM [29] or Xplore3D the FEI automated Tomography data collection software.

For imaging processing analysis of isolated virions, three dimensional (3D) reconstructions (tomograms) were generated using IMOD[30], and the data were binned twofold during the process. The tomograms were further binned and denoised by either bilateral filtering or non-linear anisotropic diffusion as implemented in the Bsoft suite.[31] Final analyses of the tomograms were with a voxel size range of 1.5 nm to 0.9 nm. Direct volume rendering, z-slice progressions, and quantitative rendering were done with Amira 5.4.1 (Visualization Sciences Group). Linear profiles were generated using ImageJ software package.[32] Graphical analyses were performed using Prism (GraphPad Software), while for statistical analysis Prism, StatPlus (www.analystsoft.com) and Microsoft Excel were used.

For immunolabeling RSV F in infected cells, HeLa and HEp-2 cells (ATCC CCL-2 and CCL-23, respectively) were maintained in DMEM growth medium with 4.5 g/L D-glucose (Lonza, Switzerland), 4 mM L-glutamine (BioWhittaker), 10% fetal bovine serum (FBS, Sigma-Aldrich, St. Louis, MO), and 1% Penicillin Streptomycin (Sigma-Aldrich). Cells were grown in an incubator at 37°C with 5% CO_2. For RSV F glycoprotein immunogold labeling, 100,000 – 150,000 HEp-2 cells or HeLa cells were seeded on pre-sterilized, pre-incubated (with complete medium) Aclar disks or gold R2/1 Quantifoil TEM grids in MatTek dishes (MatTek Corp., MA) 4-8 hours prior to infection.

Cells for immunogold labeling were inoculated with an MOI of 10 with RSV in serum free media. Complete growth media was added after 1 hour. Infected cells were incubated at 37°C for 24 hours. Palivizumab was then added directly into the medium at 5 µg/mL and cells were allowed to incubate for 1.5 hours at 37°C, during which time the culture plates and MatTek dishes were shaken gently to facilitate antibody binding. After

primary antibody incubation, the cells were gently washed with complete medium 4 times for 30 seconds each time. The secondary antibodies, 6 nm gold-conjugated goat anti-human IgG or protein G, were then added to the medium directly at 1:20 dilution of the original stock solutions (10 - 20 μg/mL) and allowed to incubate for 1.5 hours. Washes were repeated as described above after secondary antibody incubation. Cells on Aclar disks were washed twice with PBS for 5-seconds and then fixed with 2.5% glutaraldehyde in 0.1 M phosphate buffer (pH 7.4) for conventional transmission electron microscopy examination. Cells on the gold Quantifoil TEM grids were plunge frozen immediately after the final wash with culture medium.

For conventional TEM preparation, fixed cells on Aclar disks were washed twice with 0.1 M phosphate buffer (pH 7.4) after overnight fixation with 2.5% glutaraldehyde in the same buffer. Cells were then post-fixed with 1% osmium tetroxide in 0.1 M phosphate buffer (pH 7.4) for 1 hour. Following graded ethanol dehydration, cells were infiltrated, embedded and polymerized in Eponate 12 resin (Ted Pella Inc., Redding, CA).

Ultrathin sections were cut using a Leica Ultracut S ultramicrotome at a thickness of 70 nm. Sections were then stained with 5% uranyl acetate and 2% lead citrate and imaged on a Hitachi H-7500 transmission electron microscope (TEM, Hitachi High-Tech, Japan) equipped with a SIA L12C 16 Megapixel CCD camera (SIA, Duluth, GA) or a JEOL JEM-1400 TEM (JEOL Ltd., Japan) equipped with a Gatan US1000 2k x 2k CCD camera (Gatan, Pleasanton, CA).

Cryo-TEM images for immunolabeled gold were acquired and processed in a similar manner as isolated virions.

References

1.Norrby, E., Marusyk, H. & Orvell, C. Morphogenesis of respiratory syncytial virus in a green monkey kidney cell line (Vero). *J. Virol.* **6,** 237-42 (1970).

2.Bächi, T. & Howe, C. Morphogenesis and ultrastructure of respiratory syncytial virus. *J. Virol.* **12,** 1173-80 (1973).

3.Roberts, S. R., Compans, R. W. & Wertz, G. W. Respiratory syncytial virus matures at the apical surfaces of polarized epithelial cells. *J. Virol.* **69,** 2667-73 (1995).

4.Liljeroos, L., Krzyzaniak, M. A., Helenius, A. & Butcher, S. J. Architecture of respiratory syncytial virus revealed by electron cryotomography. *Proc. Natl. Acad. Sci. U.S.A.* **110,** 11133-8 (2013).

5.Collins, P. L., Fearns, R. & Graham, B. S. Respiratory syncytial virus: virology, reverse genetics, and pathogenesis of disease. *Current Topics in Microbiology and Immunology* **372,** 3-38 (2013).

6.Ueba, O. Respiratory syncytial virus. I. Concentration and purification of the infectious virus. *Acta Med. Okayama* **32,** 265-72 (1978).

7.Peeples, M. & Levine, S. Respiratory syncytial virus polypeptides: their location in the virion. *Virology* **95,** 137-45 (1979).

8.García, J., García-Barreno, B., Vivo, A. & Melero, J. A. Cytoplasmic inclusions of respiratory syncytial virus-infected cells: formation of inclusion bodies in transfected cells that coexpress the nucleoprotein, the phosphoprotein, and the 22K protein. *Virology* **195,** 243-7 (1993).

9.Collins, P. L., Hill, M. G., Cristina, J. & Grosfeld, H. Transcription elongation factor of respiratory syncytial virus, a nonsegmented negative-strand RNA virus. *Proceedings of the National Academy of Sciences* **93,** 81 (1996).

10.Bermingham, A. & Collins, P. L. The M2-2 protein of human respiratory syncytial virus is a regulatory factor involved in the balance between RNA replication and transcription. *Proc. Natl. Acad. Sci. U.S.A.* **96,** 11259-64 (1999).

11.Hardy, R. W. & Wertz, G. W. The product of the respiratory syncytial virus M2 gene ORF1 enhances readthrough of intergenic junctions during viral transcription. *J. Virol.* **72,** 520-6 (1998).

12.Cartee, T. L. & Wertz, G. W. Respiratory syncytial virus M2-1 protein requires phosphorylation for efficient function and binds viral RNA during infection. *J. Virol.* **75,** 12188-97 (2001).

13.Cuesta, I., Geng, X., Asenjo, A. & Villanueva, N. Structural phosphoprotein M2-1 of the human respiratory syncytial virus is an RNA binding protein. *J. Virol.* **74,** 9858-67 (2000).

14.Zhou, H., Cheng, X. & Jin, H. Identification of amino acids that are critical to the processivity function of respiratory syncytial virus M2-1 protein. *J. Virol.* **77,** 5046-53 (2003).

15.Mason, S. W., Aberg, E., Lawetz, C. & DeLong, R. Interaction between human respiratory syncytial virus (RSV) M2-1 and P proteins is required for reconstitution of M2-1-dependent RSV minigenome activity. *Journal of …* (2003).

16.Tran, T. *et al.* The respiratory syncytial virus M2-1 protein forms tetramers and interacts with RNA and P in a competitive manner. *J. Virol.* **83,** 6363-74 (2009).

17.Mills, J. *et al.* Respiratory syncytial virus matrix protein associates with nucleocapsids in infected cells. *J. Gen. Virol.* **83,** 753-7 (2002).

18.Li, D. *et al.* Association of respiratory syncytial virus M protein with viral nucleocapsids is mediated by the M2-1 protein. *J. Virol.* **82,** 8863-70 (2008).

19.Danev, R., Kanamaru, S., Marko, M. & Nagayama, K. Zernike phase contrast cryo-electron tomography. *J. Struct. Biol.* **171,** 174-81 (2010).

20.Murata, K. *et al.* Zernike phase contrast cryo-electron microscopy and tomography for structure determination at nanometer and subnanometer resolutions. *Structure* **18,** 903-12 (2010).

21.Tanner, S. J. *et al.* Crystal structure of the essential transcription antiterminator M2-1 protein of human respiratory syncytial virus and implications of its phosphorylation. *Proc. Natl. Acad. Sci. U.S.A.* **111,** 1580-5 (2014).

22.John, S. P. *et al.* Ebola virus VP30 is an RNA binding protein. *J. Virol.* **81,** 8967-76 (2007).

23.Blondot, M. *et al.* Structure and functional analysis of the RNA- and viral phosphoprotein-binding domain of respiratory syncytial virus M2-1 protein. *PLoS Pathog.* **8,** e1002734 (2012).

24.Ghildyal, R. *et al.* Interaction between the respiratory syncytial virus G glycoprotein cytoplasmic domain and the matrix protein. *J. Gen. Virol.* **86,** 1879-84 (2005).

25.Baviskar, P. S., Hotard, A. L., Moore, M. L. & Oomens, A. G. P. The respiratory syncytial virus fusion protein targets to the perimeter of inclusion bodies and facilitates filament formation by a cytoplasmic tail-dependent mechanism. *J. Virol.* **87,** 10730-41 (2013).

26.Oomens, A. G. P., Bevis, K. P. & Wertz, G. W. The cytoplasmic tail of the human respiratory syncytial virus F protein plays critical roles in cellular localization of the F protein and infectious progeny production. *J. Virol.* **80,** 10465-77 (2006).

27.Jardetzky, T. S. & Lamb, R. A. Activation of paramyxovirus membrane fusion and virus entry. *Current Opinion in Virology* **5,** 24-33 (2014).

28.McLellan, J. S., Yang, Y., Graham, B. S. & Kwong, P. D. Structure of respiratory syncytial virus fusion glycoprotein in the postfusion conformation reveals preservation of neutralizing epitopes. *J. Virol.* **85,** 7788-96 (2011).

29.Mastronarde, D. N. Automated electron microscope tomography using robust prediction of specimen movements. *J. Struct. Biol.* **152,** 36-51 (2005).

30.Kremer, J. R., Mastronarde, D. N. & McIntosh, J. R. Computer visualization of three-dimensional image data using IMOD. *J. Struct. Biol.* **116,** 71-6 (1996).

31.Heymann, J. B. Bsoft: image and molecular processing in electron microscopy. *J. Struct. Biol.* **133,** 156-69 (2001).

32.Schneider, C. A., Rasband, W. S. & Eliceiri, K. W. NIH Image to ImageJ: 25 years of image analysis. *Nat. Methods* **9,** 671-5 (2012).

CHAPTER 6

RNA PROBES FOR ULTRASTRUCTURAL IMAGING

This work is currently unpublished; all images taken by EA with the exception of Figure 6.5.

Background

RNAs by themselves do not generate sufficient contrast in TEM, necessitating electron dense labeling for imaging. The gold standard for RNA localization has been electron microscopy in situ hybridization (EM ISH), which uses digoxigenin or biotin conjugated antisense oligonucleotides.1 This can be done in a pre-resin embedding, post-resin emedding, or cryo-sectioning. One of the only examples of EM-ISH was the work of Bassell *et al.*, in which they used the technique to analyze the distribution of the poly(A) mRNAs attached to different cytoskeletal elements.2. They used fibroblasts in this example of pre-embedding hybridization. Another example of the technique was provided by Li *et al*, in which the authors imaged a small RNA which is part of the RNase MRP endonuclease complex and localizes within the mitochondria.3 They used mouse cardiomyocytes in an example of cryo-sectioning EM-ISH. However, EM-ISH is not without drawbacks. Most prominent among them is the harshness of the permeability (for pre-embedding) and denaturants (for all variations of EM ISH) on the cellular ultrastructure. Imaging the virus and cells in their native, hydrated state is crucial towards understanding how the virus is assembled and where the gRNA is localized. For this reason, we turned to cryo-EM and cryo-ET. Our live cell probe delivery method using streptolysin-O avoids the use of fixatives, allowing the virus or cells to be plunge frozen instantly, preserving its ultrastructure.

Our original design for an electron dense RNA probe consisted of one or more 1.4 nm gold nanoclusters (Nanogold) covalently bound to either the neutravidin core or the oligonucleotide arms of our existing RNA probe. We chose the 1.4 nm Nanogold because it was the smallest gold particle that has been detected by cryo-EM (data not shown) and because it has a single reactive site on it. As an initial test, we attempted to use the commercially available 1.4 nm gold nanocluster streptavidin conjugate in making the probes.

We next attempted to image the probes using thin section TEM after silver enhancement. We tried, in order, the following model systems: RSV infected cells with RSV probes, noninfected cells with polyA probes, noninfected cells with polyA peptide nucleic acid (PNA) probes, noninfected cells with polyA probes and polyA PNA probes under oxidative stress. Unfortunately, in all of these cases, the density of RNA was not sufficient for us to comfortably proceed to cryo-EM, possibly due to undersampling by thin sectioning, linker length of the PNA probes preventing delivery, etc. It should be noted that we also attempted immunogold staining of RNA binding proteins (G3BP) and were unsuccessful at sufficiently detecting this protein in thin sections. We next decided to forego TEM, studies and replace them with darkfield imaging of silver enhanced nanogold and to use a model system that would purposely localize many RNA molecules within a small region.

The model system we settled on were cells transfected with probes pre-hybridized to a synthetic mRNA encoding GFP and delivered to the cell using a cationic lipid transfection agent (which we will refer to as an RNA lipoplex). Previous studies by Jonathan Kirschman had shown that mRNA could be “pre-labeled” with RNA probes and delivered to cells in a variety of ways. When cationic lipids (Lipofectamine) are used as a delivery method, it was observed that the pre-labeled mRNAs tended to form large, bright puncta greater than 100 nm in size. Moreover, using silver enhancement and darkfield microscopy, we could test the delivery protocol both on glass and in cells,

ensuring that the puncta contained gold nanoclusters without having to process samples for TEM.

In addition to the darkfield, we also had the opportunity of using a new cryo-fluorescence widefield microscope for correlative FLM/cryo-EM imaging. This system was instrumental in helping us verify what the RNA lipoplex puncta would look like in cryo-EM. Data from the demo system is briefly featured in Figure 6.5.

The field of non-viral mRNA delivery has been growing due to its potential applications in cancer therapeutics, protein replacements, and infectious disease vaccines.[4] Cationic lipids, polymers, and peptides have been a popular choice for delivering nucleic acids due to their lower immunogenicity when compared with viral methods.[5] While several specific mechanisms for cytoplasmic entry have been proposed, one popular hypothesis is that nucleic acid lipoplexes enter the cell through endocytosis, followed by endosomal disruption.[6] Several electron microscopy studies have attempted to understand the ultrastructure of DNA lipoplexes and their entry pathway into cells, including negative stain TEM,[7] thin-section TEM,[7,8] freeze-fracture TEM,[9-11] and more recently cryo-EM.[10,12-15] These DNA lipoplexes typically manifest in images as multilamellar structures. There has been comparatively less research on the ultrastructure of mRNA lipoplexes.

In order to pursue the imaging of RNA lipoplexes, we began synthesizing our own neutravidin-gold nanocluster conjugates for two reasons, first, in order to add multiple golds per neutravidin, second, because we observed that the BSA stabilizer within the commercial streptavidin-gold nanocluster conjugate decreased the transfection efficiency when using cationic lipids; using SLO as a delivery method did not seem to be adversely affected. This was likely due to the charge of BSA and it's possible binding to Lipofectamine, preventing for formation of adequate mRNA/Lipofectamine complexes. After size exclusion HPLC, the conjugates were allowed to bind to biotinylated, fluorescently labeled oligos to make the RNA probes. After filter through a membrane

filter, the probes were then hybridized with the mRNA, membrane filtered again, and complexed with the cationic lipid before being added to cells.

Imaging probe labeled RNA lipoplexes

We began by examining our probe labeled mRNA lipoplexes that we had isolated on fibronectin coated coverglass. The lipoplexes made with gold nanocluster labeled probes appear to be of similar size and number as their unlabeled counterparts in fluorescence (**Fig. 6.1a**). In order to verify the presence of gold in the lipoplexes, we amplified the gold nanoclusters by reductive silver enhancement and imaged them using fluorescence and darkfield (**Fig. 6.1b**). The gold nanocluster labeled probes generated a strong darkfield signal that touches and surrounds the fluorescent puncta of the lipoplexes, as opposed to the non-gold containing control. Clearly, the gold-labeled probe lipoplexes contained sufficient seeds to rapidly generate large silver particles.

To take our examination a step further, we examined what effect changing either the amount of mRNA or the volume of cationic lipid had on the lipoplex granules. We found that decreasing the volume of the cationic lipid for a constant amount of RNA decreases the number of the puncta (**Fig. 6.2a**), possibly indicating less complexed mRNA. It should be noted that at this particular decreased volume of Lipofectamine (0.4uL), the transfection efficiency for this RNA lipoplex in cells at 24 hr post transfection as measured by GFP expression drops well below 50% (data not shown), lending support to the idea that less mRNA are complexed and therefore fewer mRNAs efficiently delivered. On the other hand, we found that decreasing the amount of mRNA for a given amount of lipofectamine decreases the size of the granules (**Fig. 6.2b**), possibly indicating fewer mRNA per granule. The transfection efficiency for this RNA

lipoplex (100 ng mRNA) in cells at 24 hr post transfection is similar to the increased case (500 ng mRNA), but the GFP signal intensity is lower.

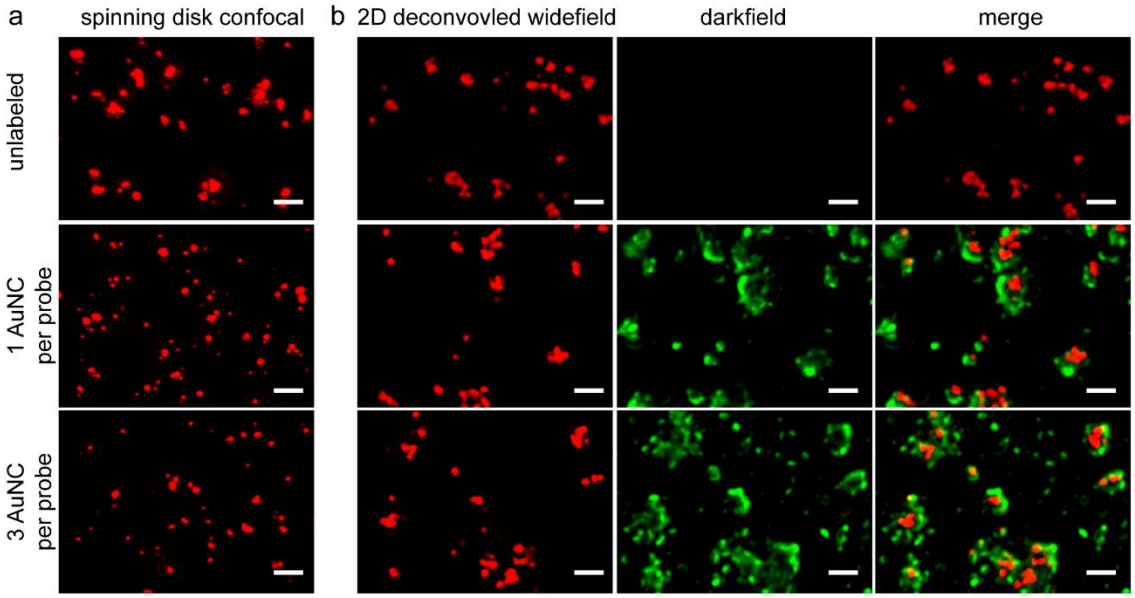

Figure 6.1 RNA-Lipoplexes on Glass. (a) Spinning disk confocal images of unlabeled RNA probes, 1 gold nanocluster (AuNC) labeled probes, and 3 gold nanocluster probes, all bound to an mRNA and in a lipoplex. (b) Widefield 2D deconvolved images (red) of unlabeled and labeled probes bound to mRNA and in a lipoplex on glass after silver enhancement (left column); darkfield images (green) after silver enhancement (middle column); and merged image of darkfield and widefield images (right column). Single-plane images shown. Scale bar 5 μm.

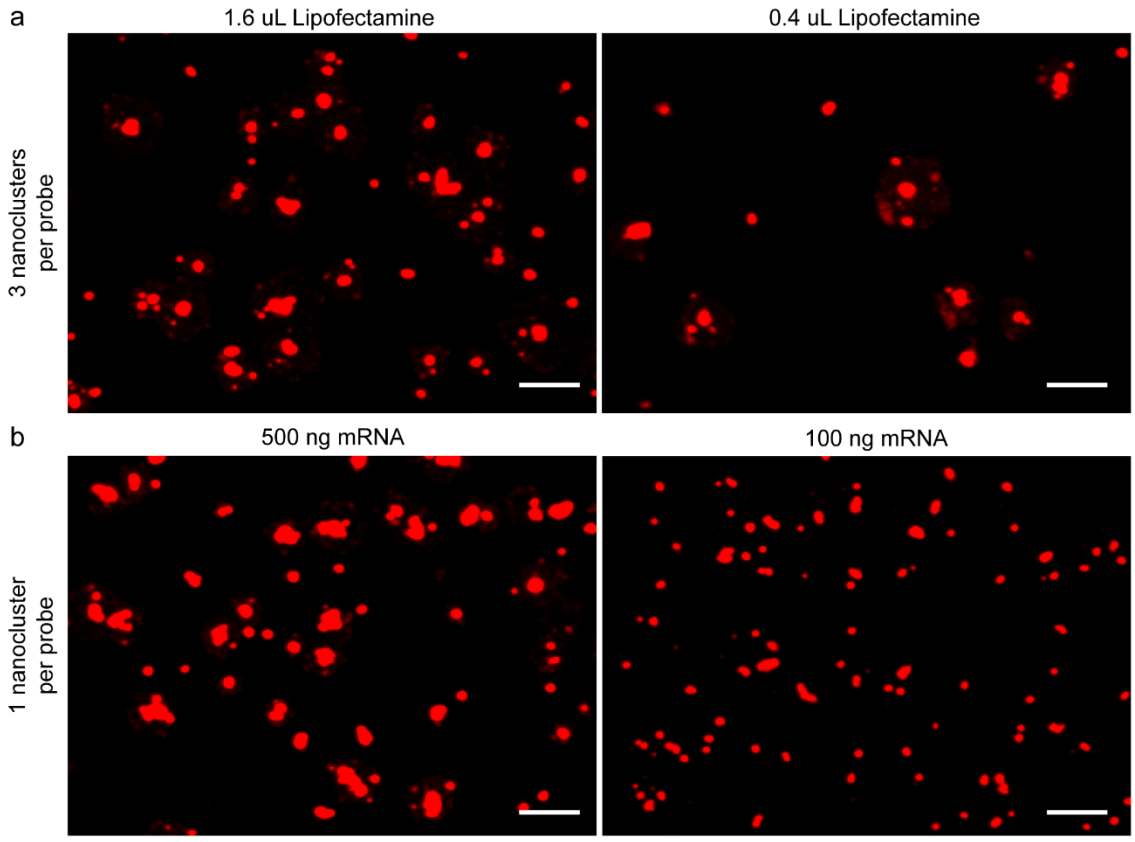

Figure 6.2 Influence of cationic lipid and mRNA concentrations on lipoplexes on glass. (a) Images showing 3 gold nanocluster-labeled probes bound to mRNA in a lipoplex made with two different volumes of Lipofectamine. (b) Images showing 1 gold nanocluster-labeled probes bound to two different amounts of mRNA in a lipoplex. Single-plane, spinning disk confocal images shown. Scale bar 5 μm.

We also studied RNA lipoplexes entering cells at an early timepoint. RNA lipoplexes made with and without gold nanocluster labeled probes enter the cell cytoplasm at 5 hr post transfection (**Fig. 6.3a**). Upon examination of cells in widefield fluorescence and darkfield microscopy, it is evident that the lipoplexes containing gold nanocluster labeled probes produce puncta in darkfield, and that those darkfield puncta colocalize with the fluorescent signal of the lipoplexes (**Fig. 6.3b**). The non-gold labeled lipoplexes produce little to no signal above background. It appeared that the gold nanocluster labeling does not inhibit the lipoplexes from entering the cell.

We also examined the effect of gold nanocluster labeling on the translation of mRNA into GFP. We observed that gold nanocluster labeling does not affect the transfection efficiency nor the translation efficiency of the mRNA within the lipoplex (**Fig. 6.4**). This suggests that gold nanocluster labeling does not adversely affect the function, and likewise the structure, of the RNA lipoplexes.

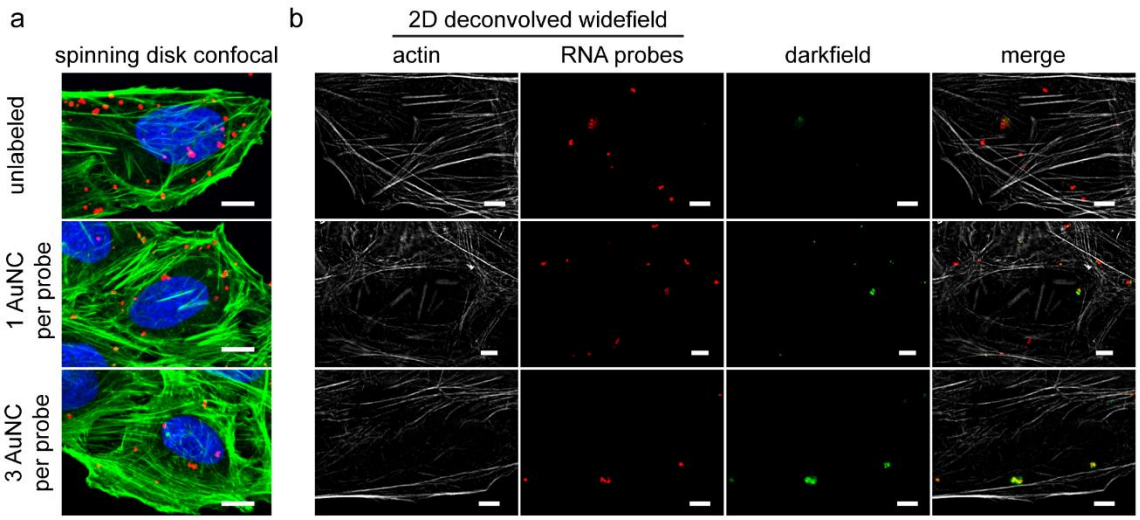

Figure 6.3 RNA lipoplexes in cells. (a) Spinning disk confocal images showing U2OS cell transfected with unlabeled, 1 gold nanocluster labeled, and 3 gold nanocluster labeled RNA probes bound to mRNA and in a lipoplex. Taken at 5 hr post transfection. Green is actin, red is lipoplex, and blue is nucleus. (b) 2D deconvolved widefield images showing cellular actin (gray, first column from left), RNA lipoplex (red, second column from left), darkfield (green, third column from left), and merge of all images for aforementioned probe labelings (rows). Single plane images shown. Scale bar 10 μm.

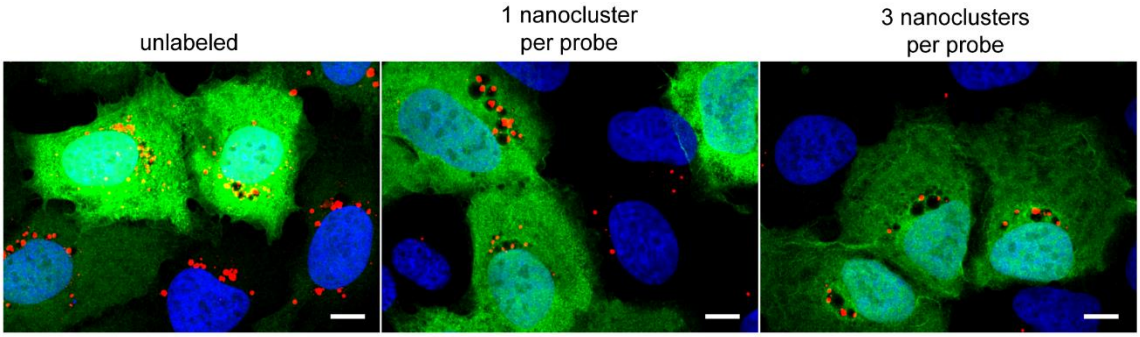

Figure 6.4 Transfection efficiency of RNA lipoplexes. RNA lipoplexes made with unlabeled (left image), 1 gold-nanocluster labeled (middle image), or 3 gold nanocluster-labeled RNA probes (right image) were delivered to U2OS cells and allowed to incubate for 24 hours before being fixed and immunostained for GFP. RNA probes in red, GFP in green, cell nuclei in blue. Extended focus spinning disk confocal images. Scale bar 10 μm.

To date, we were able to conduct one round of correlative cryo-fluorescence/cryo-EM on the RNA lipoplexes in U2OS cells. U2OS cells were used because they are thin, ~ 1 um, facilitating imaging throughout the cells via cryoEM. U2OS cells were grown on finder grids, transfected with RNA lipoplexes, allowed to incubate for 5 hr post transfection, and then immediately plunge frozen. Cells were imaged in cryo-fluorescence to find suitable regions containing sufficient numbers of RNA lipoplexes (**Fig. 6.5A**). The regions were relocated in cryo-EM (**Fig. 6.5B**) and after magnification the structure identical to the RNA lipoplex fluorescent puncta could be identified (**Fig. 6.5C**). At high magnification, the RNA lipoplex ultrastructure is a semi-organized, multilamellar lipid structure (**Fig. 6.5D**). After images are captured as frames on a direct electron detection device and computationally aligned to remove beam-induced motion and image contrast enhancement, the 1.4 nm gold nanoclusters can be seen within the lipid layers (yellow arrows). This image provides unambiguous evidence that the RNA lipoplexes are labeled with gold nanoclusters.

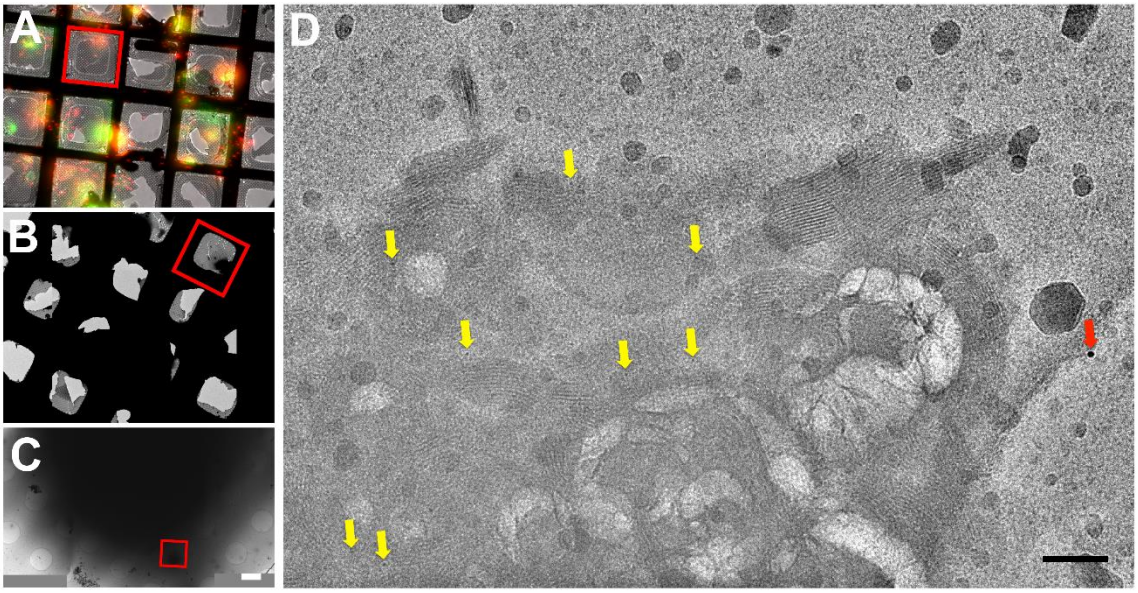

Figure 6.5 RNA lipoplexes in correlative cryo-fluorescence and cryo-EM. (A) Cryo-fluorescence image of finder grid showing low magnification of RNA lipoplexes (red) and cell cytoplasm (green). Red box denotes grid square that was correlated to TEM. Extended focus widefield image. (B) Low magnification image of grid in cryo-TEM, with red box that was indicated the same grid square as the one boxed in (A). (C) Medium magnification stitched image of boxed grid square shown in (A) and (B). Red boxed region in this case is magnified further in next panel. (D) High magnification imaged of RNA lipoplex puncta in cryo-EM. Red arrow indicates 10 nm fiducial gold nanoparticle. Yellow arrows indicate 1.4 nm gold nanocluster conjugated RNA probes. Scale bars indicate 2 μm and 100 nm for (C) and (D), respectively.

Discussion and conclusion

These experiments demonstrate that gold nanocluster labeling of RNA probes represent a means to accurately detect mRNAs within a lipoplex via cryoEM. Like the recent DNA lipoplex work from Bihan et al.[15], we found that mRNA in a lipoplex exists as a semi-organized, multilamellar structure. However, unlike DNA, our mRNA is already capped and polyadenylated, and therefore should not enter the nucleus. Also, since our probes are based on Watson-Crick base pairing as opposed to ionic interactions between DNA and surface aminated nanoparticles, are probes should prove to have greater specificity for long term tracking of the lipoplexes within the cell.

In addition, we found that the volume of cationic lipid influences the number of lipoplexes, whereas the amount of RNA influences the size. These findings agree with the work of Huebner *et al.*[13], which suggests that the nucleic acid (in their case linear DNA) is necessary to form multilamellar lipoplexes from unilamellar cationic lipids in solution. However, the exact point in the entry pathway at which smaller lipoplexes made from less mRNA might differ from larger ones (cellular entry, endocytosis, etc.) has yet to be determined. It would be simple matter of doing a timecourse experiment, perhaps with inhibitors of different endosomal components, to be able to paint out, along with fluorescence microscopy, the entry pathway of these RNA-lipoplexes.

With regard to the virus work, it would ultimately be useful to not only have the RNA delineated, but also some of the virus proteins. In this way, for instance, we could provide direct evidence of M2-1 binding to the genomic RNA. The viral surface proteins could be labeled easily enough, using antibodies conjugated to larger gold particles as we have already shown for the F protein. However, labeling the internal proteins presents a

bit more of challenge. It might be possible to produce and deliver either a Fab fragment or a single domain antibody attached to a small undecagold, nanogold, or gold nanoparticle, at least for those RSV proteins for which a suitable antibody exists. However, it would still be better if the proteins themselves could be expressed with a small affinity tag, which could then be targeted with a Fab/single domain antibody. Unfortunately, commonly used tags such as the glutathione *S*-transferase (GST tag) and SNAP-tag still require the addition of a ~20kDa tag protein onto the protein of interest. It is not likely that the smaller proteins of the RSV genome, such as M2-1, which are also on the order of ~20kDa would tolerate such modifications, but that would have to be determined experimentally. Smaller peptide tags, such as Flag, Myc, and His tags are much smaller in size, but still might change the surface charge of the protein in a significant fashion to prevent its proper function. Additionally, finding suitable antibodies with low background to these peptide tags can be challenging. Furthermore, oftentimes multiple copies of the peptide tag are added to the protein of interest, increasing the size.

Finally, we demonstrate that we are able to do correlative fluorescence and cryo-ET. While the fluorescence is quite helpful in finding regions of interest in cryo-ET, it would be interesting to attempt either correlative STED or correlative dSTORM with cryo-ET. This would serve to paint a more accurate picture of the sample and aiding the search for regions of interest.

This work establishes a method for investigating the ultrastructure of RNA lipoplexes and could lead to improvements in mRNA delivery to cells. However, since the work is not yet complete, several experiments will be performed in the near future. These experiments are listed in Table 6.1.

Experiment	Conditions	Expected Results
Cryo-ET imaging of RNA-lipoplexes on grids	• 1-3 nanoclusters per probe • 100-500ng RNA per lipoplex	3 gold nanocluster probes will be denser than 1 gold nanocluster probe; less RNA will lead to smaller lipoplexes; probes/RNA will be sandwiched in between lipid layers
Cryo-ET imaging of RNA-lipoplexes in cells	• 1-3 nanoclusters per probe • 100-500ng RNA per lipoplex	RNA-lipoplexes will be of same sizes to previous experiment, will be contained in endosomal compartments

Table 6.1 RNA-lipoplex experiments to be conducted in near future.

Materials and methods

For conjugation of gold nanoclusters to neutravidin, a 5X or 15X molar excess (for 1 gold nanoclusters/neutravidin and 3 gold nanoclusters/neutravidin, respectively) of sulfo-NHS ester reactive gold nanoclusters (Nanogold, Nanoprobes) was reconstituted according to the manufacturer's instructions. The Nanogold was then buffer exchanged into a 0.1M sodium bicarbonate (Sigma Aldrich) buffer (pH 8.1) by membrane filtration though a 3kDa filter (EMD) at 14,000 x g twice, the first time for 5 min and the second for 20 min. Neutravidin (Pierce), reconstituted according to the manufacturer's instructions, was added to the reactive gold nanoclusters, mixed by pipette, and allowed to incubate for at least 2 hr at room temperature. Afterwards, the nanocluster-neutravidin conjugate was purified by size exclusion chromatography on a Yarra SEC-2000 column (Phenomenex). The mobile phase was 0.1M phosphate buffer pH 7.2 and the flow rate was 0.35mL/min. The peak (in both the 280 nm absorbance and 370 nm absorbance channels) between 5 min and 7 min was collected and concentrated in a 10 kDa filter (EMD Millipore). The protein concentration and degree of labeling was assessed by UV-Vis absorption at 280 nm and 420 nm according to the Nanoprobes instructions.

RNA probes were bound to biotinylated, fluorescently labeled oligonucleotides and filtered according to the protocol described in Chapter 2.

mRNA encoding for GFP that had been 5' capped and polyadenylated was melted at 70 °C in 1X PBS for 10 min and then rapidly cooled in ice briefly before RNA probes were added. The mixture was allowed to incubate overnight at 37 °C to allow RNA probes to hybridize with mRNA.

The next morning, the probe/mRNA was filtered through a 200 kDa syringe filter to remove unbound probes, then concentrated in a 50 kDa membrane filter (EMD Millipore). Next, the required volume of mRNA (translating to 500 ng mRNA unless otherwise specified) was diluted in OptiMEM (Life Technologies). The cationic lipid (Lipofectamine 2000, Life Technologies) was added to another tube of OptiMEM, then the cationic lipid was combined with the probe/mRNA, mixed gently, and allowed to incubate for 5 min at room temp (according to the manufacturer's instructions) and the complete mixture was added to cells sitting in growth media.

U2OS cells were cultured in similar media as those cells found in Chapter 2. Cells were seeded on grids, fiducial gold was added, and grids were plunge frozen in a manner similar to that found in Chapter 4. Grids were imaged in a manner similar to that found in Chapter 4, with the exception that grids were first imaged in cryo-fluorescence on a Cryo CLEM demo system (Leica) and wide-field fluorescence and phase z-stacks were acquired in order to locate puncta of interest.

References

1.Cmarko, D. & Koberna, K. Electron microscopy in situ hybridization: tracking of DNA and RNA sequences at high resolution. *Methods Mol. Biol.* **369,** 213-28 (2007).

2.Bassell, G. J., Powers, C. M., Taneja, K. L. & Singer, R. H. Single mRNAs visualized by ultrastructural in situ hybridization are principally localized at actin filament intersections in fibroblasts. *J. Cell Biol.* **126,** 863-76 (1994).

3.Li, K. *et al.* Subcellular partitioning of MRP RNA assessed by ultrastructural and biochemical analysis. *J. Cell Biol.* **124,** 871-82 (1994).

4.Sahin, U., Karikó, K. & Türeci, Ö. mRNA-based therapeutics [mdash] developing a new class of drugs. *Nature Reviews Drug Discovery* (2014).

5.Wang, W., Li, W., Ma, N. & Steinhoff, G. Non-viral gene delivery methods. *Curr Pharm Biotechnol* **14,** 46-60 (2013).

6.Elouahabi, A. & Ruysschaert, J. Formation and intracellular trafficking of lipoplexes and polyplexes. *Mol. Ther.* **11,** 336-47 (2005).

7.Fasbender, A. J., Zabner, J., Moninger, T., Poellinger, K. A. & Welsh, M. J. Cellular and Molecular Barriers to Gene Transfer by a Cationic Lipid. *Journal of Biological Chemistry* **270,** 18997 (1995).

8.Ouahabi, El, A. *et al.* Intracellular visualization of BrdU-labeled plasmid DNA/cationic liposome complexes. *J. Histochem. Cytochem.* **47,** 1159-66 (1999).

9.Eastman, S. J., Siegel, C., Tousignant, J. & Smith, A. E. Biophysical characterization of cationic lipid: DNA complexes. *... et Biophysica Acta (BBA ...* (1997).

10.Xu, Y., Hui, S. W., Frederik, P. & Szoka, F. C. Physicochemical characterization and purification of cationic lipoplexes. *Biophysical journal* **77,** 341-53 (1999).

11.Sternberg, B., Sorgi, F. L. & Huang, L. New structures in complex formation between DNA and cationic liposomes visualized by freeze-fracture electron microscopy. *FEBS Letters* **356,** 361-6 (1994).

12.Lasic, D. D., Strey, H. & Stuart, M. The structure of DNA-liposome complexes. *Journal of the ...* (1997).

13.Huebner, S., Battersby, B. J., Grimm, R. & Cevc, G. Lipid-DNA complex formation: reorganization and rupture of lipid vesicles in the presence of DNA as observed by cryoelectron microscopy. *Biophysical journal* **76,** 3158-66 (1999).

14.Gustafsson, J., Arvidson, G., Karlsson, G. & Almgren, M. Complexes between cationic liposomes and DNA visualized by cryo-TEM. *Biochimica et Biophysica Acta (BBA) - Biomembranes* **1235,** 305 (1995).

15.Le Bihan, O. *et al.* Probing the in vitro mechanism of action of cationic lipid/DNA lipoplexes at a nanometric scale. *Nucleic Acids Res.* **39,** 1595-609 (2010).

CHAPTER 7

FUTURE DIRECTIONS

The work presented in this document could be taken in several directions in the future. These paths can be divided into several categories: probe design, RSV tagging, and other model systems.

Probe design

Several changes to the probe design could merit further investigation. First, the gold nanoclusters could be conjugated to the oligonucleotide arms, either through end labeleing or internal modification, as opposed to being reacted to the neutravidin core. This might allow for even more nanoclusters per probe, although it would have to be verified that this wound not adversely affect base pairing. Second, the probe chemistry could be altered to improve affinity for its target. Locked nucleic acids (LNA) and PNA have higher affinities for their complements and are more resistant to degradation by nucleases. The PNA would arguably be the most interesting because its backbone is uncharged, therefor any doubts about whether the cationic lipid is capable of displacing the probes from the mRNA should be dispelled. Third, several more probe sequences against a target mRNA could be looked at in order to get more structural information about the mRNA in lipoplexes. Perhaps if there were many probes biased towards one end of the mRNA additional information about the orientation and distribution of mRNAs in lipoplexes could be gained. This would be especially important for attempting to follow lipoplexes for longer periods of time, including their possible disruption of the endosome.

Finally, and this is less important for the case of mRNA in a lipoplex than it is for tagging an endogenous mRNA or viral RNA, the probes could be labeled with an epitope tag and the RNA of interest, along with its binding proteins, could be interrogated by proximity ligation assays or pulled down and assessed by Western blot, mass spectrometry, or other means to identify the particular molecules that interact with that RNA. Perhaps this could be combined with one of the higher affinity probe chemistries mentioned previously to increase the pull down efficiency.

RSV tagging

We have demonstrated that our probes bind to the RSV genome and incorporate in filamentous virions. Ultimately, the cryo-EM and cryo-ET of the virus at different timepoints in the infection will have to be attempted. The orientation and number of RNPs per virus would be an easy first target, again using multiple probe sequences, perhaps biased on one end of the genome. A first proof of principle experiment could be labeling extracted RNPs from purified virus or synthetic RNPs made from in vitro transcribed RNA encapsidated in recombinant N protein.

Early entry events would be achievable so long as the labeled virus can be concentration sufficiently. If the probe labeling could be shown to be an indicator of a complete virus, it would be helpful to elucidate any differences in entry between a complete virus and a DI particle. Moreover, depending on the quality of tomograms collected, perhaps educated guesses about the identity of the fusion receptor for RSV could be made. Indeed, this author has attempted a few RSV entry experiments involving blocking the candidate receptor nucleolin, but has been unsuccessful in replicating the results of other groups. Additionally, it could be shown whether the virus goes through a

macropinocytotic mechanism, involving cleavage of the fusion receptor and the function of the SH protein as an ion pore, or through some non-compartmentalized path.

Perhaps even slightly later events could be elucidated by tagging the genomic RNP, particularly with access to a CLEM system. For instance, after the granules enter and unpack, perhaps the unpackaging of the genomic RNA could be observed. The location of the L protein during those early events would be of particular interest, especially since: the L protein is rarely identified in images of assembled virus; is possibly electron dense enough to be identified; would verify results from minigenome in vitro experiments by other groups. However, finding the L, as well as conclusively identifying other viral proteins and their structures, such as the M2-1 monomer vs. tetramer debate, might still remain unsettled without either fitting the cryo-ET data to known crystal structures, or the implementation of an electron dense protein label such as metallothioenin. A (slightly cheating) alternative to protein labeling would be the light chemical fixation and permeabilization of the cell with saponin, followed by antibody staining. However, this approach is likely to mar the ultrastructure and ruin the membrane, but might be appropriate on a case-by-case basis.

As for later, assembly events, we have already demonstrated that we can image at least viruses extending off of cells. However, it is important to note that as an infected progresses further and further in its infection, its thickness increases, limiting the potential tomography to only the most distal filaments form the cell body. Perhaps the CLEM system would enable the researcher to identify the first few filaments that assemble before the cell becomes too thick. Otherwise, assuming that the high expression of N is responsible for the cell swelling, perhaps the expression of N could be modulated

somewhat through RNAi, but that could be a complicated balancing act. Without some sort of sectioning capability, it will be difficult to peer further into a cell late in the timecourse of an RSV infection.

Other model systems

Lastly, there are a number of other viral and endogenous model systems to which these RNA probes could apply. Since most of the paramyxovirus research is done by comparing paramyxoviruses to each other or to other virus families, any other virus for which appropriate target sequences could be identified could be labeled with RNA probes, assuming the appropriate controls are run. The findings from studying the structure and function of the genomic RNA of RSV could be applied to measles, Sendai, or another related virus.

Also, particularly with the CLEM system (and possibly with a super-resolution fluorescence CLEM system), endogenous RNAs could be probe labeled using SLO and their structure, localization, and interactions with other molecules could be described. Perhaps mRNAs could be seen attached to F-actin or trafficking on microtubules, translated in a polysome or being degraded in an exosome. Perhaps their protein regulators could be identified and imaged on their 3’ UTRs. But that is for tomorrow, and another dissertation.

VITA

ERIC J. ALONAS

Eric J. Alonas was born and raised in Scottsdale, Arizona. The son of an elementary school teacher and an electrical engineer, he received his K-12 education in the Scottsdale Unified School District, culminating his graduation from Arcadia High School in 2005. He obtained a B.S. in Biomedical Engineering with a minor in the Spanish language with Honors from Barrett, the Honors College at Arizona State University in 2009. He went on to pursue a doctorate in Biomedical Engineering. When he is not working on his research, he enjoys watching movies, exploring new restaurants and drinking establishments, and spending time with his cats, Sherlock and Watson.